The Effect of Cyclic Buckling on the Structure and Mechanical Properties of Ovine Tendon

By
Austin Joseph Yazbek MacDonald

A Thesis Submitted to
Saint Mary's University, Halifax, Nova Scotia
in Partial Fulfillment of the Requirements for
the Degree of Master of Science in Applied Science.

April 2024, Halifax, Nova Scotia

Approved:	Dr. Samuel P. Veres Supervisor
Approved:	Dr. Laurent Kreplak Examiner
Approved:	Dr. Danielle Tokarz Examiner
Approved:	Dr. Jan Rainey External Examiner

Date: April 10th, 2024

Abstract

The Effect of Cyclic Buckling on the Structure and Mechanical Properties of Ovine Tendon

By Austin Yazbek MacDonald

Tendons, functionally categorized as positional or energy-storing, have differing structures and mechanical properties but are both susceptible to damage. Tendinopathy is a chronic condition that exhibits repetitive mechanical overuse damage. Despite the significant societal impact of tendinopathy, its development is poorly understood, generating a plethora of suboptimal treatment methods. This thesis investigated cyclic buckling, present in tendon unloading, as the potential root cause for the initiation and subsequent damage propagation, preceding tendinopathy. Associated structural effects were investigated from the nano-to-micro scales, using fluorescence microscopy with a collagen hybridizing peptide, second harmonic generation microscopy, and polarized light microscopy. Mechanical properties were measured via tensile testing. The results showed cyclic buckling caused structural changes, from molecular denaturation to fibre kinkbanding, accompanied by reduced ultimate tensile strength. Importantly, changes were seen in both tendon types, suggesting that cyclic buckling could be a loading mode responsible for damaging human tendons that frequently suffer tendinopathy.

Date: April 10th, 2024

Acknowledgements

Firstly, I would like to thank my supervisor, Dr. Sam Veres. Sam, ever since the first day we met over Zoom where you agreed to accept my late application for this program, you have done nothing but encourage and guide me. When I started with you in September of 2021 the world of research was foreign to me, and I had no idea what to expect. I am very grateful for your patience with me through the countless mistakes I made and unrealistic deadlines I proposed. Your combination of assisting and teaching, when necessary, while not overstepping and still allowing me to learn from my own doing has taught me more than I ever expected. I can't thank you enough. I also want to say thank you to my supervisory committee, Dr. Danielle Tokarz and Dr. Laurent Kreplak. Through your questions and help in guiding me in the right direction, you have taught me to think much more critically about my work and that every component to a project should have a purpose.

Thank you to Northumberlambs for providing the samples required for my project. Thank you to Saint Mary's University and to Research Nova Scotia for the ongoing funding that made this project possible.

Amanada Lee, Ted Lownie, and Kelsey Gsell thank you for making the lab a more fun and entertaining place. It would not have been nearly as enjoyable coming in everyday without any of you. I'm glad I made a few new friends outta this whole thing too. Also, thank you for all your help with my work and teaching me all the little things when I had no idea what I was doing. MacAulay Harvey, thank you for the many hours you spent teaching me about light microscopy, editing my drafts, helping me interpret results, and discussing our work. All our conversations and chess games were a great break from work and much enjoyed. Richard Cisek, thanks for all your help fitting and discussing my SHG data. And thank you for teaching me the iterative process of research and that my project can adapt in whatever direction I think makes the most sense, you've really helped me understand how to better conduct research. Thank you to Gerard Gaspard, Darren Cole, and Meghan Martin for all your microscopy help.

To Grandad, Nana, Dianne, جدي وستي. I am so grateful for the love and support you have given me in everything I do, I love you all so so much and I am so happy you have all been such a big part of my life. Zane and Ella, even though you might not think it, I wouldn't trade you in for anything. All our stupid arguments have helped me improve my thinking and writing. Thanks for being the bestest siblings, even though you're so stinky! I love you guys. Lastly, Mom and Dad, I could write a whole thesis on how you have been the best parents ever but since I don't have enough room, I'll leave you with this: "Dear mommy and daddy, You are special because you Are the most special in my family you are the most Special Because you are my parents my parents are my most Special in my family. Because you are my parents. Love Austin".

Table of Contents

List of Equations

List of Figures

List of Tables

List of Abbreviations

ddH_2O	Double distilled water
AGE	Advanced Glycation End product
BA	Bending Axis
CDE	Common Digital Extensor
CHP	Collagen Hybridizing Peptide
CMDI	Cellular and Molecular Digital Imaging
CUE	Compression resulting from Unresolved Elongation
DIC	Differential Interference Contrast
E	Elastic modulus
GAG	Glycosaminoglycan
IFM	Interfascicular Matrix
KA	Kinking Axis
KFM	Kinkband Formation Model
LDE	Lateral Digital Extensor
MDE	Medial Digital Extensor
OCT	Optimal Cutting Temperature
PBS	Phosphate Buffered Saline
PIPO	Polarization-In Polarization-Out
PLM	Polarized Light Microscopy
PSA	Polarization State Analyzer
PSG	Polarization State Generator

SDF	Superficial Digital Flexor
SHG	Second Harmonic Generation
SMU	Saint Mary’s University
UTS	Ultimate Tensile Strength

Chapter 1: Introduction

1.1 Tendon Anatomy and Physiology

1.1.1 Structural Hierarchy

Tendons are an imperative component of the musculoskeletal system. This collagenous tissue is the connector between muscle and bone[1,2]. While tendons do not have the multiaxial strength of bone[3], or the force producing ability of muscle[4], they have their own duty, which is to facilitate locomotion, by transferring muscle generated forces to the attached bones[5,6]. To do so, tendons require high uniaxial strength[7,8], and a highly organized structural hierarchy[9–11]. This uniaxial strength is attained through the directionally dependent orientation of various levels of the tendon hierarchy[11].

While there is some debate amongst research groups, regarding the inclusion of certain levels and the associated nomenclature, there is a general agreement on the tendon structural hierarchy. This structure is comprised of seven levels, in ascending order: tropocollagen, microfibril, sub-fibril, fibril, fibre, fascicle and tendon (Figure 1.1)[11,12]. Further, this hierarchy can be reduced to three classifications of size. The nanoscale encompasses the tropocollagen molecule, all the way to the fibril. The microscale includes the fibre and fascicle. The entire tendon is on the macroscale.

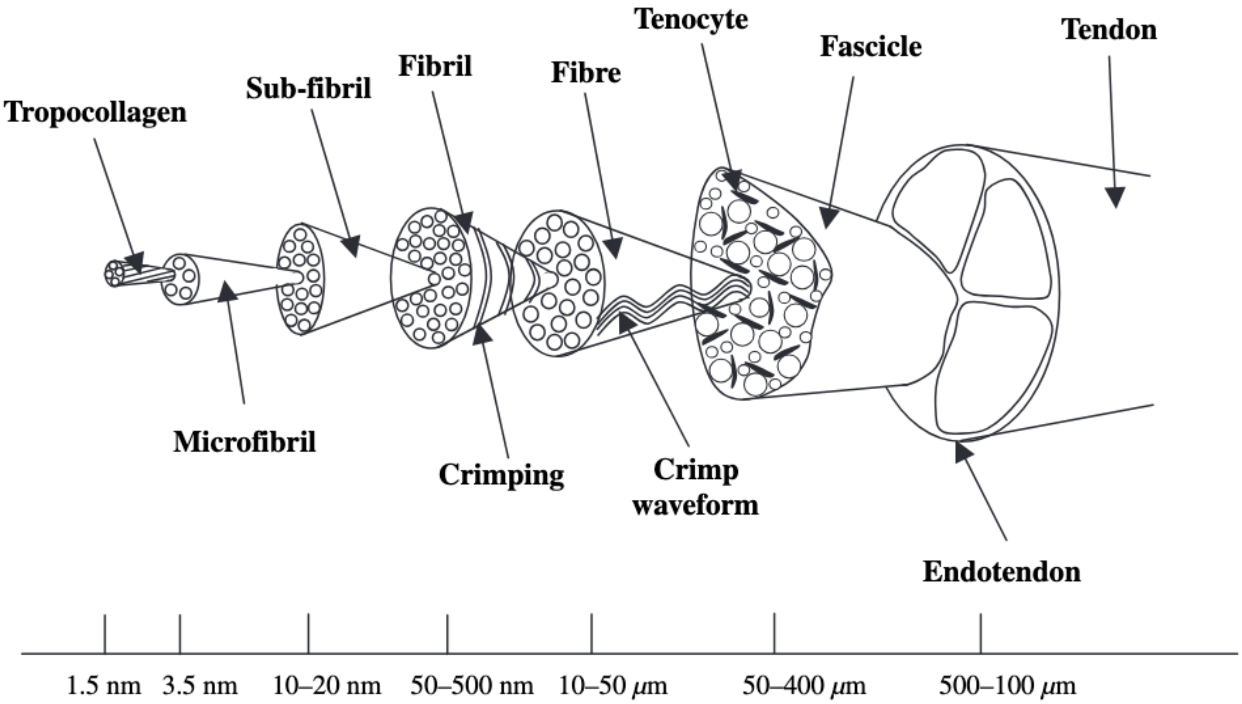

Figure 1.1: Schematic of the tendon structural hierarchy. (See Appendix II for permissions)[13]

As the roles and responsibilities of muscles and bones vary throughout the body, based on their location, the same is true for tendons. Consequently, function is used as a classification tool. There are two tendon types, energy-storing, and positional[5,14]. Energy-storing tendons have a special function of elongating and recoiling during locomotion, to store and release strain energy (like a spring), reducing the energetic cost associated with locomotion[15,16]. All other tendons are considered positional, frequently used to articulate body segments with high precision, under minimal stresses[5,17,18]. To maximize efficacy for their required roles, structural differences are present at various hierarchical levels, while still maintaining the same general structural hierarchy.

Nanoscale

To investigate the nanoscale of tendon, very high-resolution microscopies are utilized. Among others, some common choices are fluorescence microscopy, second harmonic generation microscopy, scanning electron microscopy, transmission electron microscopy, and atomic force microscopy[19,20].

Tropocollagen is the primary structural unit of the tendon hierarchy, having a diameter of 1.5 nm and a length of 280-300 nm in fibril forming collagens[10,11,21,22]. These molecules are comprised of three polypeptide strands of the pattern Gly-Xaa-Yaa, held together in a triple helical arrangement through the utilization of hydrogen bonding, where Xaa and Yaa can be any amino acids, though are typically proline and hydroxyproline[21,23–25].

As groups of five collagen molecules aggregate together in highly organized arrangements, they form microfibrils, the basic subunit of a fibril. Microfibrils have a diameter on the nanoscale, reported to be 3.5 nm[5,10,11]. Though often neglected, the sub-fibril is a group of compact microfibrils, having a diameter of approximately 20 nm[12].

Composed of highly organized members of the collagen family (mainly type I collagen), tendon fibrils maintain their structure through intermolecular crosslinking[21,25,26]. While the length of fibrils is still unclear[27,28], their bimodal distribution of diameters is known to range from 50-500 nm, differing between tendon types[10,11,29]. Across multiple animal models, electron microscopy has illustrated that positional tendons possess a larger mean fibril diameter than energy-storing tendons. The bovine, positional common digital extensor (CDE), and energy-storing superficial digital flexor (SDF) tendons have been shown to have mean fibril diameters of approximately 130-135 nm, and 75-80 nm, respectively[29,30]. These findings were supported by the larger fibril diameters observed in equine CDE compared to SDF tendons (229 nm vs. 169 nm)[31]. In a third large animal model, one group showed a contradictory result, where the ovine positional lateral digit extensor (LDE) tendon had a smaller mean fibril diameter than the SDF tendon (187 nm vs. 240 nm)[32]. Though it was shown in another ovine study that the CDE tendon, having a mean fibril diameter of 138 nm, was larger than that of the SDF tendon, whose mean fibril diameter was 117 nm, in agreement with the rest of the literature[29]. Not only does the mean fibril diameter differ between tendon types but the means of each peak differs, in the bimodal fibril distribution, present in both tendon types[29,30,32]. In one study, both bovine and ovine fibril diameter peaks were investigated[29]. Bovine small and large fibril diameter peaks were observed in positional tendons at 70 and 170 nm, and in energy-storing tendons at 55 and 126 nm[29]. The ovine small and large fibril diameters peaks showed a similar result, with peaks observed at 84 and 165 nm for positional tendons, and 66 and 145 nm for energy-storing tendons[29].

The fibril structure is characterized by a property known as the D-band. D-banding is the axial quarter staggering of neighbouring collagen molecules, where length, D, is defined as the sum of gap and overlap regions periodically repeating every 64 nm in wet tissue and 67 nm in dry tissue[21,33–35].

Microscale

While other imaging techniques may be utilized, polarized light microscopy is a common choice for investigating the microscale, due to its cost effectiveness and ease of use[19].

There are two types of fibres present in tendons. The dominant type of fibre is formed when a group of collagen fibrils coalesce, creating highly organized longitudinal bundles, of diameter 10-50 μm[11,36]. Aside from collagen fibres, another type of fibre comprised of elastic material has been reported. These elastic fibres were found to be widely dispersed within densely packed groups of other fibres, with a higher incidence of occurrence near tenocytes in the extracellular matrix[37].

Collagen fibres are characterized by a feature known as waveform crimp, referred to as crimp or wavelength, describing the fibre's wave like structure that repeats on the order of 100 μm[6,38]. This structure, although not present in individual fibrils, is apparent in the bundled fibrils creating a fibre and is therefore discussed in relation to fibrils, despite being a microscale feature. One descriptor of crimp is its angle, which has not been reported to differ between tendon types. The crimp angle is known to range from 12.6° - 17.3° in different human tendons and the outer fibril crimp angle of the equine CDE and SDF tendons has been reported as 15.1° and 15.8° - 20.1° depending on age, respectively[39–41]. Another descriptor of crimp is its wavelength, which does depend on tendon type. A large difference in crimp wavelength has been reported between the bovine CDE (124 μm) and SDF (57 μm) tendons[30].

The last hierarchical level prior to the tendon is the fascicle. At the fascicular level, several components contribute to the structure, having diameter of 50-500 μm[11,42,43]. Predominantly collagen fibres, combined with some elastic fibres, congregate together to form fascicles[37].

Macroscale

The final level of the structural hierarchy is the full tendon (Figure 1.2). Tendons have a diameter of 500-3000 μm, which varies amongst species and between tendon types[10,11,14]. A key feature of tendon function stems from the interfascicular matrix (IFM). This matrix, comprised of collagenous and non-collagenous components, holds fascicles together and forms the tendon proper[37,44–46]. Among other IFM differences between tendon types[45,46], in CDE tendons these fascicles are more tightly packed, whereas in SDF tendons they are more loosely dispersed[17]. To aid the higher volumes of loading energy-storing tendons experience in vivo, the IFM has been reported to have a much more rapid turnover[47].

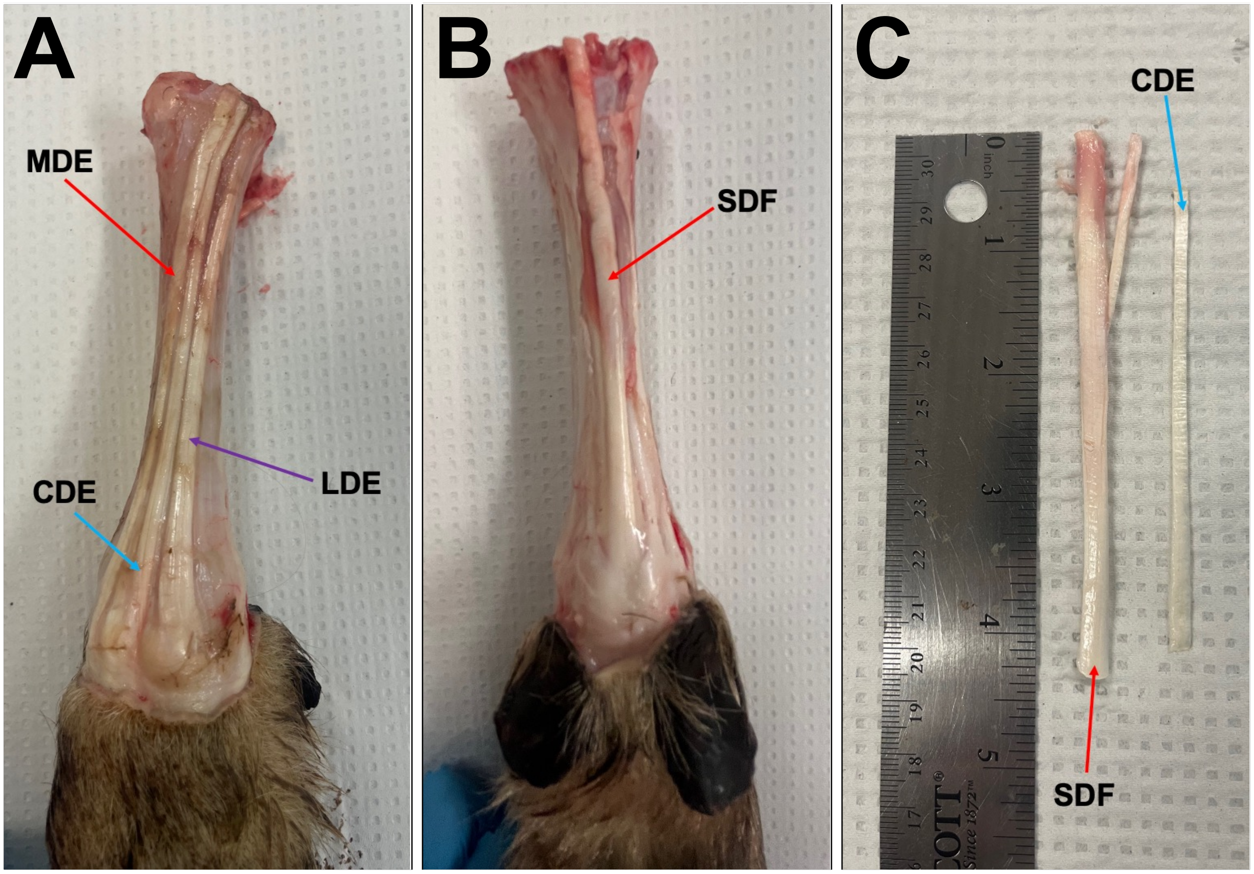

Figure 1.2: (A) Subdermal dorsal view of an ovine forelimb, with the in situ: medial digital extensor (MDE), common digital extensor (CDE), and lateral digital extensor (LDE) tendons labelled. (B) Subdermal palmar view of an ovine forelimb with the in situ superficial digital flexor (SDF) tendon labelled. (C) Image of the CDE and SDF tendons dissected from an ovine forelimb.

1.1.2 Tendon Mechanics

The observed structural differences between tendon types allows the differing mechanical properties to be tailored to the specific functional duties.

The nanostructure of collagen molecules adds difficulty when determining mechanical properties. Simulated and reported values of elastic modulus (E) and ultimate tensile strength (UTS) for individual collagen molecules, are in the range of 2.9-11.2 GPa and 0.5 GPa, respectively[22,48,49]. Progressing through the morphological hierarchy, tropocollagen relies heavily on intermolecular crosslinks to transmit forces and provide the desired mechanical properties to collagen fibrils. Intermolecular crosslinks increase the uniaxial strength of fibrils, while simultaneously reducing complicance[22]. The presence of crosslinking is therefore highly controlled to give tendon the necessary strength, without being excessively brittle, as is seen by the excessive crosslinks that accompanies aging[21].

While structural differences at the fibril level contribute to the unique mechanical properties of each tendon type, due to the difficulties posed by the small fibril size, a limited degree of evidence suggests the mechanical properties of individual fibrils differ. Differences have only been shown in one study, where a smaller elastic modulus was found in bovine positional, compared to energy-storing fibrils (333 ± 149 MPa vs. 774 ± 288 MPa)[18]. Though difficult to measure, fibril fracture strength and elastic modulus have been reported in other studies, regardless of tendon type, as 70-200 MPa and 0.3-1.5 GPa, respectively[50,51].

The properties observed in the tendon proper are heavily influenced by the microscale. The combination of fascicle and constituents contained within the IFM, provide tendon with its viscoelasticity. The differing mechanical properties at the full tendon level are largely attributed to the IFM, as there has generally been no report of tendon type affecting the fascicle elastic modulus (265-335 MPa) or failure stress (35-42 MPa)[17,52]. Unlike individual fascicles, there have been very significant differences reported in the interfascicular matrix modulus of elasticity (CDE tendon: 1586 MPa, SDF tendon: 1086 MPa) for equine positional and energy-storing tendons[14]. The more elastic IFM of energy storing tendons promotes a better resistance towards fatigue and possesses a superior resistance to plastic deformation[42,43].

The mechanical properties of the full tendon differ considerably between tendon types, as the composition of the IFM allows a greater degree of fascicle sliding in energy-storing tendons[43,52]. To withstand larger maximum in vivo loads, energy-storing tendons have a larger cross-sectional area than positional tendons, compensating for their lesser strength[14,53]. The larger ultimate tensile strength in positional versus energy-storing tendons has been shown across numerous animal models, including equine (positional: 145-157 MPa, energy-storing: 114-130 MPa)[17,52,54], bovine (positional: 37-46 MPa, energy-storing: 25 MPa)[55] and ovine (positional: 48 MPa, energy-storing: 31 MPa)[56]. Additionally, the larger elastic modulus has shown the same result across these animal models: equine (positional: 935-1035 MPa, energy-storing: 610-675 MPa)[17,52,54], bovine (positional: 185 MPa, energy-storing: 130 MPa)[55] and ovine (positional: 270 MPa, energy-storing: 120 MPa)[56]. To assess how closely the properties of these animal models resemble human tendons, the discussed properties are best compared to the Achilles tendon, a commonly considered human energy-storing tendon, analogous to the SDF tendon of large animals. In drawing comparisons, it is important to not only acknowledge the similarities between the human and animal tendons but also the differences based on animal, such as the very high levels of strain observed in the equine SDF tendon during its gallop[57]. The human Achilles tendon was observed to have an elastic modulus of 559-822 MPa and ultimate tensile strength of 71-86 MPa[58,59]. The observed human Achilles properties, similar to the commonly utilized animal models, help to validate the effectiveness of the chosen animal models as a relevant comparison. Another human energy-storing tendon commonly studied is the patellar tendon, though its function differs from the SDF tendons of large animals, as it experiences in vivo buckling and does not require the same spring-like abilities of the Achilles, it is still important to discuss due to its high rate of injury in humans. To suit these differing needs, the mechanical properties of the patellar tendon also differ, with an elastic modulus of 1.8 GPa and ultimate tensile strength of 48 MPa[60].

1.1.3 Loading Response

The unique makeup of tendon, containing components of varying properties, induces a viscoelastic loading response[61,62], which combines the elastic loading curve, where all deformation is recovered, and the viscous loading curve, where no deformation is recovered. This results in the mechanical response to an applied load being rate dependant[61]. Not only has this loading rate dependency been illustrated in the tendon proper, but it has been demonstrated at various hierarchical levels, such as the molecule[63], fibril[64], and fascicle[65,66]. An approximation of the resulting response to an applied tensile load is shown in Figure 1.3.

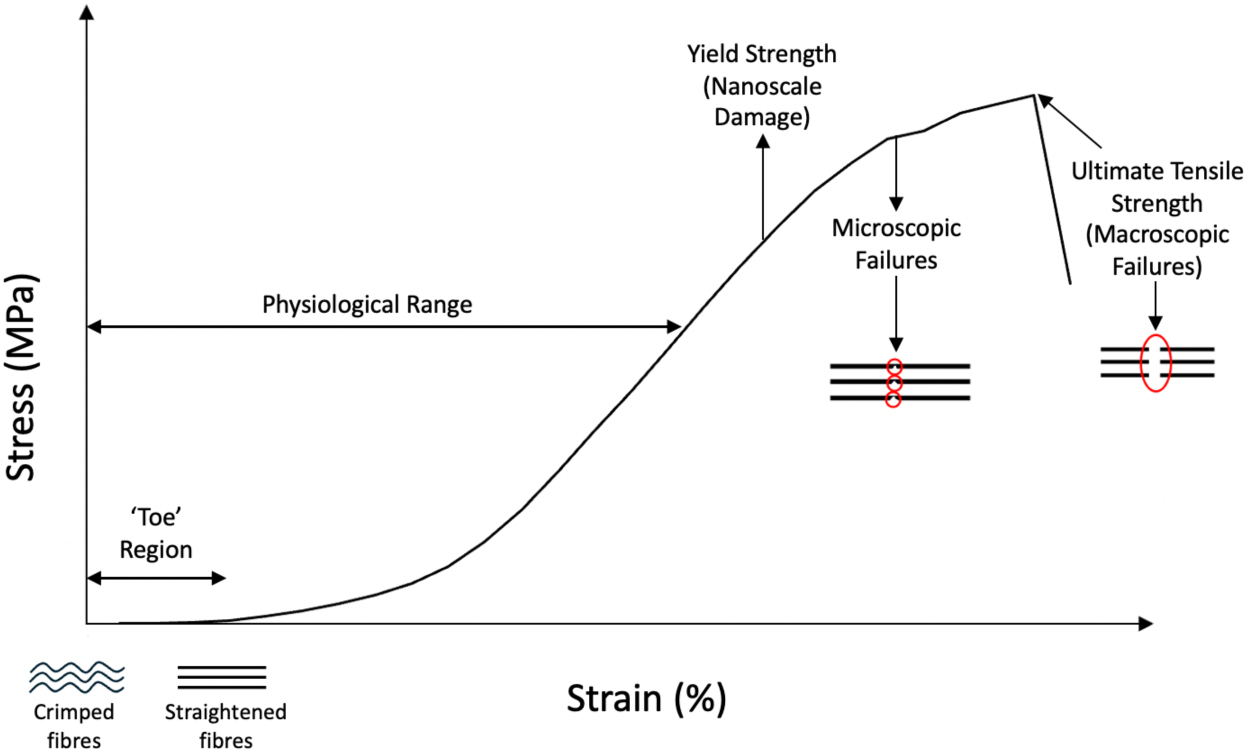

Figure 1.3: Stress-strain curve describing the mechanical response of tendon to an applied load. Upon the application of a load, the low force 'toe region' is where crimp is removed. From there, additional loading, exceeding the physiological range, increases likelihood of injury. This figure depicts the generalized response of a tendon to an applied load without including specific stress

and strain values, as different tendons of different species will experience structural effects at varying stresses and strains.

It is important to note that the numerical strain values associated with each stage of the tendon loading progression is a product of the individual tendon function and species. When a tendon experiences a tensile load, minimal applied stress is required for roughly the first 2-4 % of strain[13,67,68]. This low stress region of the loading curve is known as the toe region. Here, the fibres of the tendon undergo the process of straightening, removing all crimp before they withstand any significant load. Once fibres have straightened, any additional applied stress evokes a linear strain response for the next 2-6 % of strain, which is typical of physiological loading in some animals and still recoverable[13,67]. Though larger differences in the numerical values associated with each segment of the loading curve (shown in Figure 1.3) become apparent at this point, as the linear region exceeds a strain of 10% in other animal tendons, such as the equine SDF tendon, with physiological loading reaching up to 18% during galloping[57]. The ability to recover strain at this portion of the loading curve is largely attributed to the IFM and its combination of constituents that facilitate fascicle sliding[13]. At strains exceeding the maximum allowable linear region strains, failure of individual fibrils and fibres can begin in tendons, with further loading resulting in increased plastic damage[13,67]. This microscopic damage was suggested to occur at strains of 4-8 % by Wang et al.[67], but up to as high as 12-18% by Shojaee[57], with differing values related to the animals considered. Exceeding the strain where microscopic damage occurs, macroscopic tears initiate and propagate until the entire tendon ruptures[67]. The importance of the loading curve shown in Figure 1.3 is to understand the progression of tendon damage from the initiation of an applied load to the point of tendon rupture.

Of the many tendon constituents, the three main groups, which contribute to the structure and ultimately the mechanical response of tendons are crosslinks, collagenous, and non-collagenous components.

1.1.4 Crosslinking

Crosslinks, present within and possibly between fibrils[69,70], are a crucial regulator of tendon strength and stability, creating divergence between the mechanical properties of each tendon type. While the presence of crosslinking increases the strength of a structure, excessive crosslinking reduces extensibility, requiring the quantity and dispersion of crosslinking to be carefully selected for the specific tendon responsibilities during tendon development[69]. Crosslinking formation may occur either enzymatically or non-enzymatically at up to four locations per molecule[71].

Enzymatic crosslinks are formed via lysyl oxidase performing a deamination process on the amine side chains of specific lysine and hydroxylysine residues, converting them into aldehydes[71,72]. From here, enzymatic crosslinks are further divided into immature and mature crosslinks, based on their thermal lability[71,72]. Immature crosslinks are typically found as divalent aldimine or divalent keto-amine crosslinks[26,72]. Aldimine crosslinks maintain stability under physiological conditions but are easily cleaved by heat or acetic acid, while keto-amine crosslinks are not affected by heat or acetic acid[26,72]. Mature crosslinks are said to be thermally stable, and their trivalent nature results from the maturation of the prior divalent crosslinks[26,72].

Non-enzymatic crosslinks, known as advanced glycation end products (AGE)s are the undesirable crosslinks, formed after tendon development[72]. While the enzymatic crosslinks formed through development are meticulously located to provide the tendon the necessary mechanical properties, AGEs are unintentionally formed through a non-enzymatic reaction, where a sugar is covalently added to a protein, forming a crosslink[7,26,73]. These crosslinks are increasingly common in people with type II diabetes, as well as the aging population, as there is more opportunity for sugars to accrue[73]. The presence of AGEs is a form of damage, which increases the stiffness of tissue and results in reduced function, especially in energy-storing tendons[72,74].

1.1.5 Collagenous Components

The primary component in tendon is collagen, making up 65-80 % of its dry weight[46,75]. Of the 28 types of collagens present in the human body, several have some contribution to the tendon structure. The fibril forming types I and III are by far the most abundant, typically responsible for 95% and 3% of the total tendon collagen content, respectively[46,75]. The additional 2% is comprised of a combination of the following collagen types: V, VI, XII, XIV, XX[23,75]. While type I collagen is mostly responsible for creating the unidirectional fibrils of tendon, type III collagen is suspected in large part to facilitate and regulate the growth of type I collagen fibrils, as it has been shown to become more abundant with injury[76,77]. The content of each type of collagen varies between tendons regarding the health status, as different collagens provide different properties and functional roles. This is apparent by the increase of type III collagen, found in tendinopathic tendons[8]. Type III collagen is also found in larger quantities in the IFM, providing elasticity, fatigue resistance and an injury prevention mechanism[8,17].

1.1.6 Non-Collagenous Components

The remaining tendon composition is primarily occupied by a combination of proteoglycans and elastin[37,46]. Proteoglycans are a component of the tendon extracellular matrix that interacts with the tendon fibrils, facilitating fibril size, spacing and orientation[14,78]. Proteoglycans are made up of a core protein, from which, long glycosaminoglycan (GAG) chains are attached[46,79]. The negative charge and hydrophilic nature of GAGs is largely responsible for the extra cellular matrix's ability to retain water[80]. This directly relates to the viscoelastic behaviour of tendon, as it allows the tendon to elastically deform. When compressive forces are applied, the water helps cushion the forces, acting as a shock absorber[78,81]. As tensile forces stretch the tendon, the abundance of water acts as a buffer to help resist plastic damage[78,81]. If the water is not released from the extra cellular matrix at a sufficient rate, determined by the loading, damage may be applied directly to the fibrils. As proteoglycans contribute to the mechanical properties of tendon, they present differently based on circumstance. Due to the natural requirement of energy-storing tendons to undergo cyclic loading, they are an important component in resisting fatigue. As an increase in mechanical loading stimulates the production of proteoglycans, not only is tendon type a factor, but so too is injury. This has been observed through the larger GAG content and turnover in energy-storing tendons, relative to positional tendons, and the suspected increase of GAG content as an injury prevention mechanism[14,79].

Elastin is very fatigue resistant, and therefore more commonly found in tissue that undergoes high volumes of in vivo cyclic loading, such as the heart, skin, blood vessels, tendons, ligaments and more[44,82]. The presence of elastin in tendon helps contribute to its elastic behaviour. As energy-storing tendons experience higher volumes of in vivo cyclic loading, they consequently have a higher elastin composition than positional tendons[45]. This helps to facilitate high volumes of loading by allowing fascicular sliding, while still resisting injury[81].

1.2 Tendinopathy

Tendinopathy mainly incorporates two terms: tendinitis, and tendinosis[83]. Tendinitis describes a tendon injury characterized by an inflammatory response[77,84]. Tendinosis, a term coined by Puddu et al.[85], refers to the degeneration of tendon, in absence of any clinical or histological signs of inflammation. Tendinopathy describes the chronic pain and reduced function of tendon, resulting from excessive mechanical loading[83,86]. Tendinopathy is categorized as either symptomatic tendinopathy, referring to degenerative tendon changes accompanied by chronic pain, or asymptomatic tendinopathy, which refers to the rupture or partial rupture of tendon, linked to prior degenerative changes[87].

1.2.1 Aetiology and Epidemiology

Several risk factors are linked to tendinopathy, some more prevalent than others. To prevent tendon injury, the rate of damage must not exceed the rate of repair[88]. As this threshold is crossed, the tendon is incapable of meeting the healing demands and further loading becomes excessively more harmful, leading tendinopathies to often be referred to as overuse injuries[89,90]. Due to the high volumes of tendon loading experienced in athletes, they are at a greater risk of developing tendinopathy, specifically in high use tendons such as the rotator cuff, Achilles, patellar, tibialis posterior, and extensor carpi radialis brevis[77,86,87]. An important factor regarding overuse is tissue turnover. In the IFM, positional tendons experience a quicker turnover of collagenous components but a slower turnover of non-collagenous components, relative to energy-storing tendons[47]. The miniscule annual 0.25% of collagenous IFM turnover in energy-storing tendons helps explain why most tendons with the highest incidence of tendinopathy are energy-storing tendons, as once damage is accrued, they lack the required means for healing[47]. Other risk factors, preventing the ability for tendon healing at a high rate include sex (females are higher risk), aging, poor vascularization and consequently health conditions such as diabetes, high cholesterol, smoking and others[86,87,89–92]. While most research indicates tendon injury occurs because of overuse, the under stimulation of tendon has been shown to induce apoptosis, providing another injury factor[93,94].

1.2.2 Tendinopathy Models

To better understand the progression of tendinopathy, a combination of research based, and clinical models have been proposed. Research based tendinopathy models typically surface from animal testing. A model proposed by Shepherd et al.[88], using data from in vivo rat patellar tendons, broke the progression of disease into four stages. Starting with a healthy tendon, low levels of fatigue increase stiffness and decrease hysteresis, kinking fibres. At medium fatigue levels, there is a widening of the inter-fibre space in kinked fibres, maintaining the mechanics of the previous stage. At the last stage of high-level fatigue there are severe IFM disruptions, angulation, reduction in fibre cross-section and fibre discontinuities, accompanied by a reduction in stiffness, increases in energy dissipation and strain. A model proposed by Herod et al.[95], utilizing the bovine CDE tendon agreed, that the increasing loading cycles resulted in the kinking of fibrils, followed by fibres in a progression to tendon rupture. A distinguishing feature of this latter study was a conclusion that kinking resulted from buckling in the low force toe region.

In clinical tendinopathy models, the healing process of tendon is first considered. When tendons are loaded, they experience damage[86,87,93,96,97]. Some damage is required, to strengthen tendons, though excessive damage leads to injury[83,93,96]. To repair damage, the first step is for the tendon to display an inflammatory response, accompanied by various cellular and molecular changes[83,86,98]. The next stage is proliferation, which includes production of IFM components, an increase in type III collagen production and activation of stem cells[83,86]. Once a sufficient quantity of components to be used as the building blocks for recovery are produced, the focus is shifted to the remodelling of these added components[83,86]. This results in a reduction of IFM component production and the transition from type III to type I collagen, which can be organized as longitudinal fibrils, completing the ongoing healing process[83,86].

If loading induces damage exceeding the physiological healing abilities of tendon, this process differs and follows the proposed tendinopathy models, which agree. One model suggests that following injury, several intrinsic and extrinsic factors may cause failed healing, which then leads to a clinical presentation of tendinopathy[87]. Clinical presentations include rupture due to mechanical weakness, or pain due to increased nociception[87]. A second three stage model starts with stage 1 (reactive tendinopathy), which is a short-term fix, resulting from acute overload and causing damaged areas of the tendon to increase in thickness to reduce applied stress[96]. In stage 2 (tendon disrepair), an attempt is made to heal the tendon by increasing protein production and cell growth but is accompanied by tendon swelling and collagen disorganization[96]. Stage 3 (degenerative tendinopathy) is reached because of cell apoptosis, trauma or inadequate healing and leads to increasing collagen disorganization and tendon swelling, which is difficult to reverse[96]. A third model suggests that following repetitive mechanical loading, an inadequate cellular and IFM response leads to temporary tendon weakness[93]. If proper rest and precautions are not taken, the weakness becomes a long-lasting overuse tendon injury[93].

1.2.3 Clinical Treatment

Currently, many treatment options are available for tendinopathy, all of which have both benefits and weaknesses. The most obvious treatment is rest, as this gives the tendon adequate time to heal, though rest is not an ideal and often an unrealistic option[77]. Additionally, strengthening of tendons and supporting them with a brace is typical following treatment, though strengthening would be a much better preventative measure, as it is much harder to strengthen injured tendons than healthy ones[77]. Common non-pharmaceutical, non-invasive treatments include low-energy laser therapies such as ultrasound and shockwave therapy, often used along with cryotherapy[77,83]. These therapies are favourable due to their ease of use; however, their benefits are unclear[83]. It is suspected that some of the following apply to each therapy: promotion of blood flow, reduction of inflammation, promotion of proliferation[77,83]. Though the major drawback they pose is the inconsistent application between users and lack of a standard protocol, making results difficult to validate[83].

Other available options which have a greater validity are invasive treatments, though these are often high cost and higher risk, making them less desirable to some. Invasive options include gene therapy, growth factor therapy, steroids, other pharmaceutical agents and in severe cases, surgery[77,83,86].

The vast trade-off between cost and effectiveness/invasiveness leaves much to be desired in the realm of tendinopathy treatment. This makes the betterment of tendinopathy knowledge and understanding an imperative factor to assist clinicians.

1.3 In Vitro Mechanical Testing

Tendons experience various types of loading throughout their life. To better understand the structural and functional implications that different load conditions pose, in vitro mechanical testing is utilized. There are three main loading types utilized in tendon research: fatigue, creep/stress-relaxation, and tensile testing. Fatigue loading encompasses all forms of cyclic loading, including tension-tension, compression-compression, and tension-compression. Creep testing is the process of bringing a material to a set load and maintaining that load for a specific duration, monitoring properties such as strain, while stress-relaxation is the process of bringing a sample to a set strain and monitoring the reduction of stress over time. Tensile testing is the application of pulling a sample in tension, at a specific rate, until failure occurs.

1.3.1 Fatigue Testing

Fatigue testing is a valuable tool for determining a materials ability to resist damage over numerous loading cycles. Loading conditions are often altered to induce differing structural and mechanical responses.

In two studies by Makhzoomi et al.[33,99], utilizing the Achilles tendon of white rabbits, they investigated the effect of loading the tendons to strains of 3, 6 and 9 % over 9600 cycles (4 hours). They found that as the number of loading cycles increased, there was increasing fibril damage (kinking, fibril thinning, separation), dissociation and in severe cases rupture, which also increased with increasing strain[33,99]. This was all accompanied by decreasing fatigue resistance and stiffness, following the same severity as the structural damage[33,99].

Aside from the rabbit Achilles, which is a great analogous model to the human Achilles, due to the high forces it experiences, the CDE and SDF tendons of bovine and equine are commonly used, due to the large size of the animal model and similarities to human tendons. Three studies by Thorpe et al. have shown structural and functional differences between equine CDE and SDF tendon fascicles. The first looked solely at the SDF tendon, isolating fascicles, and cyclically loading them over 1800 cycles to 50% of predicted fatigue life[100]. It was observed that at sub-failure stresses the kinking of fibres still occurred. Additionally, localized fibre strains were greater than global strains[100]. A second study by this group tested both isolated fascicles and groups of 2 fascicles connected via the IFM of CDE and SDF tendons[43]. Samples were loaded from 0 to 3 % strain for 10 cycles before a pull to rupture, showing that the IFM of the energy storing SDF tendon was far more elastic and had better recovery than the positional CDE tendon[43]. The third study conducted by this group cyclically loaded isolated fascicles of SDF and CDE tendons to an appropriate peak load until rupture[42]. This experiment demonstrated that the CDE tendon had greater stiffness and the SDF tendon was more fatigue resistant (withstood 20 times more cycles)[42].

The most commonly utilized bovine tendons are the flexor and extensor tendons, but in some cases the positional tail tendon may be used. In a study by Veres et al., bovine tails were overloaded for either 5 or 15 cycles at a strain rate of 0.5%/s, showing a kinking of fibrils, along with a loss of D-banding that was more severe in the 15-cycle group which had a sharp crimp[101]. This kinking of fibrils and fibril misalignment was later observed by Shepherd et al. when comparing bovine CDE and energy storing deep digital flexor (DDF) tendon fascicles through 1800 loading cycles[102]. Both tendons displayed fibril kinking with the CDE tendon having a heightened UTS, and less fatigue resistance, shown by many other groups[102]. A study by Herod et al.[30] looked to further investigate this finding by testing pair matched CDE and SDF tendons of bovine forelimbs for 0, 500 or 1000 cycles of loading, to 30% failure strain at 10%/s. The stiffer CDE tendons were found to be less fatigue resistant than the SDF tendons, resulting in kinking of CDE tendon fibrils that propagated along a band, referred to as a kink band. Kink bands were present throughout the CDE tendons in both groups, with a higher rate of occurrence in the 1000-cycle group compared to the 500-cycle group[30]. The presence of kink bands was less common in the SDF tendon, with no evidence of kink banding in the 500-cycle group and rare observations in the 1000-cycle group[30]. This laboratory conducted an additional experiment, that took the SDF and CDE tendons of bovine forelimbs and subjected samples to 10 cycles of loading to 10% strain, before a pull to rupture at either 1 or 10 %/s[55]. The results here showed that at a strain rate of 1%/s, following rupture, the CDE and SDF tendons both contained repeated fibril kinking, while only the CDE fibrils showed the additional loss of D-banding. At the 10%/s strain rate, the CDE tendon contained the same kinking post rupture, though at this rate the fibril D-banding was not lost, while the SDF tendon showed no evidence of fibril plastic damage, prompting the conclusion that at higher rates, SDF fibrils undergo brittle-type fracture on overload[55].

1.3.2 Creep/Stress-Relaxation

These two loading types are often grouped together due to their similarities. The use of creep testing is commonly utilized in civil engineering, to better understand stationary structures, such as bridges. Albeit scenarios arise when tendons are subjected to prolonged static loading. Production line workers are one demographic who experience this loading in the tendons of their back and legs, as they maintain a slightly hunched over standing position for extended durations. Nonetheless, stress-relaxation loading is more commonly observed in tendons and additionally provides details regarding the tendon's inherent viscoelastic properties.

Pearson et al.[103] conducted a study on the human patellar tendon, in vivo. Patients were instructed to develop a maximum volumetric contraction lasting either 3-4 or 10-12 seconds, repeating 3 times with 180 seconds of rest between each. The results of this study showed a time dependant relationship between the duration of applied force and strain achieved. This demonstrated the viscoelastic properties of tendon, as the tendon stiffness was greater in the short contraction group.

A study by Duenwald et al.[61] looked at the stress-relaxation of porcine tendons, preloading them to strain of 2% to remove crimp, allowing them to rest and then loading to 6% strain to relax for 100 seconds, before reducing the strain to either 1, 2 or 3 % to recover for 100 seconds. They found that although the strain of 6% was not expected to be excessive, the rate of recovery was slower than the rate of relaxation. Further, the rate of relaxation was faster with increasing strain.

Another study looking at the viscoelastic behaviour of human tendon, using the subscapularis, was performed by Machiraju et al.[62]. In this study, the cadaveric subscapularis tendons were loaded to 80% of the rupture strain and left to relax. This testing again showed a non-linear viscoelastic behaviour and used finite element analysis to model the biomechanical behaviour.

1.3.3 Tensile Testing

Tensile testing provides material properties found by looking at a stress-strain curve, such as ultimate strength, yield strength, elastic modulus, and others, as previously discussed in Chapter 1.1.2. This mode of testing is often applied subsequent to another mechanical test, to monitor changes in mechanical properties.

Chapter 2: Research Objectives

2.1 Outcomes of Previous Literature

Through in vitro experimentation, cyclic loading of tendons has been shown to cause structural damage on a nano[18,30,33,95,99] and molecular[30,104–106] scale. In many cases, the result of these studies ends with a tensile failure[18,30,33,95,99,104–106]. This has led researchers to focus their research on tensile cyclic loading of tendons, manipulating variables such as the amount of stress/strain applied per cycle, the loading rate, and more. However, little attention has been directed towards the significance of the low-stress toe-region of the loading curve.

Recently, Herod et al.[95] performed cyclic testing on the bovine CDE tendon with two testing scenarios. In one scenario, each loading cycle took the tendon from zero strain to peak strain, then back to zero strain, repeating this cycle numerous times. In a second scenario, tendons were kept in constant tension throughout testing, effectively eliminating the toe-region of the loading cycle[95]. The results led to the proposition of a model termed the 'CUE' model[95]. This model suggests that during cyclic loading of tendon, the strain experienced is not immediately recovered[95]. Upon unloading and return to zero strain, the now longer tissue experiences compression induced bowing[95]. As the number of cycles increase, this progresses into buckling of fibrils, which propagate along a band of kinks, referred to as a kinkband, until eventually reaching the scale of fibre buckling and kinking[95]. Although kinkbanding is a well-known concept in material science, referring to the buckling of fibrous materials when subjected to excessive compressive stresses[107,108], it was not referenced in tendon literature prior to the 'CUE' model. The 'CUE' model concludes by suggesting that the failure to cease cyclic loading, following the formation of kinkbands, will inevitably lead to ruptures of individual fibrils, escalating into fibrous ruptures if loading persists[95]. Herod et al. proposes the 'CUE' model as a framework to describe the formation of tendinopathy, asserting that continued cyclic loading without intervention will inevitably lead to tendinopathy[95].

The concept of excessive tendon buckling as a precursor for tendinopathy is particularly relevant to the patellar tendon, which naturally undergoes buckling with movement[109–112]. However, as the 'CUE' model proposed by Herod et al.[95] only considered the bovine CDE tendon, its applicability across various tendon types remains unexplored.

2.2 Objectives

The study by Herod et al.[95] raises pivotal questions regarding the formation of tendinopathy. Is the toe region of the loading curve, where tendons experience buckling, responsible for the formation of kinkbands, and consequently tendinopathy? Does the superior fatigue resistance of energy-storing tendons reduce their susceptibility to cyclic buckling-evoked damage? These questions prompt the first two objectives, which delve into the structural response of tendons to cyclic buckling, taking into consideration the tendon type.

Objective (i): To investigate the effect of cyclic buckling on the molecular and nanoscale structure of ovine tendons.

Objective (ii): To assess the relative structural impact of cyclic buckling between the positional CDE and energy-storing SDF tendon.

Regardless of the structural changes accompanying cyclic buckling, how do tendons functionally respond? Are there changes to their mechanical properties? Which properties are most susceptible to change? How does tendon type affect the response of mechanical properties? These questions pave the way for the third and fourth objectives of this thesis, focusing on the response of mechanical properties, considering tendon type.

Objective (iii): To investigate the effect of cyclic buckling on the mechanical properties of ovine tendon.

Objective (iv): To assess the relative mechanical response to cyclic buckling between the positional CDE and energy-storing SDF tendon.

Chapter 3: Cyclic Buckling

3.1 Apparatus Construction – Hardware

To perform cyclic testing, a buckling apparatus was designed. The cyclic buckling apparatus (Figure 3.1) was constructed on top of an aluminum breadboard (MB3045/M, Thorlabs New Jersey), incorporating components sourced from various suppliers and custom-designed 3-D printed parts. All 3-D prints were crafted with a Dremel 3D45 printer, utilizing ECO-ABS filament (Dremel Canada). As shown on the left side of Figure 3.1, the actuator was elevated by a 3-D printed actuator mount securely fastened to the breadboard. On top of the actuator mount, an electromechanical actuator (A1 Series standard Servo Cylinder model, Ultra Motion New York) was bolted, powered by a 36-volt DC power supply (180W PSU, Ultra Motion New York). Actuator position readings were obtained through an RS 232 serial connection to a desktop computer and movements were orchestrated using a National Instruments data acquisition (DAQ) board (NI USB-6351, X Series DAQ, National Instruments Canada), facilitating control of the actuator using LabVIEW code.

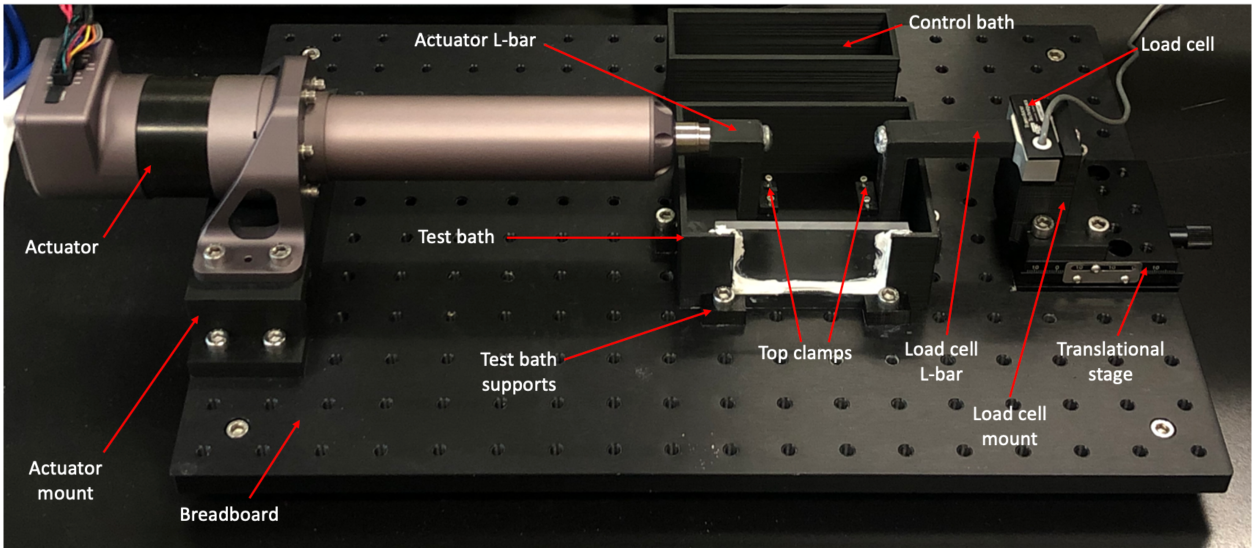

Figure 3.1: The cyclic buckling apparatus, illustrating all components with labels from left to right: actuator, actuator mount, breadboard, actuator L-bar, top clamps, test bath, test bath supports, control bath, load cell L-bar, load cell, load cell mount, and translational stage.

To the right of the actuator in Figure 3.1, a 3-D printed actuator L-bar (Figure 3.2 B) was screwed to the face of the actuator's stroke rod. The actuator L-bar was designed to have pyramidal teeth, offset from those of the top clamp (Figure 3.2 A) to create a snug fit through a peak to valley mate. The end of a test tendon was secured between the pyramidal teeth, applying compressive forces through a nut and bolt configuration (Figure 3.2 C and D). To maintain hydration of tendons throughout testing, a 3-D printed test bath, filled with a solution, enclosed the testing area, depicted in Figure 3.1. Six 3-D printed bath supports were employed to secure the test bath in place. Adjacent to the cyclic buckling apparatus, a separate 3-D printed bath filled with solution held the control sample.

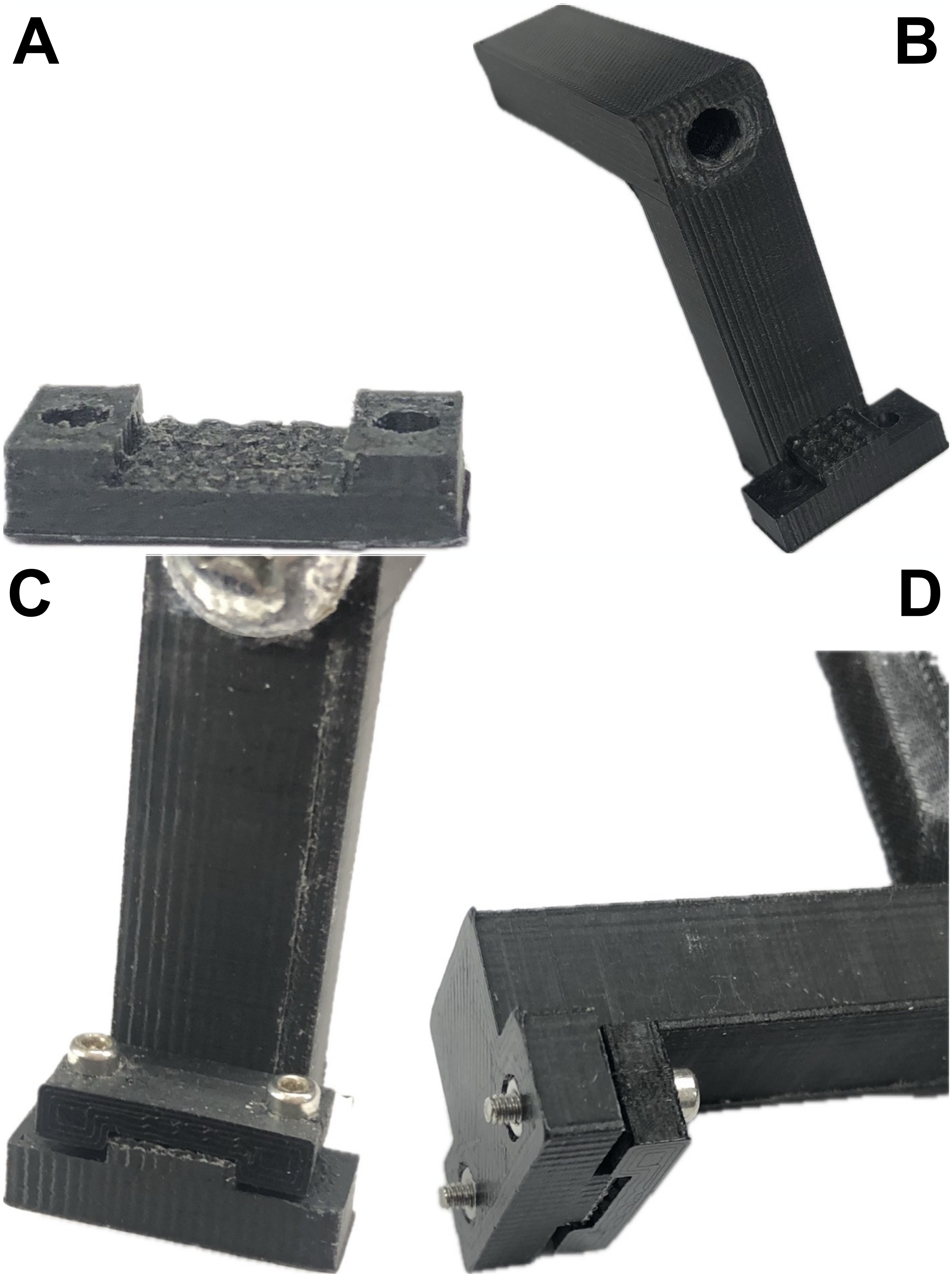
A
B
C
D

Figure 3.2: A magnified view of the two 3-D printed parts used for clamping tendon ends during cyclic buckling, (A) Top clamp and (B) L-bar. (C) and (D) A nut and bolt configuration compresses the parts, demonstrating the meshing of the teeth.

As seen in Figure 3.1, a 3-D printed load cell L-bar was located opposite of the actuator L-bar, to clamp the other end of the tendon. The load cell L-bar mirrored the pyramidal clamp design of the actuator L-bar. A load cell (MLP-100 Load Cell, Transducer Techniques California), connected to the right of the L-bar, measured the forces experienced by the test tendon throughout testing. A connector (9 PIN "D" series, Transducer Techniques California) was attached to the end of the load cell, equipped with a transducer electronic data sheet EEPROM. The connector had 'Smart Plug & Play IEEE 1451.4' capabilities and was connected to a high voltage transmitter (SST-HV, Transducer Techniques California), also equipped with 'Smart Plug & Play IEEE 1451.4' compatibility. The transmitter used an RS 232 serial connection to relay data to a desktop computer.

A 3-D printed load cell mount, as seen in Figure 3.1, was implemented to ensure the load cell was adequately secured at the proper height. Below the load cell mount but above the breadboard, in Figure 3.1, a Thorlabs translational stage (DTS25/M, Thorlabs New Jersey) was bolted and used to position the tendon prior to cyclic testing.

3.2 Apparatus Construction – Software

Software of the cyclic buckling apparatus was programmed using LabVIEW 2014 (National Instruments Canada). The front panel (Figure 3.3) served as a user-friendly interface, where the values for cyclic testing parameters could be input. The block diagram (Figure 3.4) delineated the sequential instructions for each step that the LabVIEW code was to perform once the program was executed.

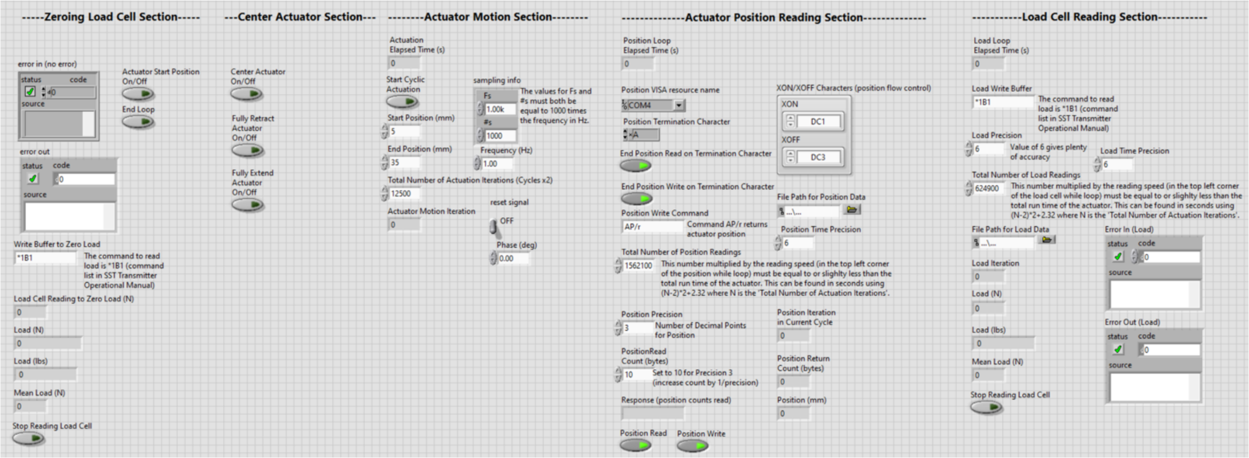

error in (no error): status ✓ code 0 source
error out: status ✓ code 0 source
Write Buffer to Zero Load: *1B1
The command to read load is *1B1 (command list in SST Transmitter Operational Manual)
Load Cell Reading to Zero Load (N): 0
Load (N): 0
Load (lbs): 0
Mean Load (N): 0

Actuation Elapsed Time (s): 0
Start Position (mm): 5
End Position (mm): 35
Total Number of Actuation Iterations (Cycles x2): 12500
Actuator Motion Iteration: 0
sampling info: Fs 1.00k; #s 1000
The values for Fs and #s must both be equal to 1000 times the frequency in Hz.
Frequency (Hz): 1.00
reset signal: OFF
Phase (deg): 0.00

Position Loop Elapsed Time (s): 0
Position VISA resource name: COM4
Position Termination Character: \A
XON/XOFF Characters (position flow control): XON DC1; XOFF DC3
File Path for Position Data: ...\...
Position Write Command: AP/r
Command AP/r returns actuator position
Position Time Precision: 6
Total Number of Position Readings: 1562100
This number multiplied by the reading speed (in the top left corner of the position while loop) must be equal to or slighlty less than the total run time of the actuator. This can be found in seconds using (N-2)*2+2.32 where N is the 'Total Number of Actuation Iterations'.
Position Precision: 3
Number of Decimal Points for Position
PositionRead Count (bytes): 10
Set to 10 for Precision 3 (increase count by 1/precision)
Position Iteration in Current Cycle: 0
Position Return Count (bytes): 0
Response (position counts read):
Position (mm): 0

Load Loop Elapsed Time (s): 0
Load Write Buffer: *1B1
The command to read load is *1B1 (command list in SST Transmitter Operational Manual)
Load Precision: 6
Value of 6 gives plenty of accuracy
Load Time Precision: 6
Total Number of Load Readings: 624900
This number multiplied by the reading speed (in the top left corner of the load cell while loop) must be equal to or slighlty less than the total run time of the actuator. This can be found in seconds using (N-2)*2+2.32 where N is the 'Total Number of Actuation Iterations'.
File Path for Load Data: ...\...
Load Iteration: 0
Load (N): 0
Load (lbs): 0
Mean Load (N): 0
Error In (Load): status ✓ code 0 source
Error Out (Load): status ✓ code 0 source

Figure 3.3: Front panel of the LabVIEW code employed for the cyclic buckling apparatus.

When the LabVIEW program was run, the first section of code executed was sequence 1 of the block diagram (Figure 3.4 A). This functioned as a calculator, converting counts and voltages into physical actuator positions, with inputs on the front panel representing the start (5 mm extension) and end (35 mm extension) positions of each cycle.

Sequence 2 of the block diagram (Figure 3.4 B) comprises two components. The top while loop in sequence 2 contained an embedded case structure, creating a switch available on the front panel that, when turned on, moved the actuator into the start position (where the tendons ends were furthest apart). The bottom while loop in sequence 2 used a serial connection to read, convert from pounds to newtons, and relay the force experienced by the load cell to the front panel, every 40 ms. To reduce error in force readings, the average of the 10 most recent readings were retained and the 11th reading was excluded. Using the force reading of the load cell, with the actuator in the start position, the translational stage was moved away from the actuator until a nominal tensile force of 0.1 N in the tendon was read. Subsequently, the switches for both while loops in sequence 2 were turned off, allowing the code to transition to sequence 3.

Sequence 3 (Figure 3.4 B) was implemented for the purpose of taking photographs of test tendons at the most buckled, least buckled, and midpoint of the buckling cycle. Each of the three case structures in sequence 3 corresponded to one of the on/off switches under the ‘Center Actuator Section’ on the front panel. Sequentially, each of the 3 on/off switches were turned on, photographs of the tendon were taken, and they were turned off, as multiple switches could not be kept on simultaneously. Once all photographs were taken, the switches were all turned off except for the midpoint switch, since the first buckling cycle commenced from the midpoint. Lastly, the ‘Start Cyclic Actuation’ switch on the front panel was turned on, exiting the while loop in sequence 3 and moving to sequence 4.

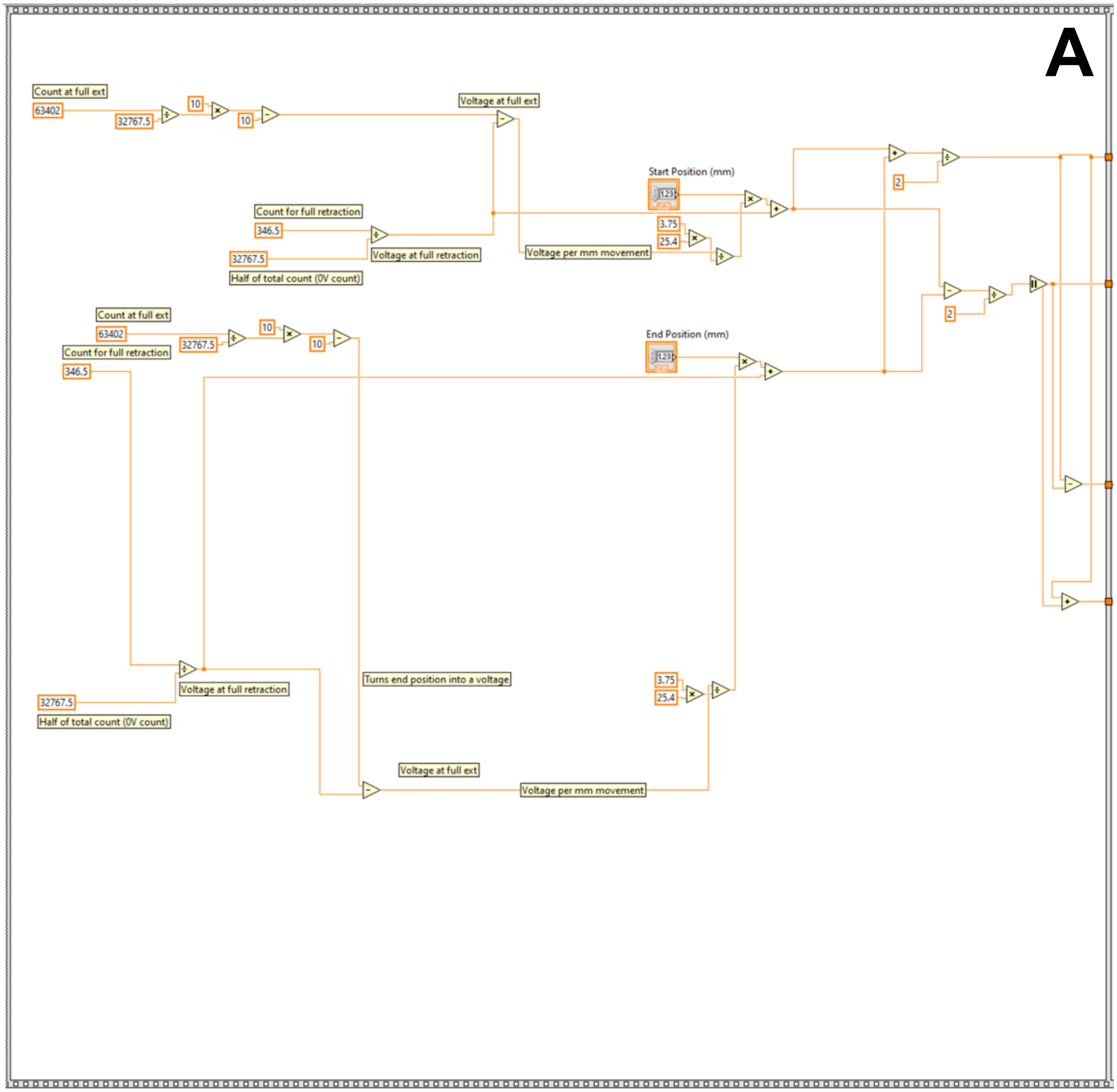

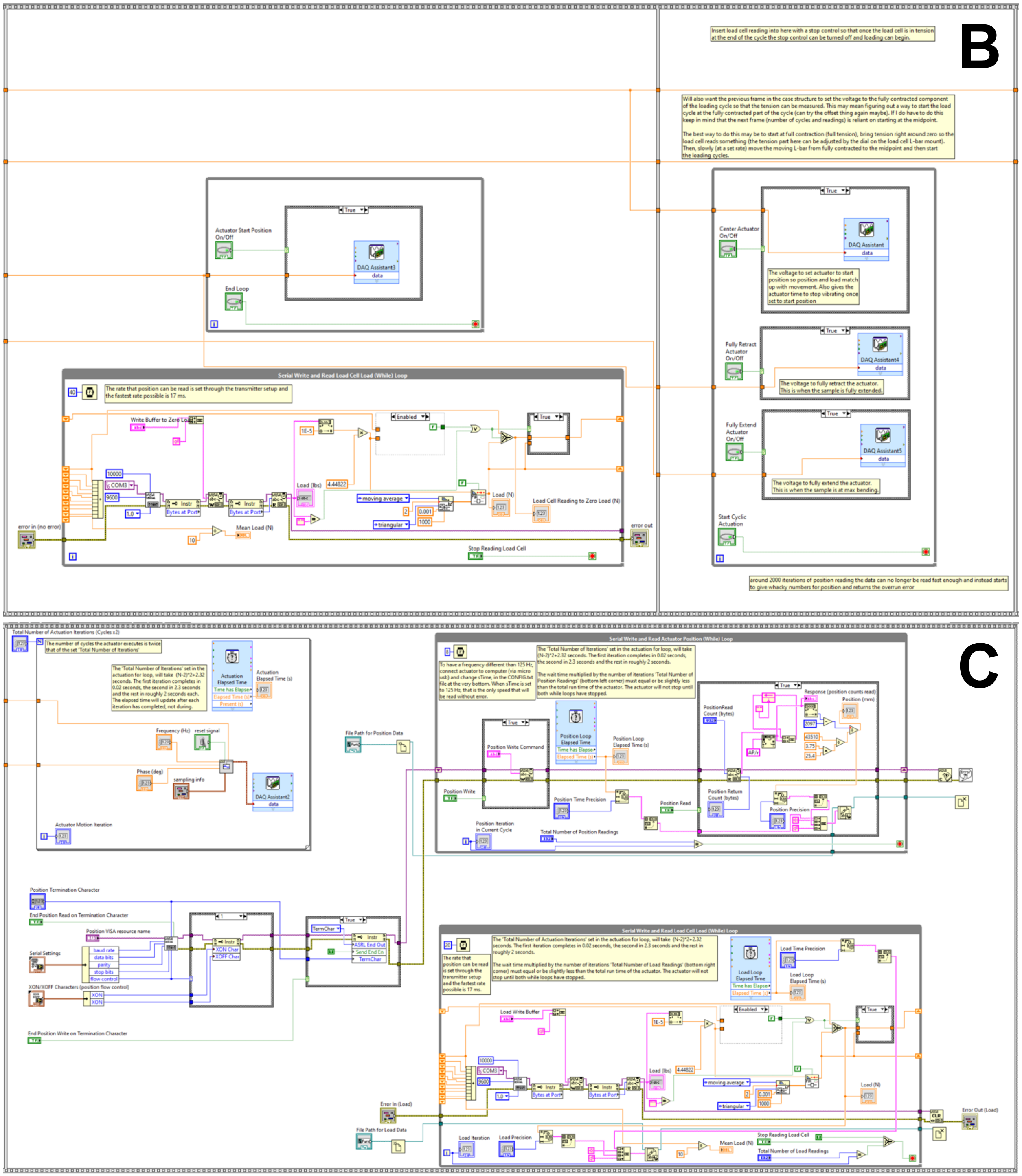

The rate that position can be read is set through the transmitter setup and the fastest rate possible is 17 ms.

Insert load cell reading into here with a stop control so that once the load cell is in tension at the end of the cycle the stop control can be turned off and loading can begin.

Will also want the previous frame in the case structure to set the voltage to the fully contracted component of the loading cycle so that the tension can be measured. This may mean figuring out a way to start the load cycle at the fully contracted part of the cycle (can try the offset thing again maybe). If I do have to do this keep in mind that the next frame (number of cycles and readings) is reliant on starting at the midpoint.

The best way to do this may be to start at full contraction (full tension), bring tension right around zero so the load cell reads something (the tension part here can be adjusted by the dial on the load cell L-bar mount). Then, slowly (at a set rate) move the moving L-bar from fully contracted to the midpoint and then start the loading cycles.

The voltage to set actuator to start position so position and load match up with movement. Also gives the actuator time to stop vibrating once set to start position

The voltage to fully retract the actuator. This is when the sample is fully extended.

The voltage to fully extend the actuator. This is when the sample is at max bending.

around 2000 iterations of position reading the data can no longer be read fast enough and instead starts to give whacky numbers for position and returns the overrun error

The number of cycles the actuator executes is twice that of the set 'Total Number of Iterations'

The 'Total Number of Iterations' set in the actuation for loop, will take (N-2)*2+2.32 seconds. The first iteration completes in 0.02 seconds, the second in 2.3 seconds and the rest in roughly 2 seconds each. The elapsed time will update after each iteration has completed, not during.

To have a frequency different than 125 Hz, connect actuator to computer (via micro usb) and change sTime, in the CONFIG.txt file at the very bottom. When sTime is set to 125 Hz, that is the only speed that will be read without error.

The 'Total Number of Iterations' set in the actuation for loop, will take (N-2)*2+2.32 seconds. The first iteration completes in 0.02 seconds, the second in 2.3 seconds and the rest in roughly 2 seconds.

The wait time multiplied by the number of iterations 'Total Number of Position Readings' (bottom left corner) must equal or be slightly less than the total run time of the actuator. The actuator will not stop until both while loops have stopped.

The rate that position can be read is set through the transmitter setup and the fastest rate possible is 17 ms.

The 'Total Number of Actuation Iterations' set in the actuation for loop, will take (N-2)*2+2.32 seconds. The first iteration completes in 0.02 seconds, the second in 2.3 seconds and the rest in roughly 2 seconds.

The wait time multiplied by the number of iterations 'Total Number of Load Readings' (bottom right corner) must equal or be slightly less than the total run time of the actuator. The actuator will not stop until both while loops have stopped.

Figure 3.4: Block diagram of the LabVIEW code used for the cyclic buckling apparatus. The block diagram uses a sequence structure, where the code is contained within 4 sequences: (A) sequence 1, (B) sequences 2 and 3, and (C) sequence 4.

All front panel controls created within sequence 4 (Figure 3.4 C) were adjusted prior to running the LabVIEW code. These controls encompassed all specifications related to the cyclic motion of the actuator, along with all entities read from the load cell and actuator. Sequence 4 contained 3 loops. In the top left corner of sequence 4 was a for loop responsible for the actuator cyclic motion. The start and end position inputs from sequence 1 determined the stroke of each cycle and the frequency, phase, and sampling info inputs from sequence 4 determined the start location, duration, and number of position signals for each cycle. The for loop continued to run until the ‘Actuator Motion Iteration’ indicator on the front panel, which represented total elapsed cycles, reached the total number of experimental cycles, set in the ‘Total Number of Actuator Iterations (Cycles x2)’ control on the front panel.

The while loop in the top right corner of sequence 4 used a serial communication to read position data from the actuator every 8 ms, throughout the duration of actuator movement. The total number of cycles set for the position readings was set to last slightly longer than actuator motion, to ensure the actuator ended at the proper time. When the ‘Position Iteration in Current Cycle’ indicator equalled the ‘Total Number of Position Readings’ control, the LabVIEW program stopped reading the actuator position and wrote all position readings to a text file, with a neighbouring column for elapsed time at each reading. Additional controls within the loop, for precision of actuator position and time elapsed, were also integrated into the front panel.

The while loop in the bottom right corner of sequence 4 also used a serial communication, receiving force readings from the load cell every 20 ms. To enhance accuracy, the mean of the most recent 10 readings was recorded, rather than individual readings. The total number of load cell readings (cycles) was set to last slightly longer than the duration of actuator motion, to ensure that if the test tendon slipped from the grips, it would be detected. When the ‘Load Iteration’ indicator value equalled the ‘Total Number of Load Readings’ control, the while loop ended and the force readings, along with a neighbouring column for time elapsed, were sent to a text file. Additional controls within the loop, for precision of force and time elapsed, were added to the front panel.

3.3 Sample Overview

The following research was conducted utilizing the common digital extensor and superficial digital flexor tendons of mature ewe forelimbs. Forelimbs were sourced from Northumberland Lamb Marketing Co-Op Ltd., a provincially inspected abattoir in Truro, Nova Scotia. The slaughtering of ewes took place from 7:00 am – 11:00 am. Forelimbs were bagged in matched pairs, with accompanying information regarding their approximate age. Bags were placed in a cooler with ice and transported to Saint Mary’s University (SMU) for dissection, within 90 minutes of the last animal being slaughtered. At SMU, the CDE and SDF tendons from each forelimb were dissected using a surgical blade (sterile, no. 11, stainless steel, surgical blade; Swann-Morton Canada). Each tendon was wrapped in phosphate buffered saline (PBS)-soaked gauze, sealed inside two labelled Ziplock bags and promptly stored in a -86 °C freezer.

3.4 Cyclic Buckling Procedure

On testing days, a tendon and its matched pair from the contralateral forelimb were retrieved from the freezer, removed from their bags, and left to thaw for one hour at room temperature. A razor blade (single-edged carbon steel, VWR Canada) was used to remove a 50 mm long segment from the center of each tendon, placing one in the test group and the other in the control group.

Tendons were clamped on one end using a paper clip and suspended in a custom-built apparatus (Figure 3.5). Each tendon was photographed four times, rotating 90° degrees after each photograph, resulting in two images of the major diameter and two images of the minor diameter for cross-sectional area calculations.

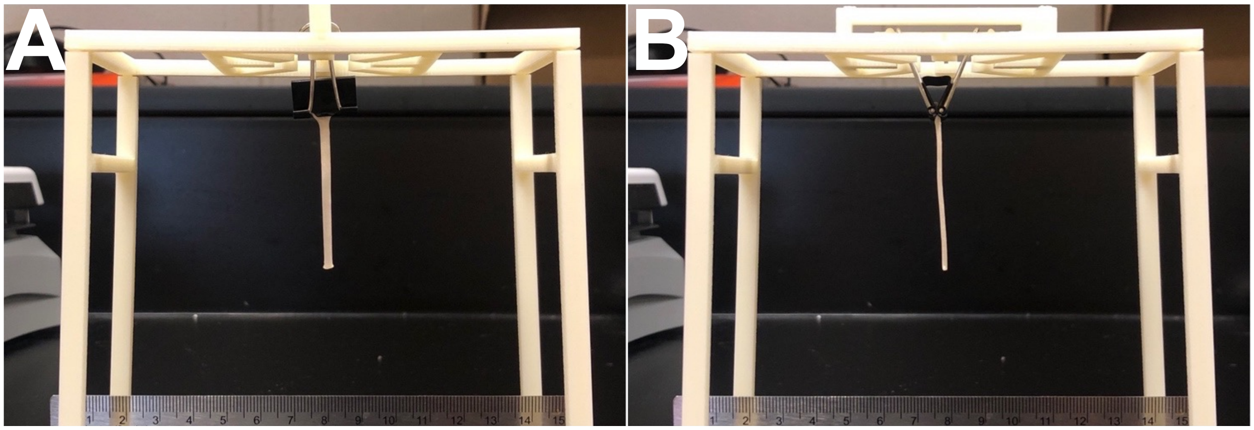

Figure 3.5: A longitudinally suspended CDE tendon, (A) with the major diameter and (B) with the minor diameter in the plane of view. These images were used to calculate tendon cross-sectional area. Images were opened in ImageJ, and the diameter was measured 25%, 50% and 75% of the distance from the tendon's end.

Test tendons underwent cyclic buckling using the custom-built buckling apparatus, seen in Figure 3.1. One end of the tendon was clamped to the moving L-bar and the other end was clamped to the load cell L-bar, ensuring the tendon was not yet in tension. After tightening the clamps, a 250 mL room temperature solution of 99% PBS and 1% antibiotic/antimycotic (10 000 units penicillin, 10 mg streptomycin, and 25 mg Amphotericin B per ml; product A5955, Sigma–Aldrich Canada) was poured into the test tendon bath, to maintain hydration and prevent bacterial and fungal growth throughout testing. Clamps were tightened once more after adding the solution. The load cell was zeroed, and the translational stage was shifted away from the actuator, pulling the tendon taut. The stage was translated until a nominal tensile force of 0.1 N was reached, indicating that the tendon was no longer slack. The inter-grip length was measured (36 ± 2 mm) with a caliper. Photographs were taken from a side and top view of the tendon in the fully stretched, fully compressed, and mid-stroke positions (Figure 3.6).

Testing was initiated, subjecting tendons to 25 000 buckling cycles at a frequency of 1 Hz, using a compressive stroke length of 30 mm. A 5-second video of testing was taken from the top and side views to compare tests if necessary. Throughout testing, the matched-pair control sample remained in a separate bath containing a 100 mL solution of the same composition.

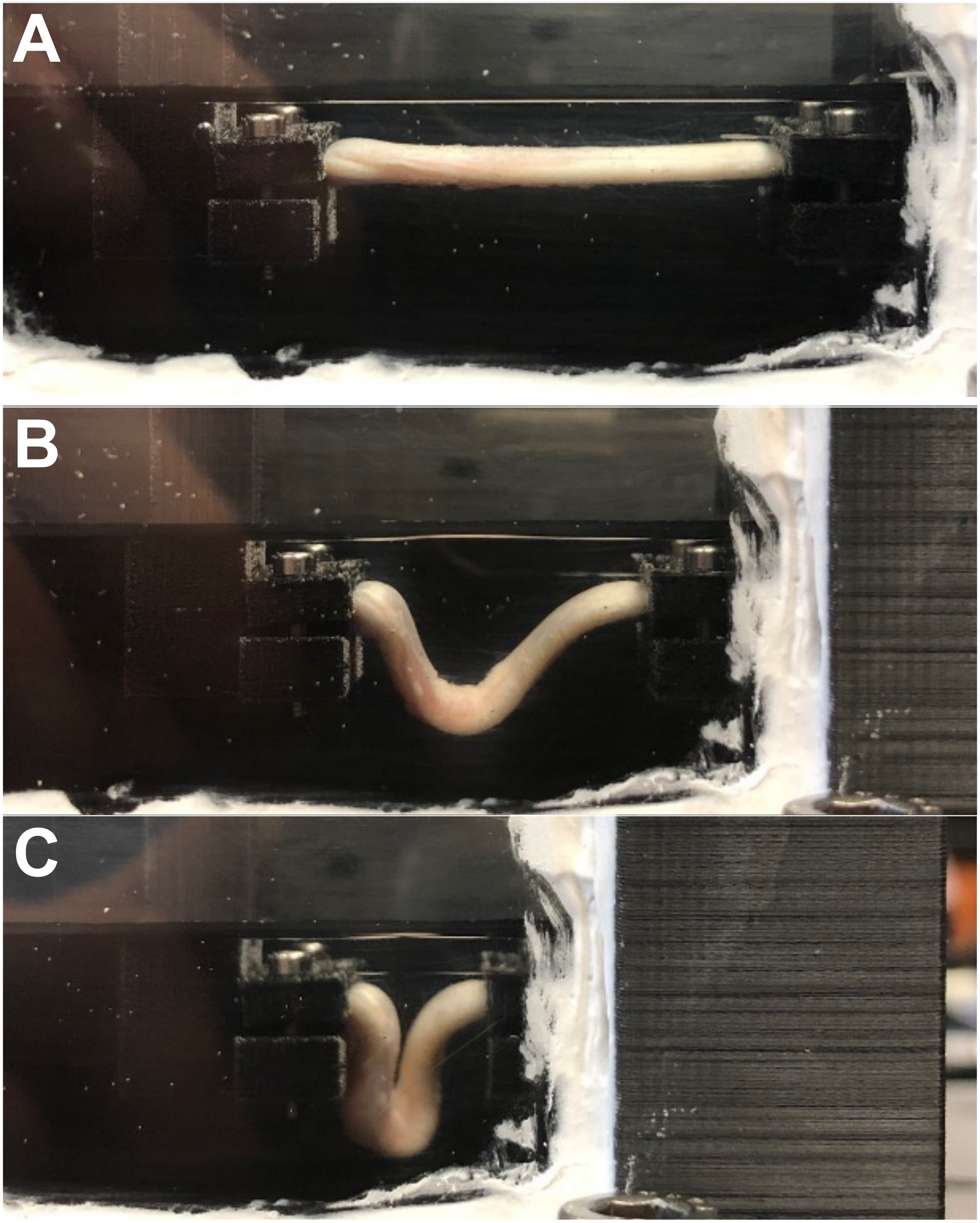

Figure 3.6: Side view of an SDF tendon clamped into the cyclic buckling apparatus. Images at three positions of the buckling cycle, (A) fully stretched, (B), mid-stroke and (C) fully compressed are shown.

Chapter 4: Structural Analysis – Imaging Techniques

4.1 Imaging Sample Preparation

Following cyclic buckling, a one-sided razor blade was used to remove a 12 mm portion of the test tendon, containing 6 mm on either side of the buckling axis (the line of the tendon that experienced the greatest change in altitude through buckling). Additionally, a 12 mm portion of the control tendon was also removed. Under a fume hood, the test and control tendons (n = 5 pairs per tendon type) were placed in separate 15 mL Falcon tubes, filled with 10 mL of 10% formalin. Tendons were left in the fixative for 60 hours[113,114].

After 60 hours, tendons were removed from the formalin solution and placed in the first well of a 12 well plate, filled with double distilled water (ddH_2O). The well plate was placed on a shaker table on a medium-low setting for 15 minutes. The tendons were then moved to wells containing fresh ddH_2O and shook twice more to complete the rinsing process.

Formalin fixed tendons were mounted on an aluminum block using optimal cutting temperature (OCT) compound and submerged in liquid nitrogen, in preparation for cryo-sectioning. The tendon orientation on the block was rotated 90° about the tendon's longitudinal axis, from the images in Figure 3.6, so the major diameter of the tendon, who's clamped ends were in the horizontal plane during cyclic buckling, now resided in the vertical plane, meaning each section would have undergone similar buckling. A sliding microtome (Leica SM2000 R) was set to a thickness of 5 μm and used to remove several sections of from every tendon, placing each in a separate well of a 24 well plate, filled with ddH_2O. The well plate was placed on a shaker table and shook for 15 minutes on a medium speed. The ddH_2O was replaced with clean ddH_2O after 15 minutes and the process was repeated, attempting to remove all OCT from the tendon sections.

One section from each tendon was then prepared for fluorescence microscopy and a second section was prepared for second harmonic generation (SHG) microscopy, as described in Chapter 4.2.3 and 4.4.3 respectively.

4.2 Fluorescence Microscopy

4.2.1 Background

Fluorescence microscopy is a powerful imaging technique that has evolved and broadened over the years. What started as one-photon excitation fluorescence has since expanded to include multiphoton excitation fluorescence, and more complicated non-linear microscopies[115]. The basic principles of fluorescence microscopy are derived from the concept of transmitting light of a specific wavelength to a sample and detecting the wavelengths of the emitted light[116].

In one-photon excitation epifluorescence microscopy, the process begins by directing light onto a sample[117]. When the wavelength of an incident photon and the absorption spectrum of a sample's fluorophore match, the fluorophore may absorb the photon, consuming its energy[116–118]. This surplus of energy excites the fluorophores electrons, temporarily raising them to a higher energy state[116–118]. Subsequently, the fluorophore has multiple potential outcomes. The first option is for the fluorophore to disperse the excess energy absorbed from the colliding photon to neighbouring molecules, as a transfer of heat, allowing the molecule to return to its electric ground state[115]. In this outcome, the excited state is exited very rapidly (several magnitudes faster than any other outcome), and this process does not result in the emission of a photon[115]. A second possibility is for the absorbing molecule to emit a phosphorescent photon. In this scenario the fluorophore remains in a high energy state for magnitudes longer than any other outcome, and once again does not result in the production of a fluorescent signal[115,117]. A third fate for the excited molecule is that the excess energy is emitted as a fluorescent photon, after remaining in an excited energy state for a period on the magnitude of nanoseconds[115,117]. The photon is emitted at a lower energy level and therefore has a longer wavelength than the absorbed photon, due to a phenomenon known as the Stokes shift[115].

To properly measure the fluorescent signal exerted by a molecule, the filtering of light is intrinsic. If no filter were applied to the incident or emitted light it would be impossible to differentiate signal produced by absorbed and emitted photons, or photons of different wavelengths, as no wavelengths would be restricted[116,117]. When light is directed at a sample, a bandpass filter restricts access of some photons to only allow those having wavelengths within the specified band to pass[116,117]. Similarly, the emitted light is filtered with center at a higher wavelength, blocking photons of the incident wavelength and only allowing fluorescent photons to pass and be detected[116,117].

While it is possible to image an unstained sample using fluorescence microscopy, staining techniques are regularly utilized[116,118]. Typically, a dye will contain some component capable of attaching to a specific molecule, cell, or structure[116,118]. The composition of this component will also involve a fluorescent probe to label the intended feature[116,118]. The fluorescent probe will have a known excitation and emission wavelength spectrum, allowing an optimal filter set to be selected[116,118]. When the sample is imaged, the fluorescent probe will emit far more fluorescent photons, intensifying the fluorescent signal produced by the tagged features relative to the rest of the sample[116,118].

Recently, a new product referred to as a collagen hybridizing peptide (CHP) has emerged on the market, helping to progress the field of tendon research[119–122]. The CHP is a synthetic peptide that mimics the Gly-X-Y repeat sequence of a natural collagen α-chain[122,123]. Utilizing hydrogen bonding, the CHP has a high affinity to bind to denatured collagen molecules as there are a plethora of potential binding sites. For the same reason, the CHP has a negligible affinity to bind to intact collagen molecules. Currently, three CHP products are commercially available from 3-Helix, two of which are labelled with a fluorophore. F-CHP has an excitation/emission of 494 nm/512 nm and R-CHP has an excitation/emission of 548 nm/563 nm.

The emergence of CHP staining of tendon samples over the last ten plus years has allowed research groups to use fluorescence microscopy to determine the amount of denatured collagen present in a tissue sample. A study by Lin et al.[124] set this framework by using a trypsin-hydroxyproline assay and CHP fluorescence to show that a linear relationship between CHP fluorescence and collagen denaturation exists[124,125]. This relationship has been used in several tendon loading studies to assess denaturation of collagen molecules, altering various loading conditions and factors.

Tensile loading at a specified strain rate or speed, to a particular strain or displacement, has been conducted by numerous research groups, loading both individual fibrils and fascicles of positional and energy storing tendons. Despite the differing animal models, loading factors, and hierarchical level undergoing tensile testing, the results of these studies using a CHP show similar results. Tendon molecules begin to denature at the yield point[104,126]. As the sample is loaded past the yield point, denaturation continues to increase[126–128].

Although fewer, some studies have looked at the relationship between denaturation of collagen molecules and cyclic loading. When cyclically loading rat tail tendon fascicles to stresses above the yield point, the denaturation of molecules was quickly observed, and increased with additional loading cycles[105]. Interestingly, when cyclically loading positional and energy-storing tendons of mice to rupture, using a lower stress for the maximum stress of each cycle, an additional result was observed. While positional tendons showed a significant level of denatured collagen molecules, the denaturation of energy-storing tendons was minimal[106].

Though some progress has been made, the lack of research on tendon molecular denaturation, resulting from mechanical loading (aside from tensile overload) under various conditions, raises some interesting queries. Will the results observed through cyclic loading of small animal tendons be transferable to larger animal models[29]? Are energy-storing tendons more resistant to denaturation than positional tendons, through cyclic loading? Is loading near or past the yield point of a tendon a necessary precursor for molecular denaturation? Or can denaturation occur with the absence of a tensile load?

4.2.2 Hypotheses and Rationale

The objective of this section was to investigate the molecular response of tendon to cyclic buckling. Both quantitative and qualitative assessments were utilized to measure the amount of denatured collagen between test, control, CDE and SDF tendons, and if there were any patterns of denaturation location, respectively.

Hypothesis (i): Following cyclic buckling, fluorescence microscopy will demonstrate an increased presence of denatured collagen in test tendons relative to their match-paired controls.

Rationale: Though much of the literature suggests denaturation may only occur after tissue yield[104,126,127], these studies typically do not consider cyclic loading and there has yet to be a study where tendons undergo strictly cyclic buckling.

Hypothesis (ii): Following cyclic buckling, fluorescence microscopy will demonstrate that a greater product of denatured collagen between test and match-paired control exists in CDE tendons, compared to SDF tendons.

Rationale: Based on the in vivo function of the two tendons, SDF tendons are more adept to cyclic loading[30,42,102].

Hypothesis (iii): In all tendons used in this study, kinkbands observed through polarized light microscopy will often display a heightened fluorescence signal along the center of the kinkband.

Rationale: Some structural damage must occur when a fibril is kinked, it is unclear as to what hierarchical level that happens at yet.

4.2.3 Methodology

<u>Experimental</u>

Following cyclic buckling (Chapter 3.4) and cryo-sectioning (Chapter 4.1), one section for each of the test tendon and matched-pair control tendon underwent preparation for fluorescence microscopy, following the outlined R-CHP protocol (R-CHP, 3Helix Inc., Salt Lake City, UT). First, 180 μL of PBS was pipetted into a 600 μL microcentrifuge tube and brought to 80 °C in a dry block heater. Once the PBS was measured at a steady temperature (two measurements spaced a minimum of 15 minutes apart) of 80 °C, 20 μL of a 100 μM R-CHP stock solution was pipetted into the microcentrifuge tube containing PBS, diluting the R-CHP stock solution to a concentration of 10 μM. The new 10 μM, 200 μL R-CHP solution remained in the dry block heater at 80 °C for 5 minutes to unfold the CHP into monomeric α-strands. Throughout this process, the dry block heater was covered in aluminum foil to minimize photobleaching of the fluorophores. After 5 minutes, the microcentrifuge tube was immediately submerged in an aluminium foil covered ice bath for 80 seconds to quench to room temperature. The microcentrifuge tube was then centrifuged for approximately 20 seconds to collect any condensation in the tubes, again, keeping the centrifuge covered in aluminum foil. The 200 μL of R-CHP solution was evenly pipetted into 2 wells of a 48 well plate (100 μL per well). One section from a test tendon was carefully placed in one of the two wells, using tweezers, and one section from the match-paired control tendon was placed in the other well, ensuring each section was fully submerged in the R-CHP solution. The well plate was wrapped in aluminum foil and placed in a 4 °C refrigerator overnight, for approximately 20 hours.

The following day, the well plate was removed from the refrigerator and the R-CHP solution was pipetted out of each well, replacing it with 400 μL of PBS. The well plate was again covered in aluminum foil and shook at a medium setting on a shaker table for 5 minutes, rinsing any excess R-CHP α-strands from the tissue. After 5 minutes, the PBS was replaced and the process was repeated, rinsing the sections a total of three times. Using Hydromount (Cat # 17966: Electron Microscopy Sciences, Canada) as a mounting medium, each section was wet mounted onto a 1 mm thick glass microscope slide and covered with a 0.13-0.17 mm thick cover slip. Slides were placed in a slide box, wrapped in aluminum foil, and stored in a dark cupboard.

Imaging was conducted in the Cellular and molecular digital imaging (CMDI) facility, at Dalhousie University. Imaging was conducted using the Zeiss Axio Imager Z2, an upright confocal one-photon excitation epifluorescence microscope. It was equipped with an HXP 120V mercury short-arc lamp, utilized as the light source, emitting broadband light. Light passed through a Zeiss Lumar 50 filter set (excitation: 30 nm bandpass filter centered at 640 nm, emission: 50 nm bandpass filter centered at 690 nm), filtering transmitted light to match the R-CHP excitation spectrum. After the sample absorbed the transmitted light and emitted photons, the same filter set filtered emitted fluorescent photons to match the emission spectrum of the R-CHP fluorophore. The filtered light was collected by a detector, contained within an Axiocam 506m_S1975 monochrome camera. To collect and process images, Zen Blue 2.6 software was used. All samples followed the sample imaging protocol. Using the attached brightfield microscope with a 10x magnification lens, the tissue was located. The Alexa Fluor 555 reflector channel, most closely mimicking the excitation/emission of the R-CHP fluorophore, was first used with the 5x magnification lens to take a series of images using a 50 ms exposure time. These images were stitched together to create a map of the tissue. The tissue was then outlined with a tracing tool to indicate the desired imaging region. The 10x magnification lens (0.3 numerical aperture) was switched into place and a series of images were taken by the software in a grid/tile format, shifting 70% of the focal view laterally after each image and then shifting up or down 70% to the next row after reaching the end of the tissue outline. At each image location, a fluorescence and differential interference contrast (DIC) image were taken, each using an exposure time of 50 ms. Once the full tissue area was imaged, the images were stitched together, fusing 10% of the overlap between adjacent images.

Data Analysis

The fluorescence data analysis was conducted using two quantitative approaches (1 and 2), where approach 1 contained two subparts (a and b). It was important when using both approaches to only compare fluorescence intensities between match-paired samples, to minimize experimental error. Although all samples underwent the same staining protocols, the match-paired samples were stained together, under the exact same conditions and duration, meaning their base tissue fluorescence was the most similar. When comparing match-paired samples to other samples, the base fluorescence level was not always similar, which would heavily skew the results. In approach

1 (a), the 10% of tissue area with the greatest intensity on a given section was isolated and the mean intensity of that 10% was computed. For approach 1 (b), the same protocol was utilized, but isolating the 5% of tissue area with the greatest intensity. For approach 2, the control was considered first. It was assumed that 1% of the control tissue was denatured[106], observed as the 1% with the greatest intensity. The minimum intensity of pixels in the control top 1% were then used as a threshold for denaturation. The same threshold was applied to the match-paired test and the percent of denatured tissue in the test was recorded.

The first step for both approaches was to determine which pixels of each fluorescence image were tissue and which ones were background[115]. To do this, the histogram of pixel count vs. fluorescence intensity was utilized. Using an RGB scale, where an intensity of 0 represented black and 16384 represented white, the intensities were grouped into a bin size of width 1. As seen in Figure 4.1, this histogram had a bimodal distribution, with the mean of the first peak occurring near an intensity of 100. The first peak represented background and all pixels below the threshold to exceed this peak were removed. The threshold for determining which pixels corresponded to tissue was set where a decrease in intensity less than 5000 was observed between neighbouring bins, 3 subsequent times (Figure 4.1). Since matched pairs were analyzed together, the sample with the larger intensity threshold for base tissue fluorescence was used for both test and control.

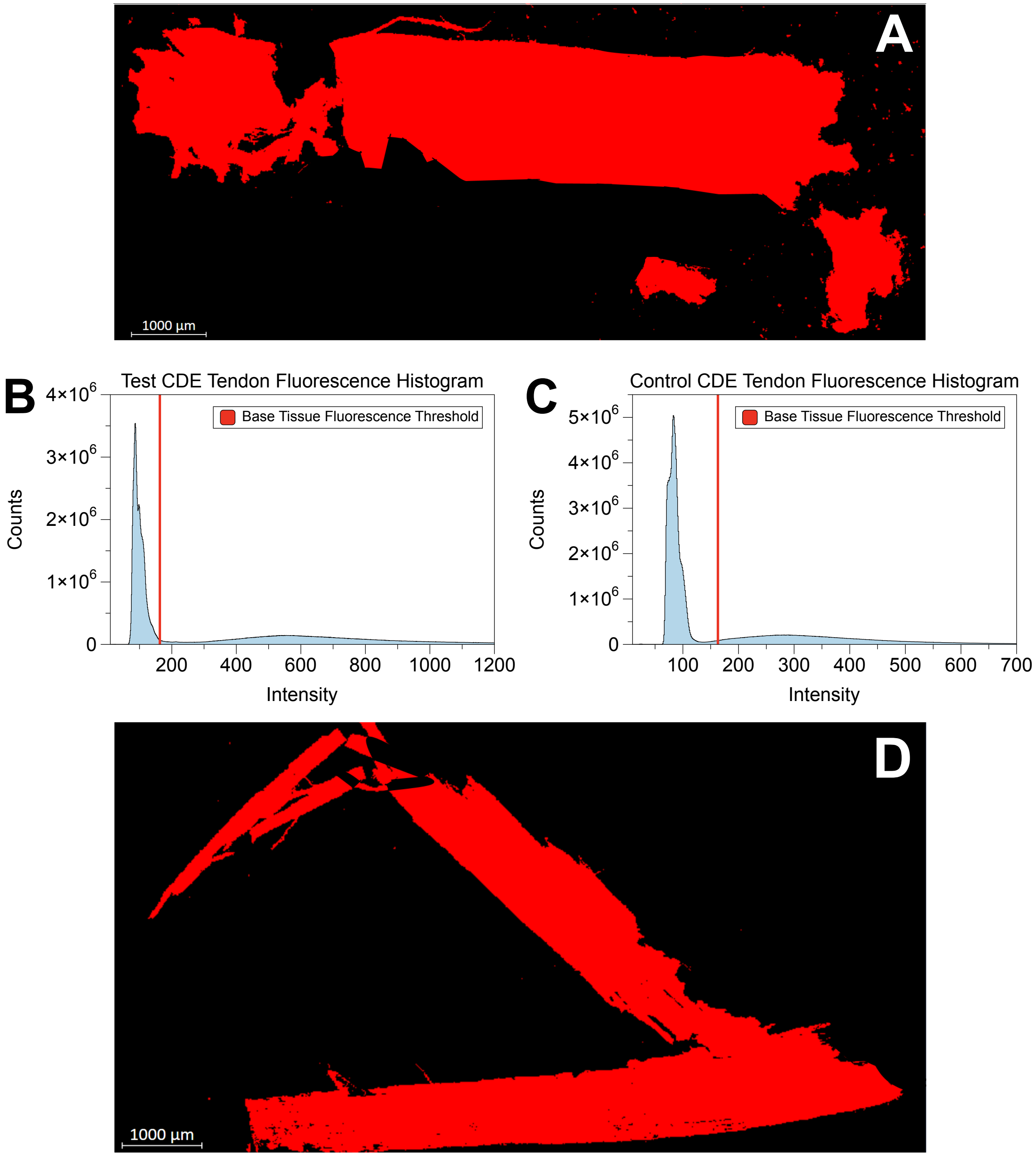

Figure 4.1: This figure shows an example of the process to determine which pixels were tissue vs. background. (A) The fluorescence image of a CDE test tendon, where all pixels representing tissue, regardless of intensity, are red and all other pixels are black. (B) The histogram of photon counts vs. pixel intensity for the fluorescence image in (A), where the intensity peak on the left represents background and the gaussian distribution in the middle is the tissue. The vertical red line, located

at an intensity of 163 in both histograms, represents the minimum intensity for a pixel to be considered tissue in these two matched-pair sections. (C) This panel shows the histogram of the match paired CDE control tendon, whose fluorescence image is shown in panel (D).

For approach 1a, the total tissue area was divided by 10, to determine the number of pixels in 10% of the tissue. The lower intensity threshold was increased until the number of pixels above the threshold reached the number of pixels equivalent to 10% of the tissue (Figure 4.2). The mean pixel intensity was recorded, and this process was repeated for the other match-paired tendon. The same procedure was repeated for approach 1b, although this time the total tissue area was divided by 20, to obtain the number of pixels in 5% of tissue (Figure 4.3).

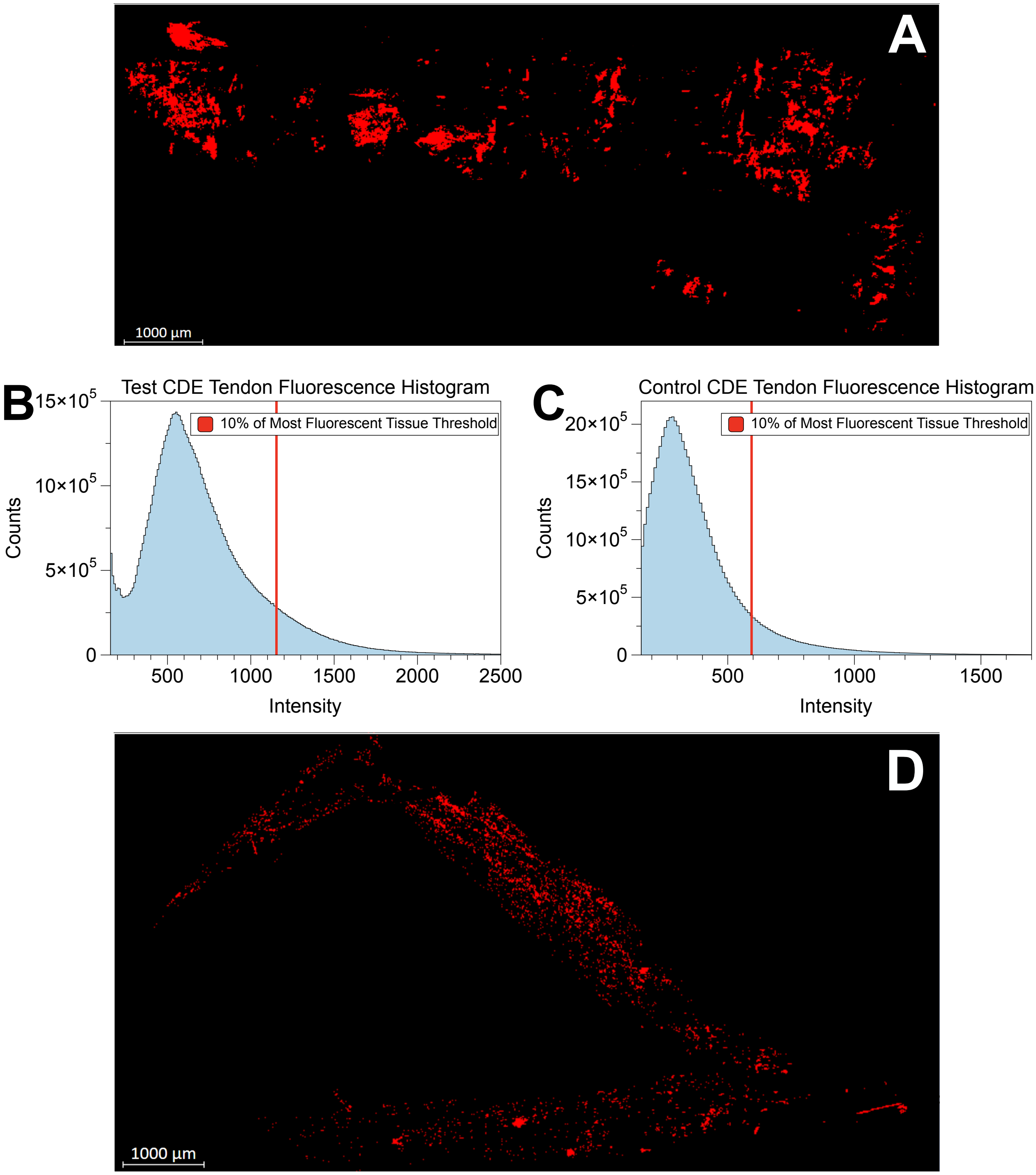

Figure 4.2: This figure shows an example of the process to determine the 10% of pixels with the greatest intensity. (A) The fluorescence image of a CDE test tendon, where all pixels representing the 10% of tissue with the greatest intensity, regardless of the value, are red and all other pixels are black. (B) The histogram of photon counts vs. pixel intensity for the fluorescence image in (A), where the x-axis of the histogram is bound on the left by the tissue intensity threshold. The vertical

red line, located at an intensity of 1154, represents the minimum intensity of the top 10% of tissue pixels. (C) This panel shows the histogram of the match paired CDE control tendon, where the vertical red line for the top 10% of the control is at an intensity of 594. (D) The fluorescence image of the histogram in panel (C).

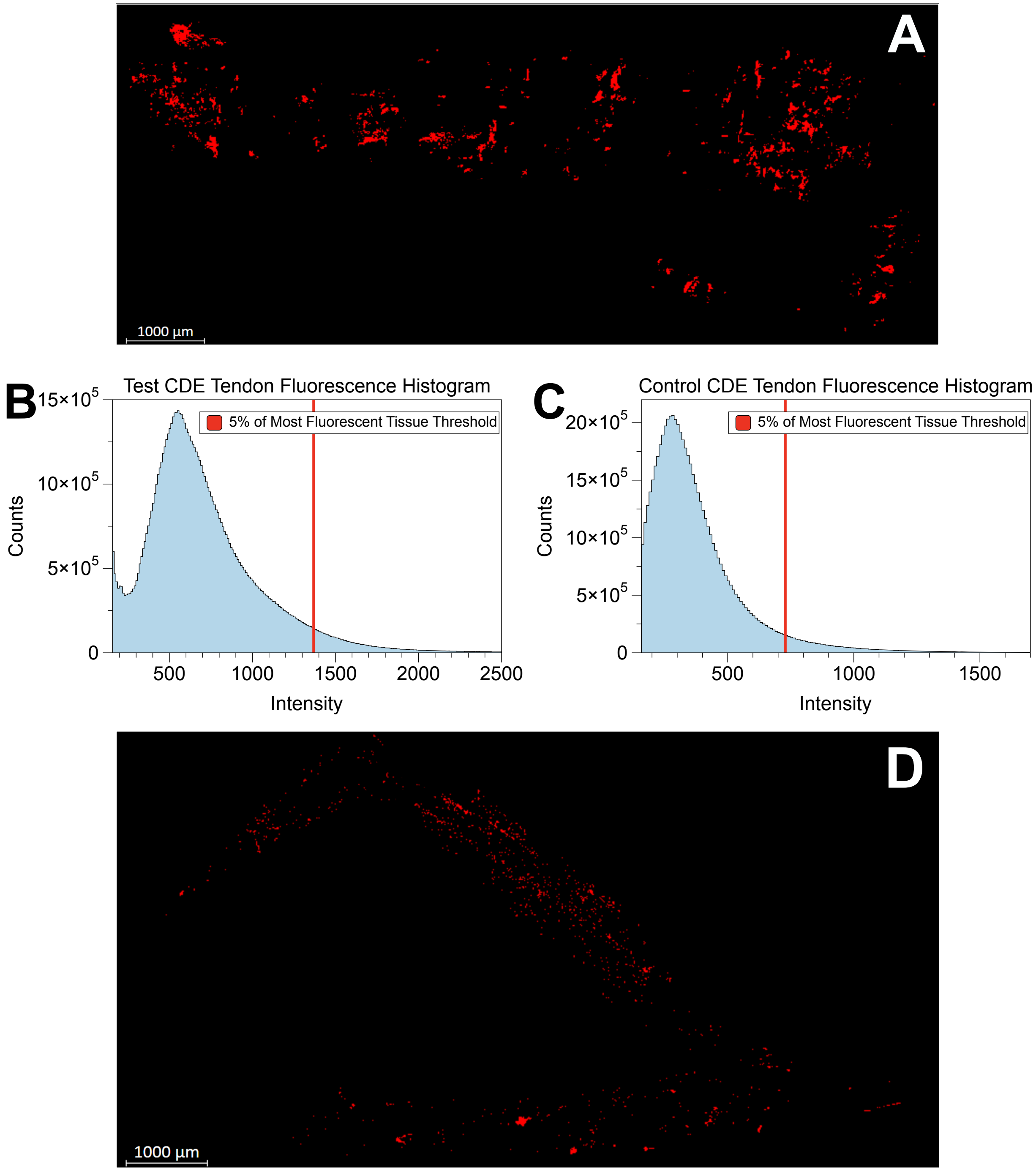

Figure 4.3: This figure shows an example of the process to determine the 5% of pixels with the greatest intensity. (A) The fluorescence image of a CDE test tendon, where all pixels representing the 5% of tissue with the greatest intensity, regardless of the value, are red and all other pixels are black. (B) The histogram of photon counts vs. pixel intensity for the fluorescence image in (A), where the x-axis of the histogram is bound on the left by the tissue intensity threshold. The vertical red line, located at an intensity of 1368, represents the minimum intensity of the top 5% of tissue pixels. (C) This panel shows the histogram of the match paired CDE control tendon, where the vertical red line for the top 5% of the control is at an intensity of 729. (D) The fluorescence image of the histogram in panel (C).

For approach 2, the total tissue area of the control in each pair was divided by 100, yielding the number of pixels in 1% of tissue. The lower intensity threshold was raised until the 1% of tissue with the greatest intensity remained. For this approach, the intensity at the threshold was recorded, rather than the mean intensity above the threshold. The same intensity threshold of the control was then applied to the match paired test and the percentage of test tissue above the threshold was determined (Figure 4.4).

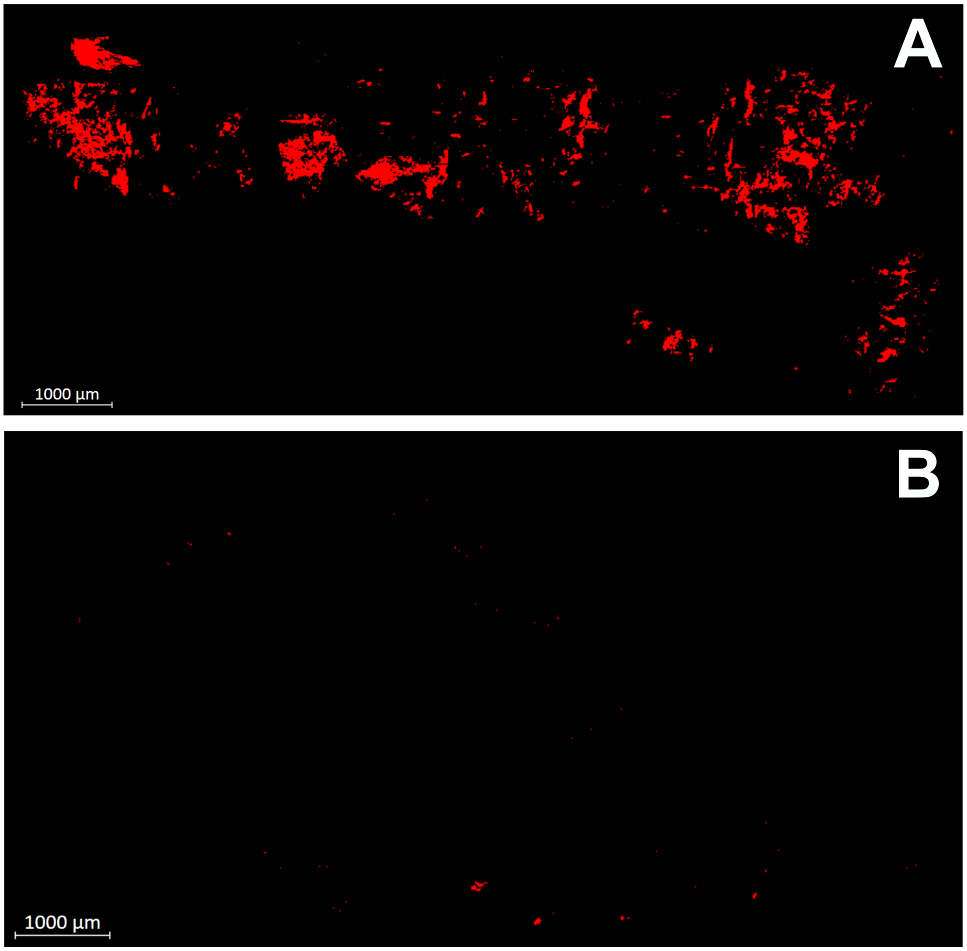

Figure 4.4: Fluorescence image comparing (A) the percentage of denatured tissue in the test and (B) match paired control tissue. All pixels having an intensity above the threshold for the top 1% of the control are red, and all other pixels are black. (A) Of the test tendon area, 11.0% is denatured. (B) The control tissue is 1.0% denatured.

Following the quantitative analyses, a qualitative analysis was conducted to determine if locations considered to be kinkbands when looking at the corresponding PLM image, exhibited increased fluorescence levels.

Statistical Analysis

Statistical analysis was conducted using JMP (Version 17.1.0, SAS Institute, USA). For approach 1, a matched-pair two-tailed t-test between test and control was conducted on the data set, to assess differences resulting from cyclic buckling. Additionally, for approach 1, differences between tendon type were analyzed by taking the percent increase in fluorescence between a test and match-paired control and running a two-tailed t-test, with tendon type as the factor. For approach 2, effect of treatment method was assessed by ranking the test data and running a Signed-Rank test. To investigate the effect of tendon type, the data was separated by tendon type, ranked, and a Wilcoxon test was performed.

4.2.4 Results

For approach 1, the matched-pair two-tailed t-test for both the 10% (p = 0.0451) and 5% (p = 0.0446) of tissue with the greatest intensity displayed a significant difference between test and control mean pixel intensity (Figure 4.5). However, the results of the pooled two-tailed t-test showed there was not a significant difference in percent increase of intensity from test to control, regarding tendon type (Figure 4.6), for neither the top 10% (p = 0.7636), nor the top 5% data (p = 0.7972).

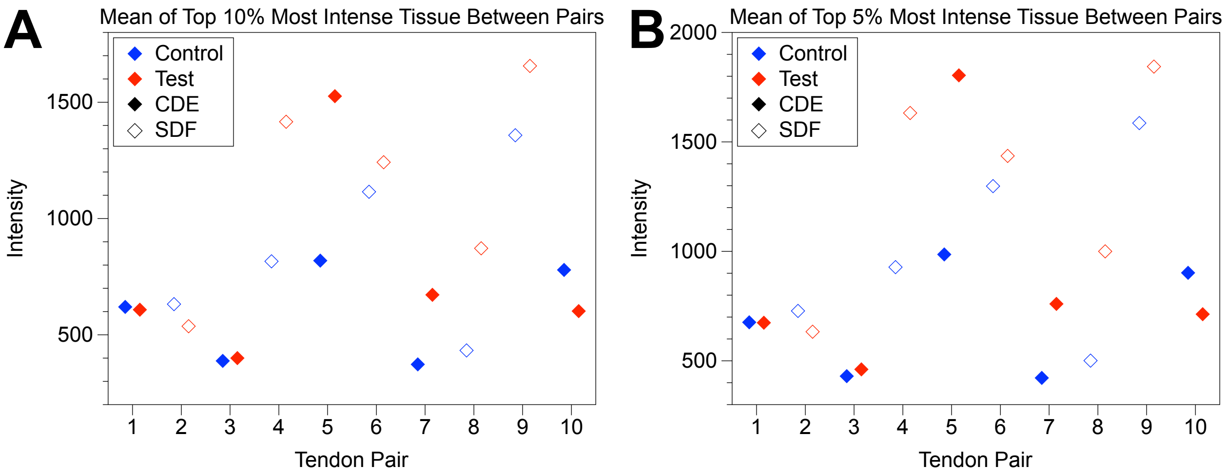

Figure 4.5: (A) Each diamond represents the mean intensity of the 10% of pixels with the greatest intensity for one sample. A test and control diamond located above the same number on the x-axis, for tendon pair, indicates the two diamonds are matched pairs. (B) This plot is the same as plot (A)

but considering the 5% of pixels with the greatest intensity. Both panels show that for 7/10 tendon pairs, the mean fluorescence of the test was greater than the control for the top 10% and 5% of tissue.

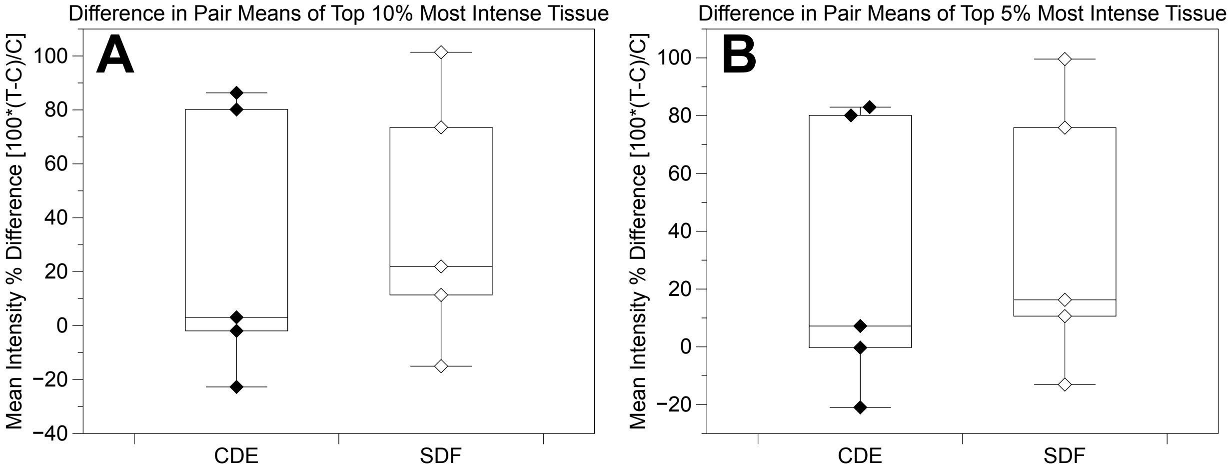

Figure 4.6: (A) Using the mean intensity of the top 10% of pixels, one value was calculated for each tendon pair, by taking the test mean minus the control mean intensity and dividing it all by the control mean intensity, to determine the percent difference between the two, with the positive convention meaning the test mean was larger. There was no difference (*p* = 0.7636) in percent increase in denaturation between CDE (29.0 ± 50.5 [%]) and SDF (38.6 ± 47.6 [%]) tendons. (B) This plot is the same as plot (A) but considering the 5% of pixels with the greatest intensity. Again, there was no difference (*p* = 0.7972) in percent increase in denaturation between CDE (29.8 ± 48.3 [%]) and SDF (37.9 ± 47.6 [%]) tendons.

Approach 2 showed the percentage of test tissue meeting the minimum intensity of the control top 1% to be significantly greater than 1%, using the Signed-Rank test (*p* = 0.0371), as displayed in Figure 4.7. As observed in approach 1, tendon type, was again not found to be a significant factor, using the Wilcoxon test (*p* = 0.5309).

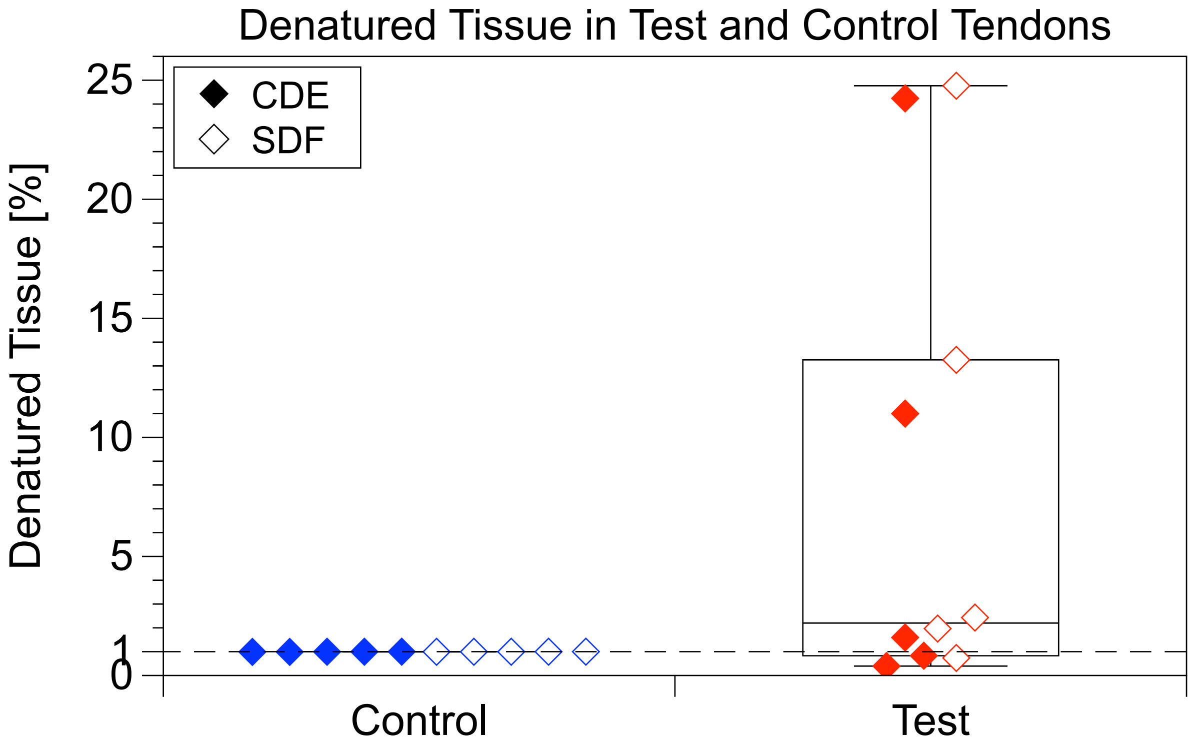

Figure 4.7: This plot compares the percentage of denatured tissue between test and control samples, assuming 1% of the control tissue to be denatured[106]. The horizontal dashed black line represents the denaturation level. Though 3/10 test samples fall below this line, a mean test denaturation of 8.1% shows a significant increase relative to the controls.

Upon visual inspection of identified kinkbands, there did not appear to be an increase in denaturation at the regions of kinkbanding. In some cases, portions of the kinkband had a more intense signal than the base tissue, however, the increase seemed to be dispersed across the tissue rather than specifically propagating along the kink. No evidence was present to suggest that the observed localized denaturation around the kinkband differed from localized denaturation observed at other tissue locations not near a kinkband.

4.3 Polarized Light Microscopy

4.3.1 Background

Polarized light microscopy (PLM) is a form of optical microscopy often utilized in quantitative and qualitative studies. The many benefits of PLM include its cost effectiveness and simplistic nature, making it a common choice when high magnification images on the nano or molecular scales are not required[129]. Additionally, PLM provides insight to the changes of a structure's orientation, thickness, and birefringence[130,131]. As the orientation of points on a specimen change relative to the direction of polarized light, their colour and intensity follows[130,131]. These qualities enhance the effectiveness of PLM when interacting with stagnant[132,133] anisotropic structures[134], making its value as a microscopy technique optimal when imaging tendon cryosections.

PLM functions as follows. First, a light source located at the bottom of an upright microscope is directed upwards towards a sample. Located between the light source and the sample is a polarizer. As unpolarized light passes through the polarizer, only light waves oscillating in a specific direction, known as the direction of polarized light, are allowed through. This linearly polarizes the light by blocking light travelling in any other plane[135]. When the polarized light contacts an anisotropic sample, the emerging light is split into two components, oscillating in perpendicular planes[129,136]. These two components (ordinary and extraordinary wavefronts) travel with different phase speeds, until they reach the analyzer. The analyzer is a second polarizing filter, typically oriented perpendicular to the polarizer, meaning that in the absence of a sample, negligible light will be observed through the eyepiece[129,135]. As light from the two components passes through the analyzer, it is brought back into phase via constructive and destructive interference[137]. The resulting recombined light rays are then viewed through an eyepiece or camera.

When multiple locations of a sample differ in colour, the conclusion can be drawn that the incident polarized light interacted differently with each sample location, resulting in a unique interference pattern[129,131,137]. One optional component often added to a PLM setup is a wave plate. Wave plates, existing as one half, one quarter, and multiples thereof, apply a phase shift (of the amount indicated in the wave plate name) between the ordinary and extraordinary wavefronts[137]. By rotating the wave plate, specific features can be made more prominent, providing an enhanced contrast among the sample[138]. They are additionally beneficial for their ability to convert linearly polarized light to circularly polarized light when oriented properly[41,139].

The exploitation of PLM as a resource for imaging both stained[140] and unstained[10,38] collagenous structures has spanned more than half a century. In tendon research, the most significant benefits of PLM have been towards furthering an understanding of the fibre and fibril levels of the structural hierarchy. Specifically, the angle[41,141,142] and period[10,143] of crimp. The wave like structure of crimp is enhanced through PLM. Since the tissue orientation oscillates, some locations lay parallel and others perpendicular to the direction of incident polarized light, creating a pattern of alternating light and dark bands[142]. This ability of PLM to clearly display 90° changes in tissue direction becomes even more evident with sharper crimp[10,141,142], and potentially kinked tissue.

4.3.2 Kinkband Inclusion Criteria

The term kinkband has been well-studied in the field of material science, used to describe the buckling of fibrous materials[107,108]. When compressive forces are applied to a fibrous material, there reaches a point where the material can no longer support the load while still maintaining its structure. This results in a localized failure of a single fibre, in the form of a buckle, which then propagates to neighbouring fibres, creating a band of kinks. The fibrous structure of tendons has led to the use of this terminology in tendon literature[30,95]. However, the criteria for quantifying kinkbands have not been laid out. In this thesis, when a tendon was viewed through PLM, a feature was only considered a kinkband if it possessed both of the following:

(i) A change in colour between the suspected kinkband and the tissue on either side of it when following a line perpendicular to the direction of the kink.

A change in colour was recognized as a change of 10 or greater on a gray scale of 0 to 255 (an RGB difference of 3.9%).

(ii) A sharp change in tissue direction.

A change in direction was deemed sharp when the distance from the center of the suspected kinkband (peak or trough gray scale value), to the point where a colour change was observed, measured no more than 1μm.

An iterative process was utilized to refine the kinkband inclusion criteria to its final state, defined above. In each iteration, a broad spectrum of commonly observed PLM features were selected to challenge its efficacy. For each case, a feature was identified on a PLM image. The selected region was then magnified. As stated in the criteria, a line was drawn perpendicular to the direction of kinking. To determine whether the criteria was met, the plot profile of the line was viewed. The following paragraphs and figures illustrate some of the features that were and were not considered kinkbands using the above inclusion criteria.

In the first case (Figure 4.8), an example of a very sharp change in tissue direction was considered. Here, a visual assessment of the entire PLM image clearly warranted further investigation. When magnifying the image and assessing the plot profile, the trough of the plot profile was found at 6.97 μm from the left, having a gray scale value of 76.7. Moving along the perpendicular line, a change in gray scale value of 10 occurred over the shortest distance (0.63

μm) when translating left. As the distance required to meet the first condition of the criteria occurred over a distance < 1 μm, the feature was confirmed as a kinkband following the above criteria.

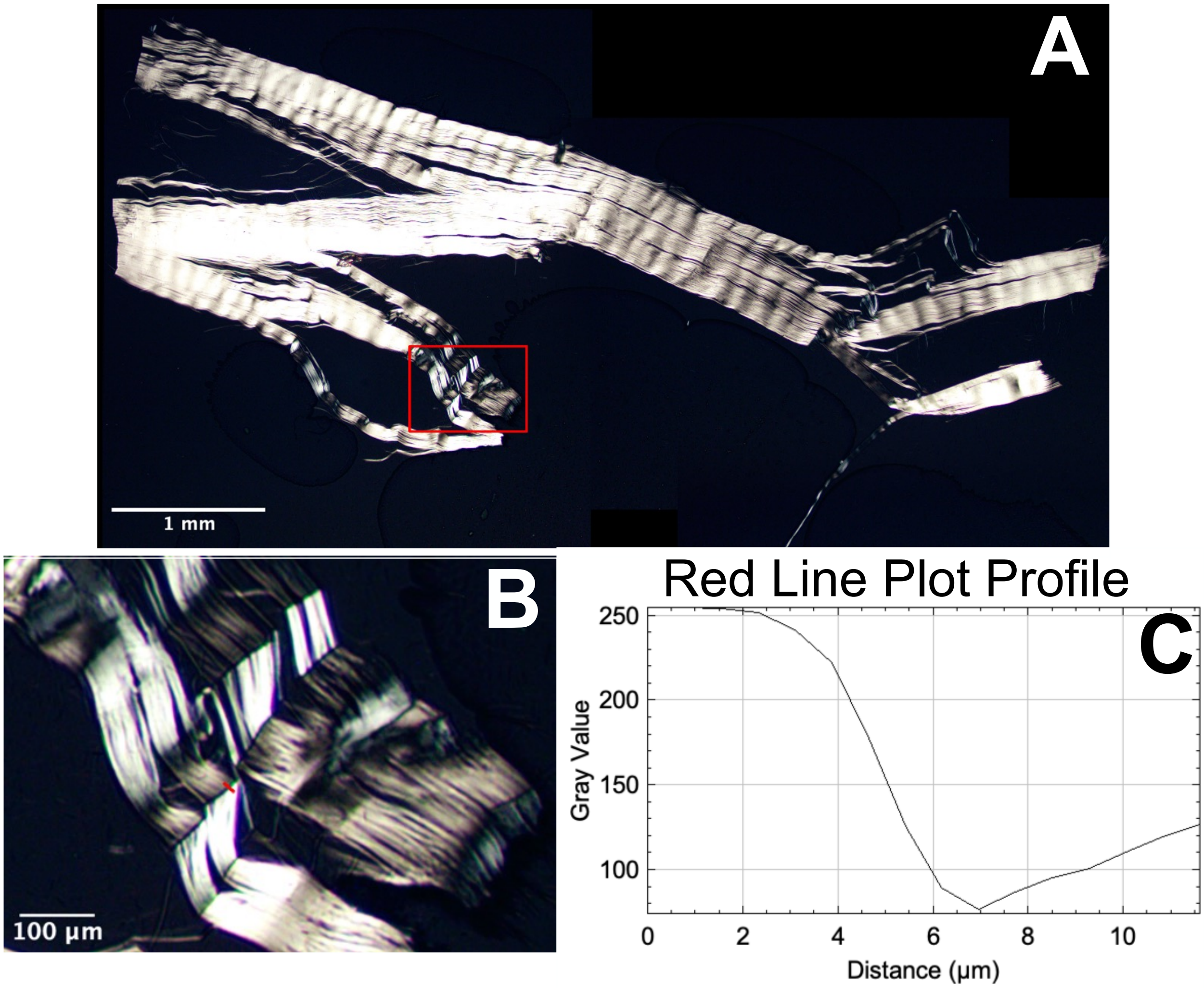

Figure 4.8: This figure shows (A) the PLM image of a CDE test tendon cross section, imaged with a 4x objective lens. (B) The region of interest contained in the red box in panel (A) is magnified. A red line is drawn across the width of one of the kinkbands. (C) The corresponding plot profile of the red line drawn from left to right across the magnified image, shows that the suspected kinkband has a width of 0.63 μm from the trough of the profile plot to an increase of 3.9% on the RGB scale and is therefore a confirmed kinkband.

While the first case was clear, some features challenging the kinkband inclusion criteria had a much closer result. The second case (Figure 4.9) was one previously observed in the literature[142] in the linea alba of rats. Here, the tissue appeared different from typical crimp but not as sharp as the kinkband in the first case. When investigating this feature, the plot profile of a perpendicular line showed there to be a change in the gray scale value of 10, satisfying the first condition. However, this changed occurred over 1.32 µm, which was greater than the 1 µm threshold required to satisfy the second condition, therefore failing to meet the kinkband criteria.

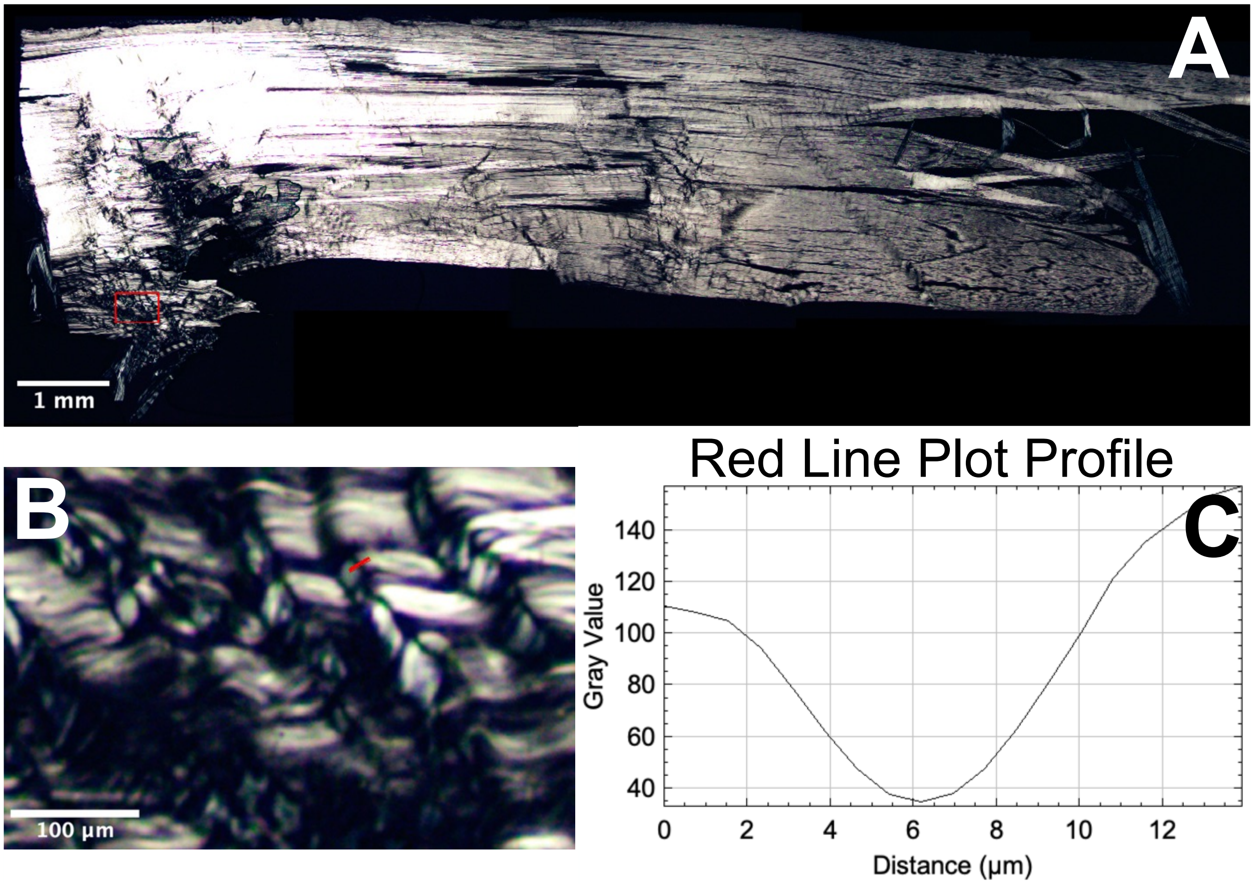

Figure 4.9: (A) The PLM image of a SDF test tendon cross section, imaged with a 4x objective lens. (B) The region of interest on the PLM image boxed in red is magnified, at a location where suspected kinkbands exist. (C) The corresponding plot profile of the red line drawn from left to right in (B) shows this feature is not a kinkband.

In the third case (Figure 4.10), an initial visual assessment suggested the flagged feature had the potential to be a kinkband. When magnifying the image and looking at the plot profile across the feature's width, at various longitudinal locations, it was observed that the first condition was met along the entire length. Though, the second condition was only met along a portion of the feature's length. The red lines in panel B of Figure 4.10 were drawn where the feature had a width of 1 μm, when meeting the first condition. The blue line, located outside of the kinkband region, was drawn where the feature had a width of 1.5 μm, and therefore did not meet the kinkband criteria. In this case, a kinkband was still present, as shown by the green line drawn where the feature had a width of 0.8 μm, but only along the portion of the suspected region contained within the red lines.

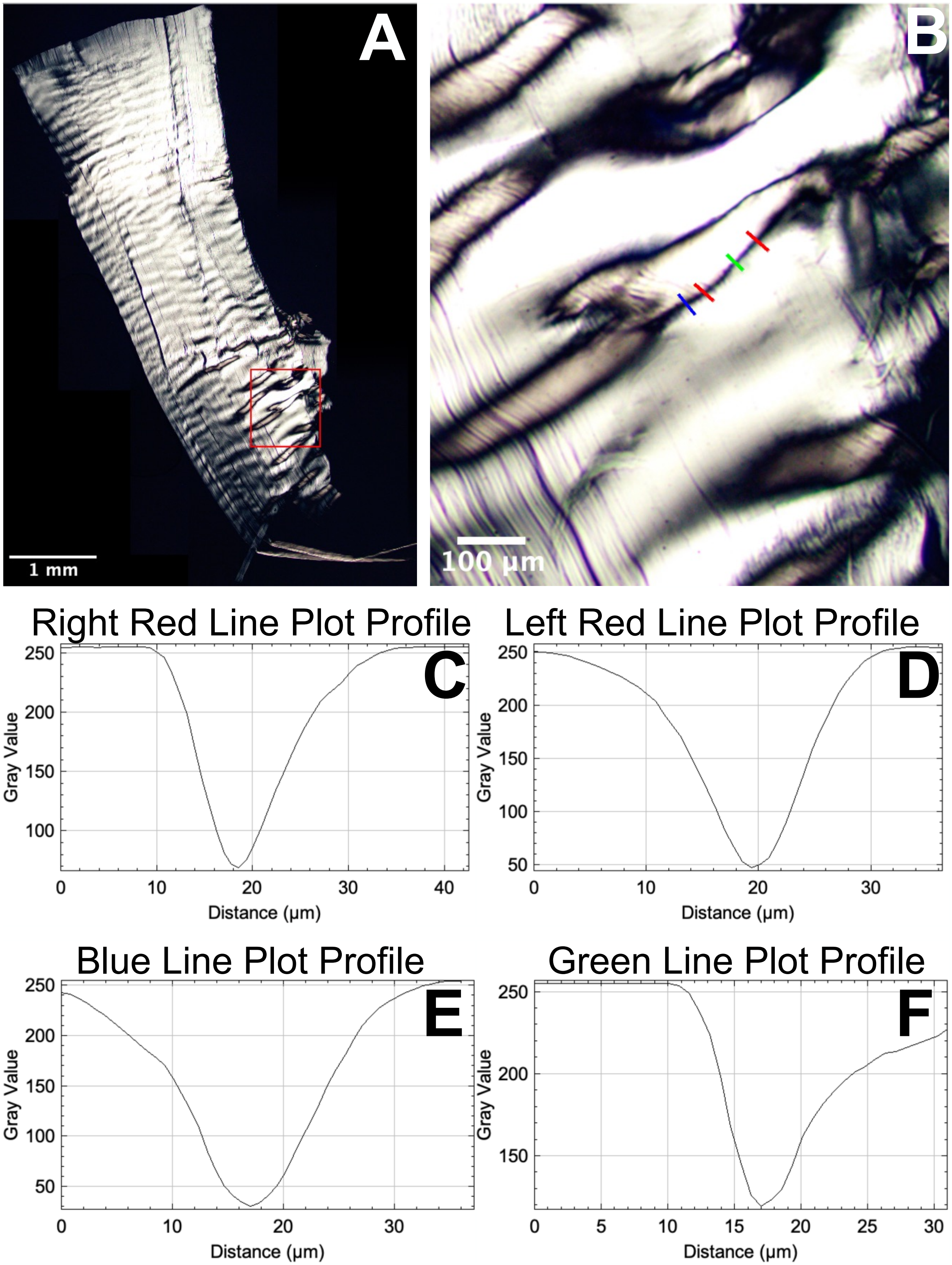
A
1 mm
B
100 µm
Right Red Line Plot Profile
C
Left Red Line Plot Profile
D
Blue Line Plot Profile
E
Green Line Plot Profile
F
Gray Value
Distance (µm)
250
200
150
100
50
0
5
10
15
20
25
30
40

Figure 4.10: (A) The PLM image of a CDE test tendon cross section, imaged with a 4x objective lens. (B) The PLM image is magnified at the region of interest denoted by the red box in panel (A). There are four lines drawn on the image in panel (B), all of which have their profiles plotted. (C) This plot profile corresponds to the right red line drawn indicative of one end of the kinkband. (D) This plot profile is of the left red line, indicating the other end of the kinkband. (E) The blue line plot profile shows that this region of tissue no longer meets the kinkband inclusion criteria. (F) The green line plot profile shows a sharp kinkband.

4.3.3 Hypotheses and Rationale

The objective of this section was to quantify the effect of cyclic buckling on the presence of kinkbanding, while comparing the susceptibility of CDE and SDF tendons to kinkband formation. An additional objective was to provide supplementary data for the other imaging techniques used.

Hypothesis (iv): The kinkband presence observed in tendons subject to cyclic buckling will be greater than that observed in the controls.

Rationale: Based on the literature[95,99], there is reason to believe that cyclic buckling of tendons does not require a tensile component to induce kinkbanding.

Hypothesis (v): Among the cyclically buckled tendons, the CDE tendons will have a greater kinkband presence than the SDF tendons.

Rationale: Positional tendons, such as the CDE tendon, are not as resistant to fatigue[42,144].

4.3.4 Methodology

<u>Experimental</u>

PLM images were taken of all sections being imaged through both fluorescence and SHG microscopy. To avoid photobleaching of fluorescence slides, PLM images were taken following fluorescence microscopy and were used to form a criterion for discerning which pixels represented tissue. For slides subjected to SHG microscopy, PLM images were taken prior, to identify target locations for scanning. Additionally, PLM images of the fluorescence microscopy slides were used to quantify kinkband presence.

PLM images were taken using a Nikon Eclipse E600 light microscope. The two polarization filters (polarizer and analyzer) used were part of the First Order Red Compensation Set for Gout Screening, provided with the microscope. To enhance image quality, a half wave plate was located between the sample stage and analyzer. To view and capture images, an AmScope MU1400 digital microscope camera together with AmLite software (2023) was utilized. To fully capture each tissue section, a series of images were taken using a 4x objective lens (0.1 numerical aperture) and manually stitched together with Adobe Photoshop.

Data Analysis

Using the kinkband inclusion criteria outlined in Chapter 4.3.2, the total kinkband presence of each section was determined. Fluorescence microscopy slides were utilized for this analysis since the total tissue area was already known. PLM images were opened using ImageJ (Version 1.53t). A scale was set by measuring the distance between two features on the fluorescence image and drawing a line between the same features on the PLM image.

Starting in the top left corner, images were scanned top to bottom for features resembling the characteristics of a kinkband. If none were present, the frame of reference was shifted to the right and the image was searched top to bottom again. This process was repeated until the entire image had been thoroughly searched. When a potential kinkband was observed, it was further investigated by drawing a line perpendicular to the direction of kinking and looking at the plot profile, using the criteria of Chapter 4.3.2. If a feature was confirmed as a kinkband, a line was drawn along its length (Figure 4.11), with the ends indicating the locations where the feature failed to meet the kinkband criteria. Once a line was drawn along the length of each kinkband on a tissue section, the kinkband presence was measured as a density, calculated as the ratio of total kinkband length to total tissue area.

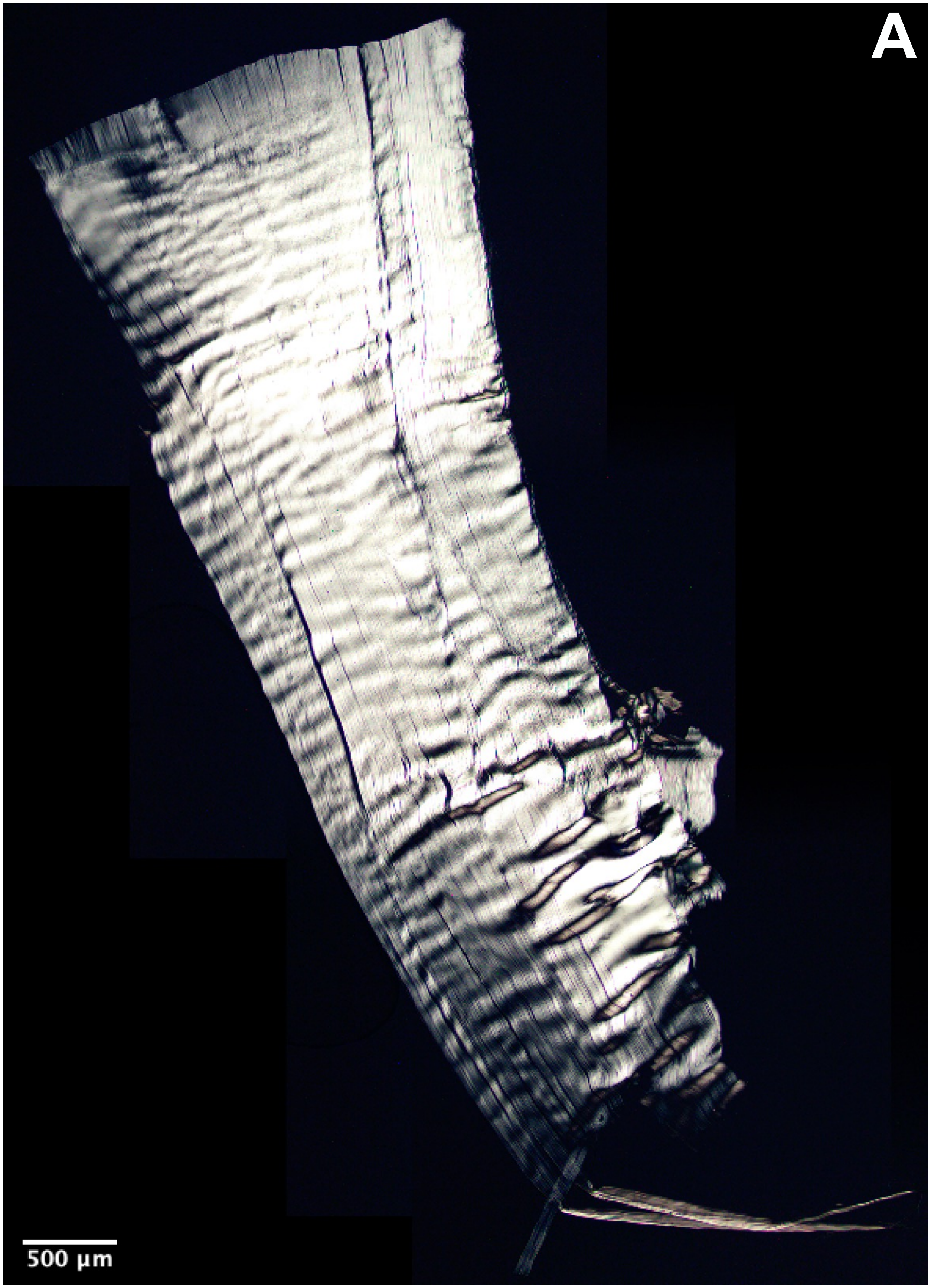
A
500 µm

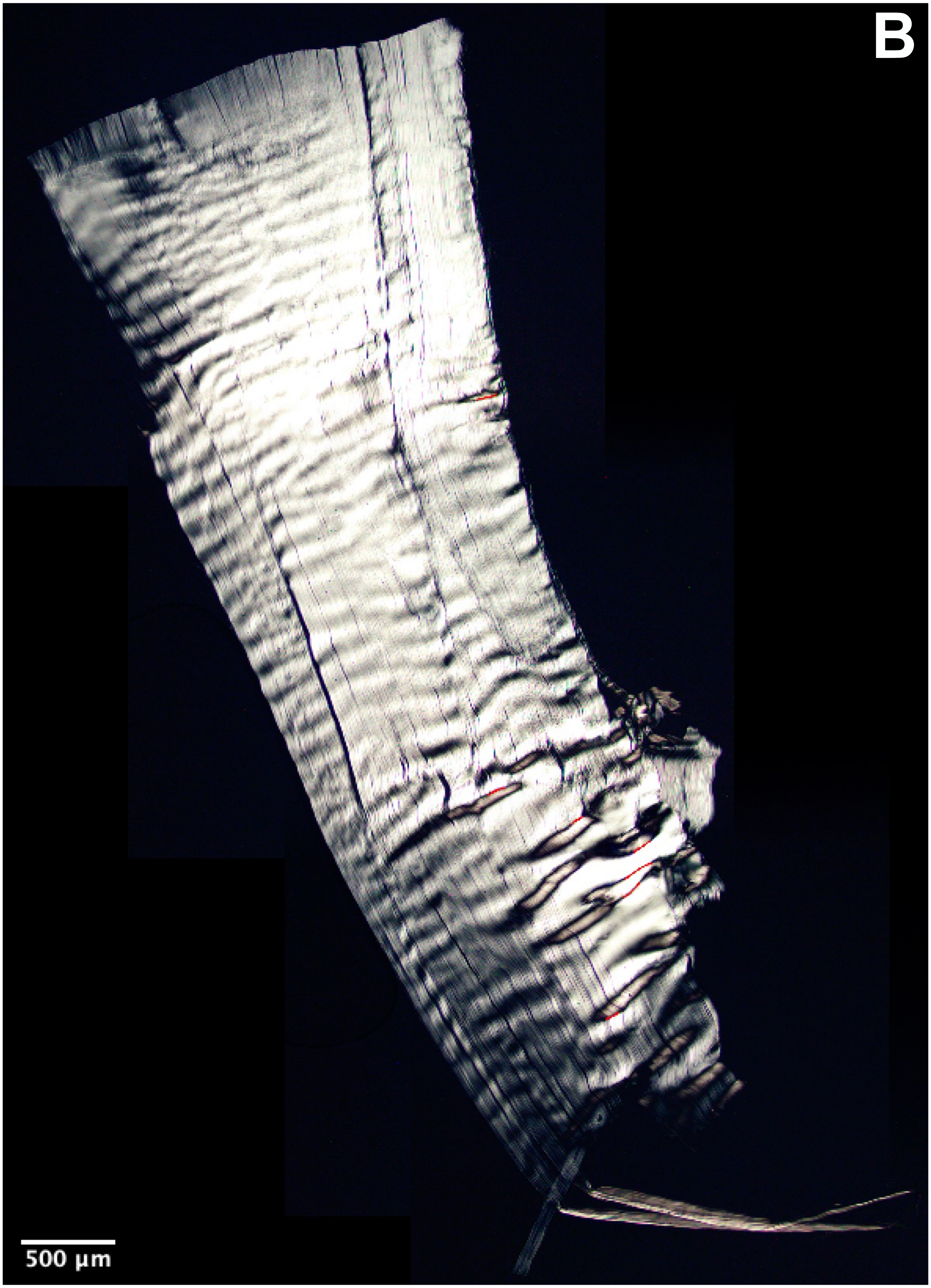
B
500 µm

Figure 4.11: (A) An unannotated PLM image of a CDE test tendon. (B) The annotated version of the PLM image in panel (A). Each red line in (B) indicates a kinkband, having a length equivalent to that of the line.

Statistical Analysis

Statistical analysis was conducted using JMP (Version 17.1.0, SAS Institute, USA). The kinkband density data was first rank transformed. The data was split by treatment method (test/control) and a one-way repeated measures ANOVA was conducted on the data, with treatment as the repeated measure and tendon type as the independent variable.

4.3.5 Results

A one-way repeated measures ANOVA found cyclic buckling of tendons to cause a significant increase in kinkband density, relative to the control group (p = 0.0140), as shown in Figure 4.12. Tendon type had no effect on the level of kinkbanding occurring, with both CDE and SDF tendons having a similar kinkband density (p = 0.7279).

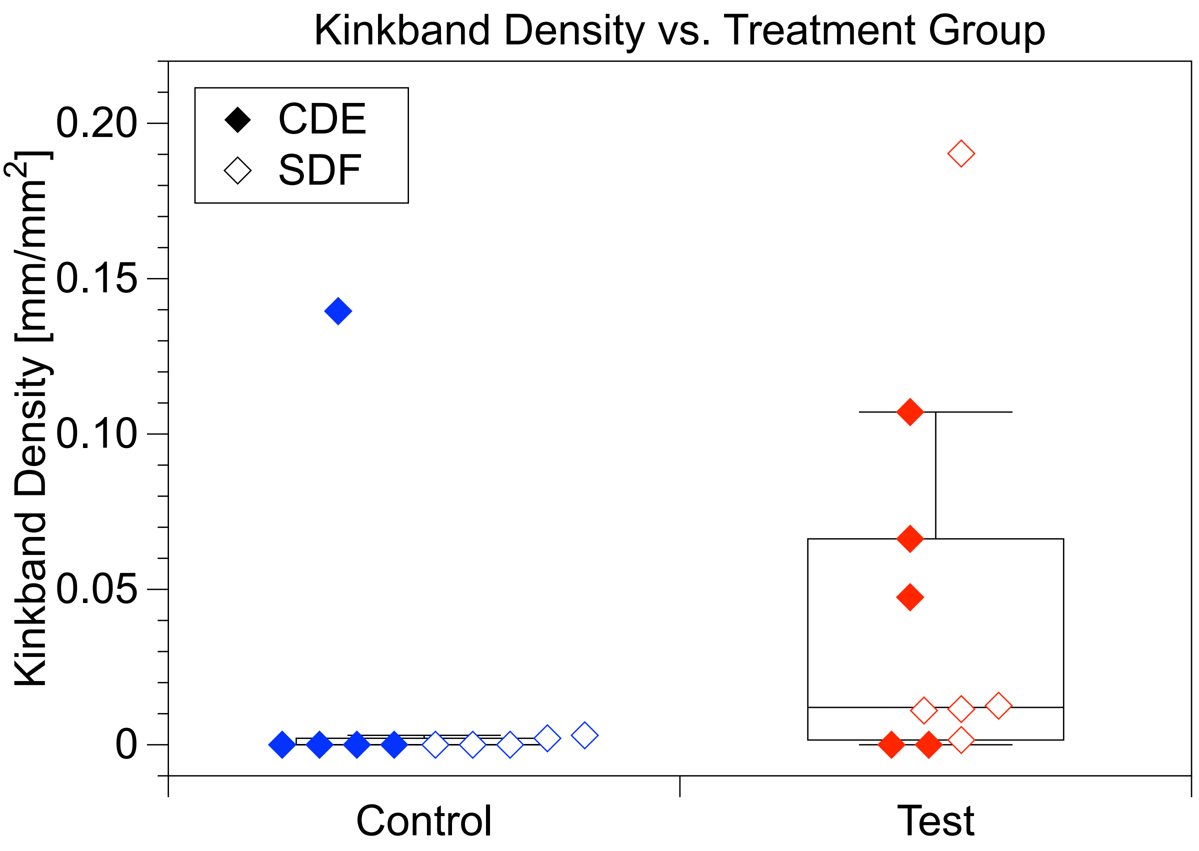

Figure 4.12: Kinkband density data measured through PLM images as the ratio of total kinkband length to tissue area, for cyclically buckled and control tendons (n=10 tendons per treatment). The mean kinkband density of the test group (44.8x10^{-3} ± 62.1x10^{-3} [mm/mm^2]) was significantly greater than that of the control group (14.5x10^{-3} ± 44.0x10^{-3} [mm/mm^2]). While 8/10 tendons in the test group had a non-zero kinkband density, only 3/10 tendons in the control showed this result.

4.4 Second Harmonic Generation Microscopy

4.4.1 Background

Second harmonic generation (SHG) microscopy is a non-linear optical technique. As collagen is one of the best biological producers of SHG signals, it has been utilized in SHG microscopy research. Aside from research, its potential as a clinical tool to aide in the diagnoses of diseases and cancers is a growing interest of the field[145–147].

The principles of SHG hinge on the optical non-linearity of a material. When a singular photon interacts with an electron of a non-linear material, the electron takes on the energy of the colliding photon, bringing it to a high-energy virtual state[148,149]. To exit this high-energy virtual state, the electron releases the energy as a single photon, having the energy and wavelength of the incident photon. However, when two photons of the same energy interact simultaneously with an electron of a non-linear material, the electron must take on twice the energy as it would with a single photon colliding, again raising it to a virtual state. To return to a ground state, the energy carried by the two incident photons must be released. The manor of the release of energy is irrelevant, so the electron releases it all as a singular photon[145,148]. This transmitted photon has double the energy, and therefore half the wavelength of the original photon[145,148]. The photon can be easily differentiated from the laser light by its second harmonic frequency.

The induction of a dipole moment is an intrinsic component of SHG signal production, as SHG signal is a measure of a material's ability to non-linearly respond to an applied electric field[150–152]. Therefore, materials with a high hyperpolarizability, such as those with a non-centrosymmetric structure, specifically on the second order, are the best emitters of SHG signal[148]. This makes collagenous tissues ideal for SHG microscopy. On a molecular level, the peptide bonds of the triple helical collagen molecule have a high hyperpolarizability[153]. For each bond or group of atoms in a collagen molecule, there is no similar feature directly opposing it to prevent the occurrence of a net dipole moment[26]. At a larger scale, a non-centrosymmetric structure is necessary for the same reason. When two photons of the second harmonic frequency are released from two separate infinitesimally spaced dipoles, having opposite directions, they destructively interfere, resulting in no net SHG signal production[148,152]. However, when two photons with frequency doubling come from infinitesimally spaced dipoles, having the same direction, they constructively interfere, resulting in the addition of signal[148,152]. In centrosymmetric structures, each dipole has a counter dipole[154], equally spaced from the centroid in the opposite direction, resulting in the absence of a net signal production. Although all collagenous molecules can produce a SHG signal, those structures having a directional dependency, such as the rod like fibrils of tendon, reap the benefits of SHG microscopy much more than quasi-centrosymmetric structures.

To induce and detect SHG signal from a sample using a typical polarization-in polarization-out (PIPO) setup, SHG microscopy requires a laser as the light source[155]. The pulsed laser fires photons at galvanometric scanning mirrors, reflecting the beam through a polarization state generator (PSG), which works with a half wave plate to rotate the polarization and polarize the light at various angles, while raster scanning the sample[155]. Before reaching the sample, the beam is focused using an air immersion objective lens[155]. As the beam passes through a thin coverslip and interacts with the sample, the emitted photons are collected by a collection objective lens[155]. The collected photons are filtered at various angles again, using a polarization state analyzer (PSA)[155]. The light then moves through an interference filter with a small bandwidth, centered at half of the incident light wavelength, to separate the photons having second harmonic frequency from the laser light[155]. The filtered light is finally measured by a single-photon-counting photomultiplier detector, obtaining the detected SHG intensity values[155].

After intensity values from the PIPO scan are obtained, different parameters of interest may be investigated. The second-order non-linear susceptibility of a material ($\chi^{(2)}$) to an applied electric field, in the general case, can be described by a 27 component, third-order tensor[148,156]. To simplify the tensor, the number of terms can be reduced using some common assumptions, specific to collagen. It is typical to approximate collagen fibrils as being a straight rod[157]. Additionally, fibrils may be assumed to have cylindrical symmetry, equivalent to hexagonal symmetry for a tensor of rank 3[157]. Applying these assumptions, the resulting SHG intensity (I_{SHG}) equation (equation 4.1)[20] can be used to fit PIPO-SHG data as a function of laser linear polarization angle (θ') and analyzer angle (φ'), for each pixel:

$$I_{SHG} \, \alpha \, | \, \rho \cos \varphi' \cos^2 \theta' + \sin \varphi' \sin 2\theta' + \cos \varphi' \sin^2 \theta' + 2\kappa \cos \varphi' \sin \theta' |^2 \qquad (4.1)$$

To better conceptualize the parameters in equation 4.1, all parameters will be described with respect to the Tokarz laboratory frame of reference, seen in Figure 4.13. The angle α describes the tilt of the fibril from the Z-X plane, and the angle δ, is the angle between the fibril projection onto the focal plane and the Z axis[155]. The angles θ and φ are defined so that $\theta' = \theta - \delta$ and $\varphi' = \varphi - \delta$[155]. The most common fit parameter of equation 4.1 is ρ. Referred to as the anisotropy parameter, ρ, is a measure related to the structural order of collagenous tissue[20]. It is defined as $\chi^{(2)}_{ZZZ}/\chi^{(2)}_{ZXX}$, which is comprised of two terms. The first, indicative of structural order of fibrils, is a function of the sine of α[20]. The second term, describing structural order within fibrils, is a function of the product of the cosine of α and ρ_f, where ρ_f is the fibril frame disorder parameter, affected by the angular arrangement of peptides within a collagen molecule[20]. The last parameter of equation 4.1 is κ, defined as $\chi^{(2)}_{XYZ}/\chi^{(2)}_{ZXX}$, which is the product of κ_f and the sine of α, where κ_f is the fibril frame chirality parameter, indicating the resultant chirality sign within each pixel[20].

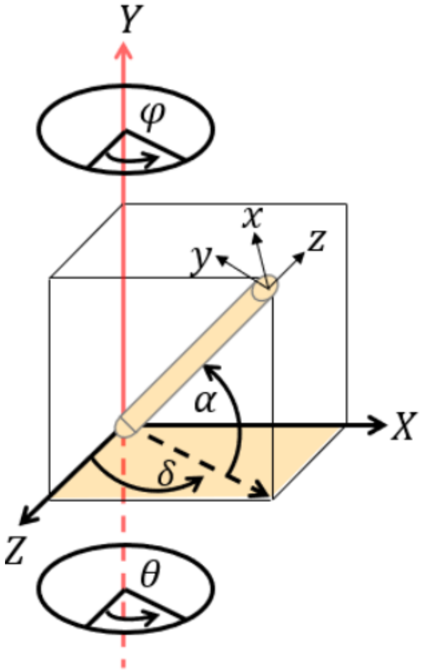

Figure 4.13: This is a diagram of the coordinate system used by the Tokarz laboratory, when describing the orientation of a collagen fibril (the yellow cylinder) laying in the Z-X focal plane (yellow shaded quadrilateral). The positive Y direction signifies the direction of light propagation from the laser. Capital X-Y-Z are the laboratory reference frame, while lower case x-y-z are the fibril reference frame, with the fibril longitudinally oriented along the z-axis. (figure modified from Tokarz et al., 2019)[155]

In tendon research, SHG microscopy has become a valuable technique for assessing structure, before and after mechanical testing, specifically of individual fibrils. As mentioned, the main parameter indicative of structural disorder is ρ. For individual fibrils, ρ values differing from normative levels suggests a structural change within the single fibril imaged[20]. When imaging tendon cross-sections, containing numerous fibrils and fibres, irregular ρ values may be caused by various factors. It becomes unclear if structural changes occur due to multiple fibrils crossing and causing interference, or if a specific fibril has crossed over itself in a kinking manor. This often leads to the use of additional imaging techniques to supplement SHG microscopy[19]. Recently, the use of SHG microscopy in collaboration with fluorescence microscopy on CHP-stained samples helped researchers to discern whether changes in structural order were occurring on a molecular or fibril level[106]. As the addition of imaging techniques provides further insight to the structure of a sample, it is important that techniques selected to support SHG microscopy help reduce uncertainties in results.

4.4.2 Hypotheses and Rationale

The objective of this section was to provide a measure of structural order in cyclically buckled and control tendons, of both tendon types, at target locations. The goal was to quantitatively measure structural order through the parameter ρ and qualitatively through the other parameters of equation 4.1.

Hypothesis (vi): Locations of a tissue section appearing healthy through PLM imaging will have the same ρ values, regardless of whether they were cyclically buckled or not.

Rationale: This would indicate that although cyclic buckling may disrupt tissue order globally, it does not affect the entirety of a buckled tendon's cross-sectional area at a given section.

Hypothesis (vii): Locations containing a kinkband, or some other abnormality, will have greater ρ values than healthy appearing locations.

Hypothesis (viii): If hypothesis vii is true, the kinkbanded or other abnormal regions will have greater ρ values when present in tendons belonging to the test group, compared to the control.

Rationale: A kinkband is a form of structural damage, meaning it should be accompanied by an increase in disorder. Additionally, tendons belonging to the test group will have undergone excess loading relative to the control, exaggerating the degree of structural disorder.

Hypothesis (ix): The ρ values of healthy regions, specifically in the control samples, will be greater in SDF than CDE tendons.

Rationale: In the literature, only one study is known to have measured mean ρ values of both positional and energy-storing tendons in the same experiment[18], and no studies are known to have reported a significant difference between the two. Due to the lack of research supporting the insignificant difference in ρ values between tendon types, it is possible that a difference exists. The parameter ρ is a measure of both molecular and fibril order. While the literature does not suggest differences in the collagen molecules of each tendon type, there are known structural differences at the fibril level. Specifically, crimp has been reported to repeat over a shorter distance in SDF than CDE tendons[30]. When tissue within a pixel is well aligned with a low α value, it has a ρ value near 1. As it becomes out of plane and is not all oriented in the same direction, ρ increases. The shorter crimp period of SDF tendons may cause neighbouring fibrils to reside at slightly different angles, who's slight differences are larger than those of CDE tendons, resulting in greater mean ρ values in healthy SDF tendons.

Hypothesis (x): Kinkbands observed through PLM will either have very high ρ values along the kink, or an absence of signal. The absence of signal will result from the denaturation of molecules and these denatured kinkbands should occur with the same frequency as in the fluorescence images.

Rationale: A kinked fibril typically results in the fibril crossing over itself, as shown through scanning electron microscopy[95]. Further, the crossing of fibrils has previously demonstrated an increase in ρ value through SHG microscopy[155].

Hypothesis (xi): The ρ values associated with kinkbands in SDF tendons will not increase as much as the ρ values associated with those of CDE tendons, relative to normal.

Rationale: The superior fatigue resistance and ductility of the SDF tendon will lead to a less brittle kinking of fibrils, where a brittle kinking would cause extreme localized disorder[42,144].

Hypothesis (xii): The structural order of tissue immediately adjacent to kinkbands will be slightly more disordered than normal but tissue further from the kinkband will have typical structural order[30,95].

Rationale: It appears in scanning electron microscopy images that kinkbands have a small kink width and the tissue gradually returns to normal on either side of the kinkband[95].

Hypothesis (xiii): The tissue along and on either side of a kinkband will often lay at different angles.

Rationale: In the scanning electron microscopy images of kinkbands in the literature, the kinking of fibrils does not appear to be planar, but rather three-dimensional[30,95].

4.4.3 Methodology

Experimental

Following cyclic buckling (Chapter 3.4), cryo-sectioning (Chapter 4.1), and PLM imaging (Chapter 4.3.4), 5 μm thick samples[158] were imaged using PIPO-SHG microscopy. For each sample, PLM maps were used to locate one region that appeared to be healthy, and when present, one that appeared to contain a kinkband, or some other abnormality (Figure 4.14). At each location, 9 PIPO scans were taken, shifting the scan location to obtain an overlap of roughly 10% between scans. After primary analysis, it was determined that some previously suspected kinkbands no longer fit the criteria, so additional kinkbands were located and a single PIPO scan was taken at each kinkband location. The microscope used for scanning has been previously described[159–161], but the specifications used for the work done for this thesis will be discussed here. The laser used in the microscope was a femtosecond duration pulsed laser. Pulses had a wavelength of 1030 nm, repetition rate of 5 MHz and duration of 300 fs. Using a pair of galvanometric scan mirrors, the laser beam was raster scanned over the scan area, with a pixel dwell time of either 6 or 12 µs. The scan area was 98x98 µm, and the corresponding image produced was 100x100 pixels. An air immersion objective lens with a numerical aperture of 0.8 was used to focus the beam to a lateral spot size of approximately 785 nm. To separate the light of second harmonic frequency from the laser light, an interference filter of width 10 nm, centered at 515 nm was used. A PSG consisting of a stationary linear polarizer and half wave plate were located on a motorized stage. On another motorized stage was a PSA, consisting of a polarizing filter. To produce each PIPO-SHG image, a 64 SHG image stack was obtained, using all combinations of 8 polarizer and 8 analyzer angles, rotating each 22.5° between 0 and 180°. One final image was taken at the end in the same location as the original, to ensure no photobleaching, burning, or movement of the sample occurred.

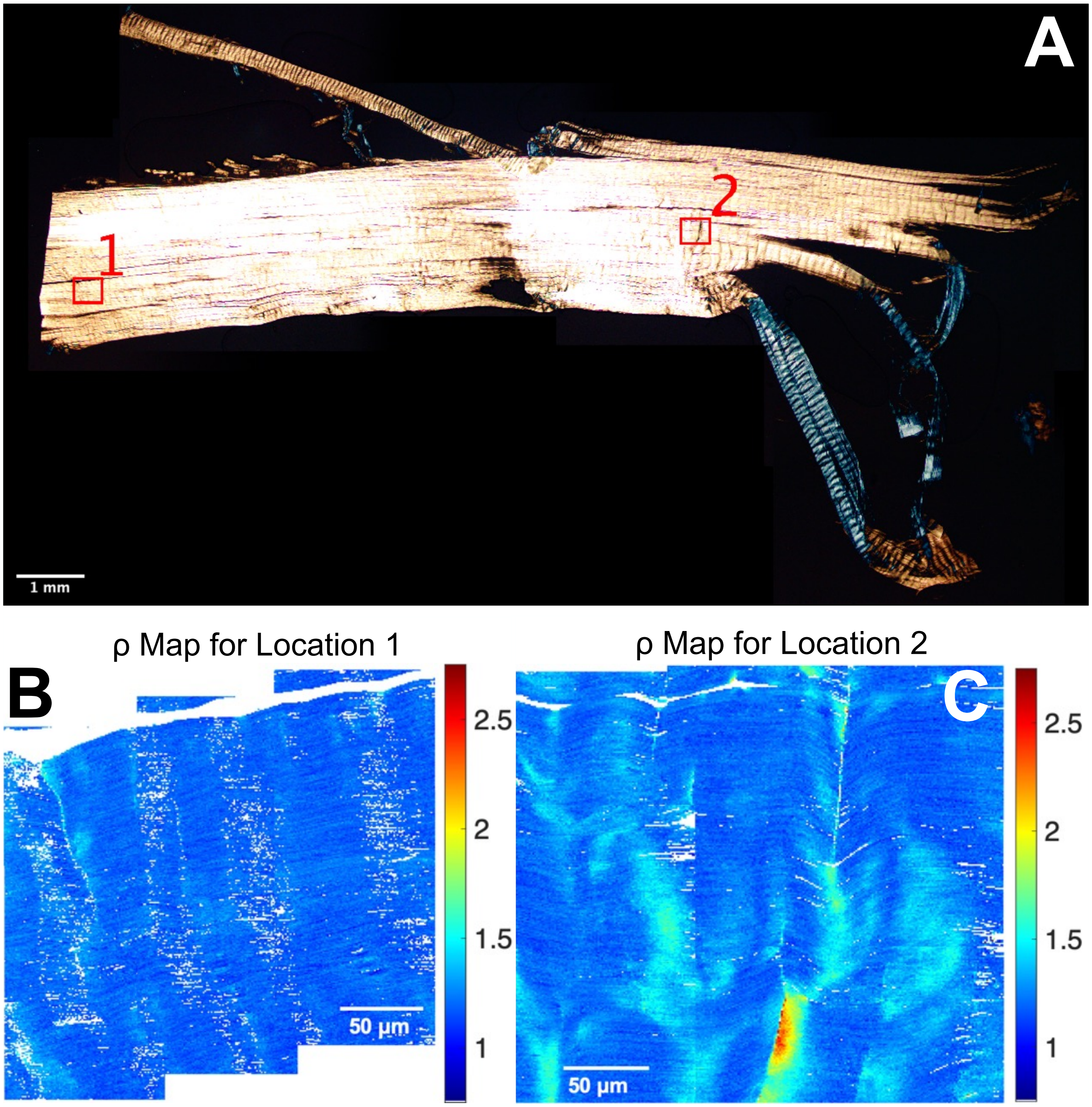

Figure 4.14: (A) The annotated PLM image of an SDF test tendon, with the two SHG scan locations located in red boxes labelled ‘1’ and ‘2’, respectively. (B) The ρ map for location 1, identified as a healthy region on the PLM image. (C) The ρ map for location 2, identified as an abnormal region on the PLM image. Both ρ maps are made up of 9 stitched PIPO scans.

Once all 9 scans at a location were obtained, each pixel was fit to equation 4.1, using a custom MATLAB (R2023a) program for fitting and visualizing SHG-PIPO scans. Scans were assumed cylindrical rods and fit using C_6 hexagonal symmetry[149,156,162,163]. A requirement was set for pixels to have a minimum intensity of 50 counts and goodness of fit parameter, $R^2 \geq 0.8$, to be displayed in images and considered in any analyses. After all scans at a location were fit, the ρ parameter-fit images of each were visualised and manually stitched together in Adobe Photoshop, to create a map containing the ρ value of each pixel at a location (Figure 4.14). These maps were used to better conceptualize the collagenous structure observed on the PLM images, and were also used in the data analysis, described in Chapter 4.4.3.

Data Analysis

Quantitative and qualitative analyses were both conducted on the SHG-PIPO images. The data were quantitatively analyzed using the ρ values of each pixel. Two quantitative analytical approaches were taken. Approach 1 looked at the entirety of each location, categorizing it as either healthy or abnormal, and then looking at the 10% and 1% of pixels with the largest ρ values, like the fluorescence analysis. Approach 2 looked at specific features within each location, selecting smaller regions of pixels representing healthy, kinkbanded, and disordered tissue. The additional kinkbands scanned after primary analysis, mentioned in the 'experimental' section of chapter 4.4.3, were only used for approach 2, as their total number of pixels was much less than the other locations.

For approach 1, the ρ value of all pixels in a location were concatenated and placed in ascending order, ensuring any overlapping pixels were only counted once. Any pixels having a ρ value not within the range of 0 to 5 were deemed outliers and excluded[155]. Of the remaining pixels, the 10% with the largest ρ values (considered to be the most disordered) were extracted and the mean average was calculated. Using the corresponding PLM image, each location was classified as either healthy or abnormal and all locations were categorized by 3 factors: (a) treatment (test/control), (b) tendon type (CDE/SDF), and (c) condition (healthy/abnormal). This process was then repeated, using the 1% of pixels with the largest ρ values.

For approach 2, three feature types (healthy, disordered, kinkbanded) were investigated. At each location, up to four 150–200-pixel regions per feature type were isolated and their ρ value profiles were extracted. Excluding all pixels having a ρ value outside of the 0 to 5 range, the mean ρ value of each select region was computed. It was important to ensure that two select regions were not isolated from the same feature (i.e. two sections of a continuous kinkband), as this would place a greater weight on that specific feature. Again, all select regions were categorized by 3 factors: (a) treatment (test/control), (b) tendon type (CDE/SDF), and (c) condition (healthy/disordered/kinkbanded).

Healthy features, as seen in Figure 4.15**,** were identified as those visually appearing to have a uniform ρ value that was consistent with other samples, supported by the region in the corresponding PLM image appearing typical.

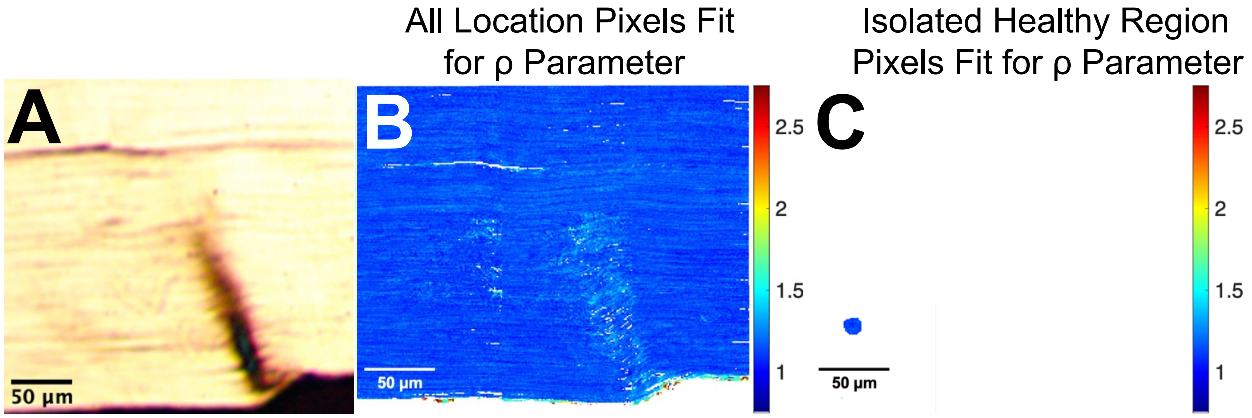

Figure 4.15: The tendon displayed in this figure is a CDE control tendon. (A) The PLM image, magnified at one of the SHG scan locations. (B) The corresponding 9 SHG scans, fit for the parameter ρ and stitched together to create a map. (C) The same SHG map as panel (C), but only showing the isolated 179-pixel region in the bottom left corner of the SHG map. This region demonstrates the typical presentation of the healthy characterization.

Features labelled disordered, as seen in Figure 4.16, were identified as regions visually appearing to have pixels with the highest ρ values at a location.

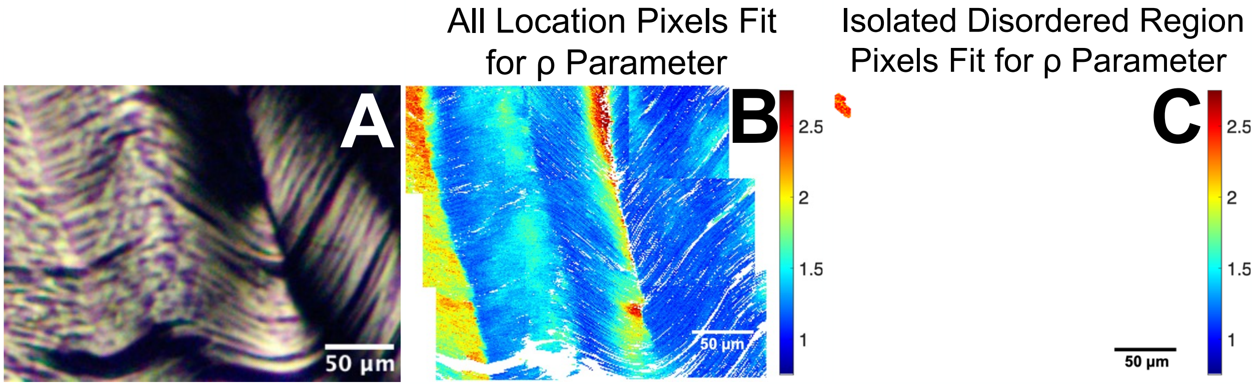

Figure 4.16: The tendon displayed in this figure is a CDE test tendon. (A) The PLM image, magnified at one of the SHG scan locations. (B) The corresponding 9 SHG scans fit for the parameter ρ and stitched together, to create a map. (C) The same SHG map as panel (B), but only showing the isolated 184-pixel region in the top left corner of the SHG map. This demonstrates how a region characterized as disordered may present itself.

Kinkbands were features adhering to the kinkband criteria, outlined in Chapter 4.3.2. All kinkbands were first identified using PLM images. Once confirmed, the kinkband was outlined on the ρ parameter image (Figure 4.17), using a maximum width of 5 pixels. Although this meant the kinkband width was wider than that defined through PLM imaging, many pixels along the kinkband did not fit, so this technique was used to best describe the structural order around a kinkband.

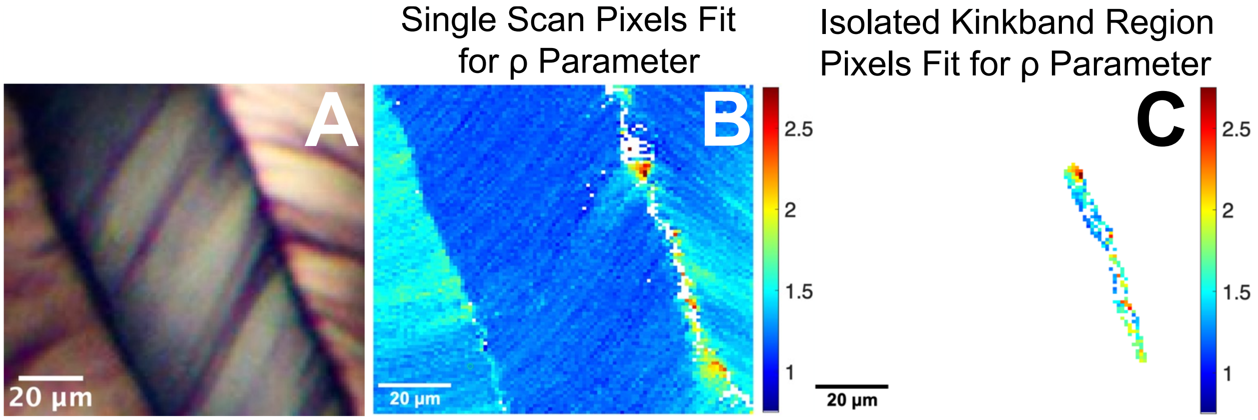

Figure 4.17: The tendon displayed in this figure is a CDE test tendon. (A) The PLM image, magnified at one of the single PIPO scan locations. The image contains only one kinkband, located on the right. The feature appearing as a potential kinkband, on the left, failed to meet the kinkband inclusion criteria. (B) The corresponding PIPO image, with pixels fit for the parameter ρ, showing the kinkband located on the right has many unfit pixels. (C) The same PIPO scan as in panel (B) but isolating a 170-pixel region of the kinkband, containing only pixels related to the kinkband.

For qualitative analysis of the data, several fit parameters were visualized, such as δ, ρ, κ and the intensity image. This analysis was used as a supporting tool when interpreting the quantitative results of approach 2, specifically regarding the formation and properties of kinkbands.

Statistical Analysis

Statistical analysis was conducted using JMP (Version 17.1.0, SAS Institute, USA). For approach 1, the data were first rank transformed. A three-way ANOVA was then performed on the data, with treatment, tendon type, and condition as the factors. For approach 2, the data was analysed differently. Since there were not enough kinkbands in the control tendons to perform statistical testing, for either tendon type, the data was split by treatment and each treatment was analyzed independently. For the control tendons, the data were first rank transformed. A two-way ANOVA was then conducted, with tendon type and condition as the factors. In the case of the control, condition did not contain kinkband as a group and therefore only contained the two groups of healthy and disordered. For the test tendons, the process was repeated. The data were rank transformed, and a two-way ANOVA was performed, with tendon type and condition as the factors. To investigate the factor of treatment, a series of Kruskal-Wallis tests were conducted on each of the following groups: disordered CDE, disordered SDF, healthy CDE and healthy SDF. In each statistical test the treatment groups of test and control were compared.

4.4.4 Results

The statistical analysis conducted using approaches 1a and 1b resulted in the same factors showing significance. For approach 1a, the mean average of the 10% of pixels with the highest ρ values at each location showed those of SDF to be significantly higher than CDE tendons ($p = 0.0144$) and those of abnormal locations to be significantly higher than healthy ($p = 0.0019$). For approach 1b, using the 1% of pixels with the highest ρ values at each location, the SDF tendons were significantly higher than CDE ($p = 0.0494$) and abnormal significantly higher than healthy ($p = 0.0006$). Interestingly, neither treatment ($p = 0.0984$ for 10% of pixels and $p = 0.1484$ for 1% of pixels), nor any of the interaction terms proved to have a significant effect on the ρ values. Figure 4.18 shows a comparison of the ρ values outlined in Tables 4.1, and 4.2, for each of the significant factors in approaches 1a and 1b.

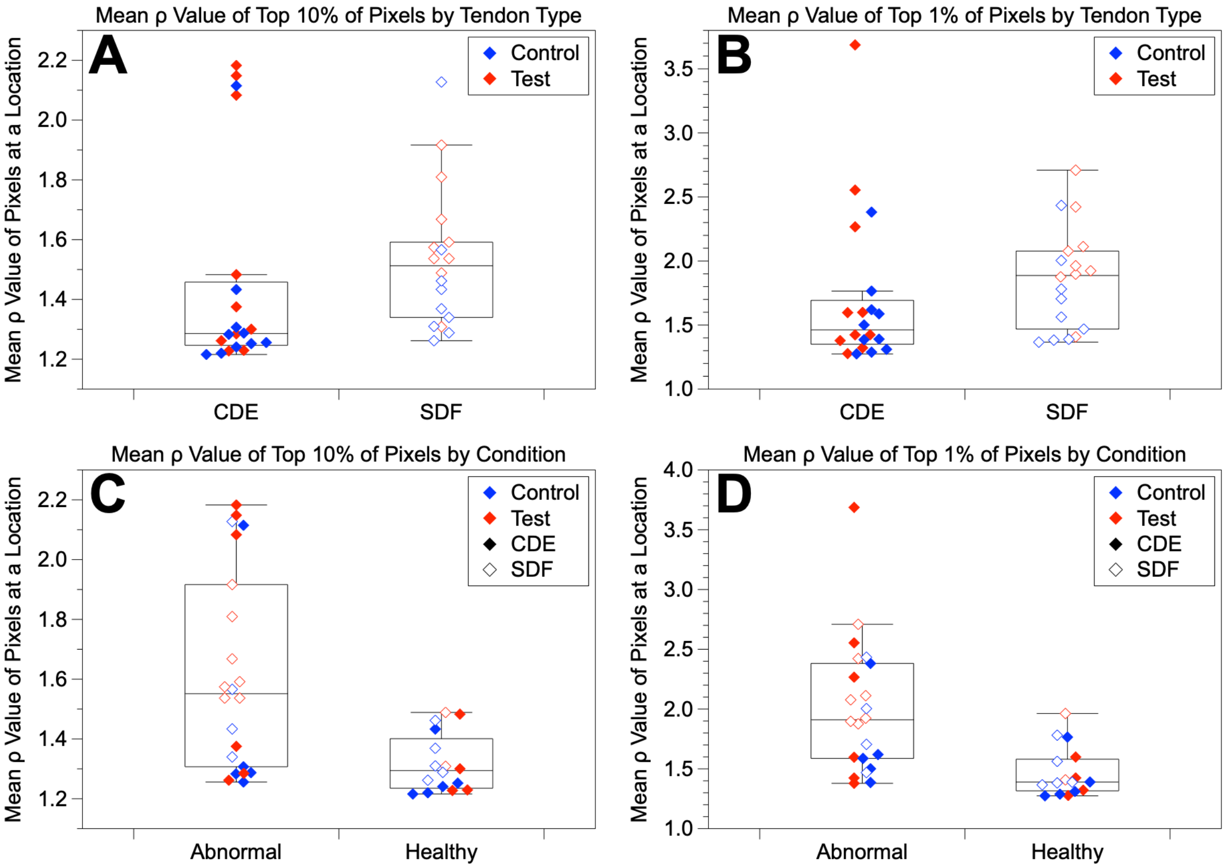

Figure 4.18: In plots (A) and (B), the mean ρ values at each scan location are compared between the CDE and SDF tendons for, (A) the 10% of pixels and (B) the 1% of pixels with the greatest ρ values. In both plots, the ρ values associated with SDF tendons were generally higher. In the bottom two plots, the mean ρ values at each scan location are compared between those of regions categorized as abnormal and healthy for, (C) the 10% of pixels and (D) the 1% of pixels with the greatest ρ values. Plot (C) and (D) both clearly show the ρ value of abnormal regions to be higher.

Table 4.1: Mean ρ Values and Associated *p*-value for Approach 1a

	Mean ρ value	***p*-value**
CDE	1.46 ± 0.35 [n=20]	$p = 0.0144$
SDF	1.53 ± 0.23 [n=18]	
Healthy	1.32 ± 0.10 [n=16]	$p = 0.0019$
Abnormal	1.62 ± 0.33 [n=22]	

Table 4.2: Mean ρ Values and Associated *p*-value for Approach 1b

	Mean ρ value	***p*-value**
CDE	1.70 ± 0.60 [n=20]	$p = 0.0494$
SDF	1.86 ± 0.40 [n=18]	
Healthy	1.47 ± 0.21 [n=16]	$p = 0.0006$
Abnormal	2.00 ± 0.56 [n=22]	

Approach 2, looking at specific regions of interest, proved to be a much better analytical method. This was essentially a more precise version of approach 1, as the select regions of interest were much smaller and consequently only containing pixels conforming to the desired feature. In this approach, there were many significant factors and interaction terms. For the two-way ANOVA conducted on the control data, all factors (tendon type and condition) and interactions (interaction between tendon type and condition) were found to be very significant ($p < 0.0001$). A similar result was found for the two-way ANOVA run using the test data. Here, a significant difference considering the factor of tendon type ($p = 0.0046$) and the interaction between tendon type and condition ($p = 0.0063$) was observed, while a very significant difference was found considering the factor of condition ($p < 0.0001$) alone. The plots shown in Figure 4.19 help to better conceptualize the differences observed between the significant results of the two-way ANOVA's.

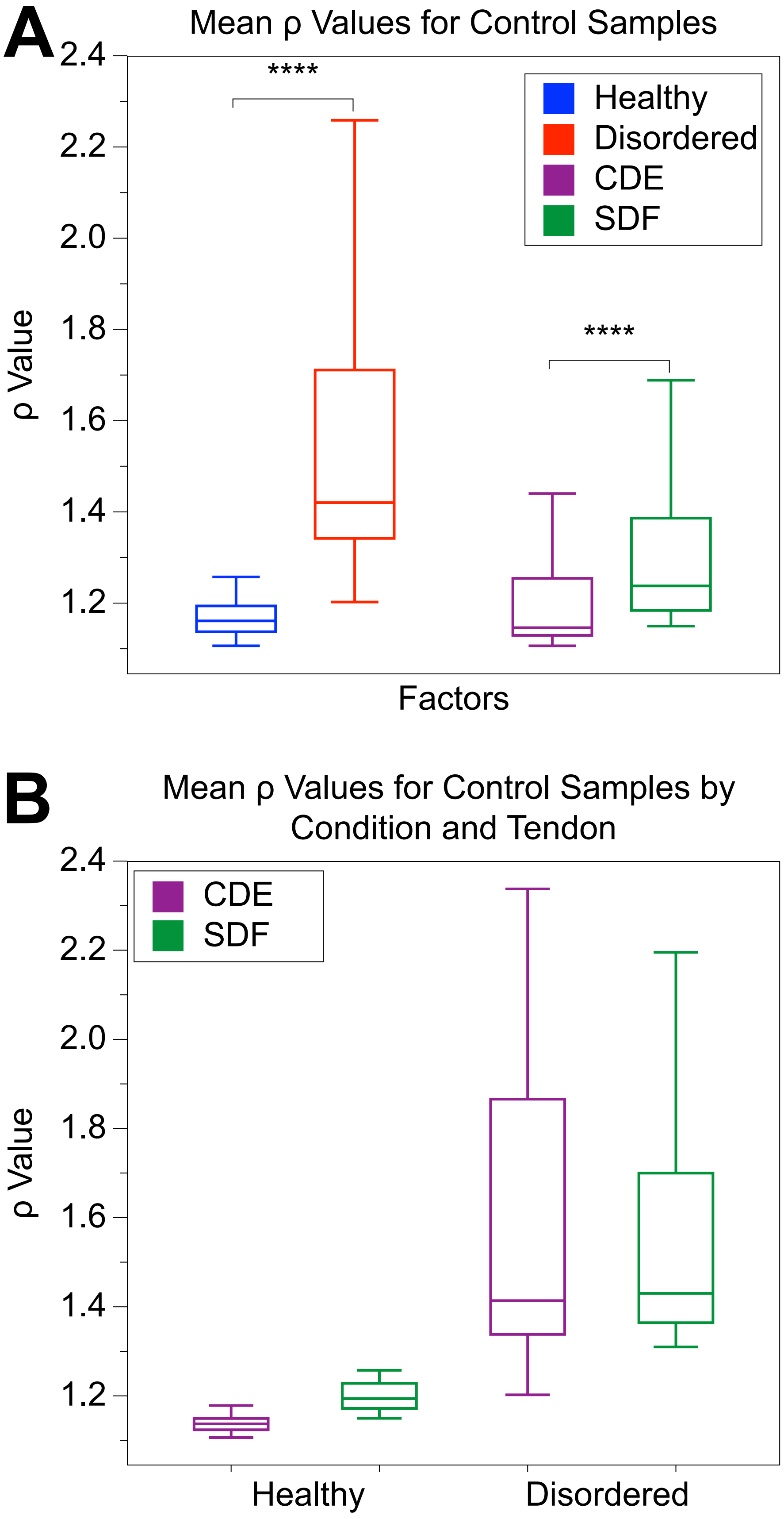
A
Mean ρ Values for Control Samples
ρ Value
2.4
2.2
2.0
1.8
1.6
1.4
1.2
****
****
Healthy
Disordered
CDE
SDF
Factors
B
Mean ρ Values for Control Samples by Condition and Tendon
ρ Value
2.4
2.2
2.0
1.8
1.6
1.4
1.2
CDE
SDF
Healthy
Disordered

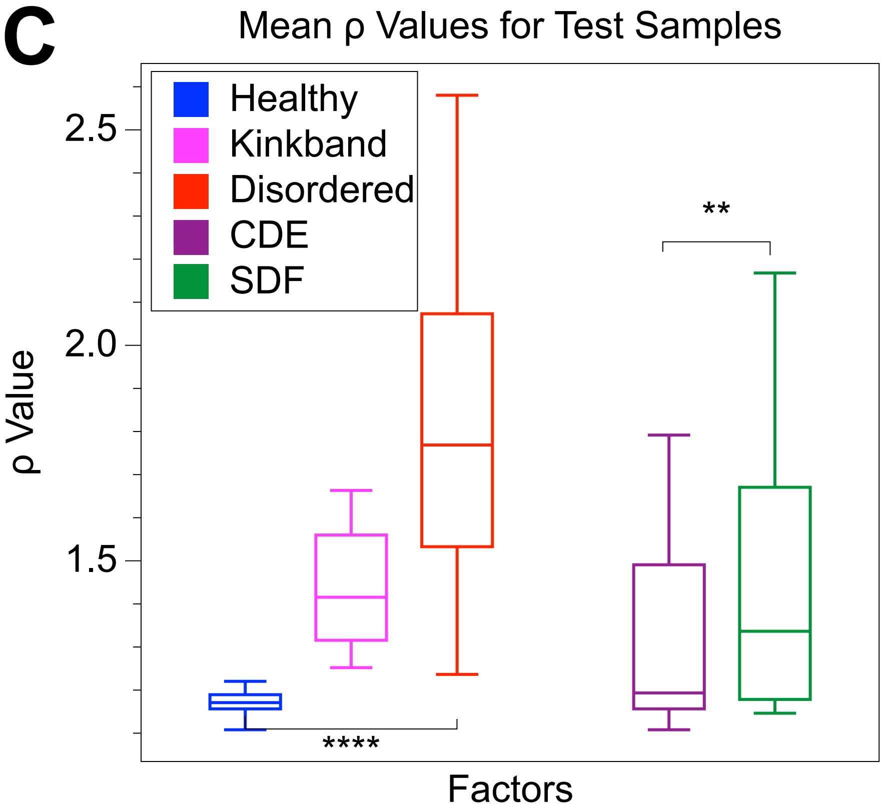
C
Mean ρ Values for Test Samples
🟦 Healthy
🟪 Kinkband
🟥 Disordered
🟪 CDE
🟩 SDF
**
****
2.5
2.0
1.5
ρ Value
Factors

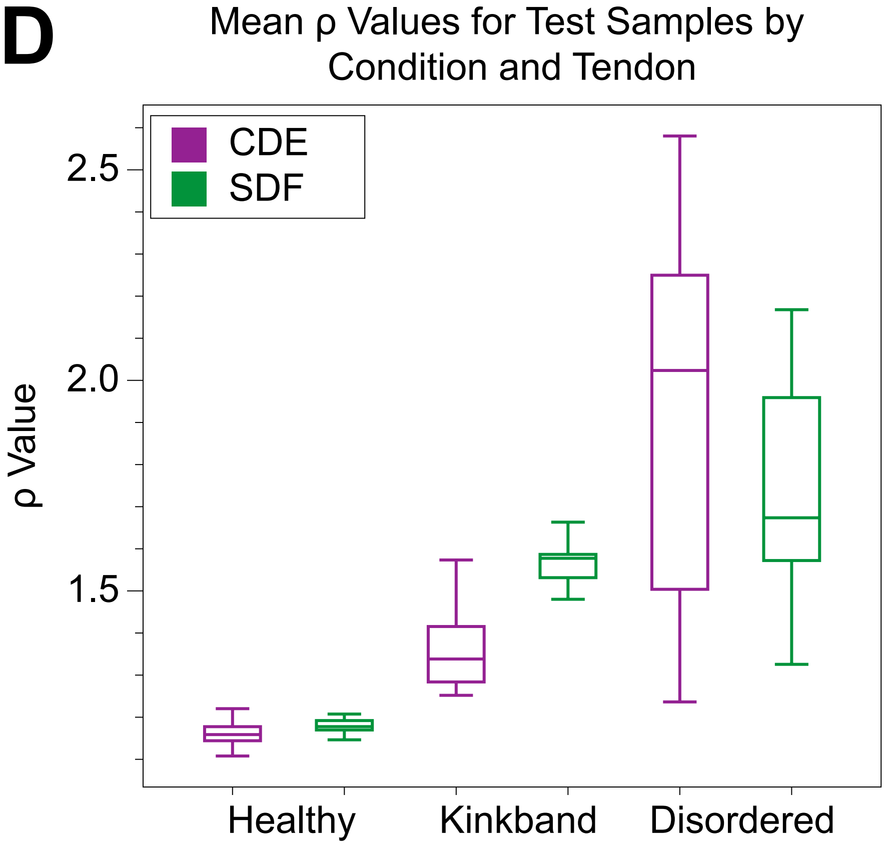
D
Mean ρ Values for Test Samples by Condition and Tendon
🟪 CDE
🟩 SDF
2.5
2.0
1.5
ρ Value
Healthy
Kinkband
Disordered

Figure 4.19: (A) A plot of the mean ρ values of each specific region in the control tendons, considering only the groups within condition and tendon type and not considering interaction terms (i.e. in the CDE group, all regions of CDE tendons, regardless of their condition are considered). (B) A plot of the mean ρ values of each specific region in the controls, considering all combinations of interaction terms. While it is evident that ρ values of SDF tendons are greater than CDE tendons in the healthy regions of both, in disordered regions, the SDF and CDE tendons appear similar, with the SDF tendons having a larger range. (C) The same plot as in (A) except considering only test tendons rather than control. This plot has the additional group of kinkband, which has differing ρ values from those of healthy and disordered. (D) A plot of the mean ρ values of each specific region in the test, considering all combinations of interaction terms. Tendon type does not appear to affect the general order of ρ values between conditions (healthy, kinkband, disorder) though within each condition there are differences. Healthy SDF is again greater than healthy CDE tendons. SDF kinkbanded regions appear to have larger ρ values (1.57 ± 0.07, [n=5]), than CDE kinkbanded regions (1.36 ± 0.11 [n=10]). Disordered CDE tendons show greater ρ values than disordered SDF tendons.
* $p < 0.05$, ** $p < 0.01$, *** $p < 0.001$, **** $p < 0.001$

While the results observed when looking at the test and control treatment methods separately are interesting and provide value, one of the main purposes of this thesis was to assess the response of tendons to cyclic buckling. To do so, four Kruskal-Wallis tests were conducted, each of which demonstrated a different result. The ρ value and associated level of significance for all Kruskal-Wallis tests are shown in Figure 4.20 and Table 4.3. When looking at healthy regions of SDF tendons, the mean ρ value was not significantly different ($p = 0.1424$) between treatments, but in the healthy CDE tendons, the difference was very significant ($p < 0.0001$). For the mean ρ value of disordered CDE tendons, a marginally significant difference ($p = 0.0583$) was observed among treatment methods, while in disordered SDF tendons, a significant difference ($p = 0.0102$) was observed.

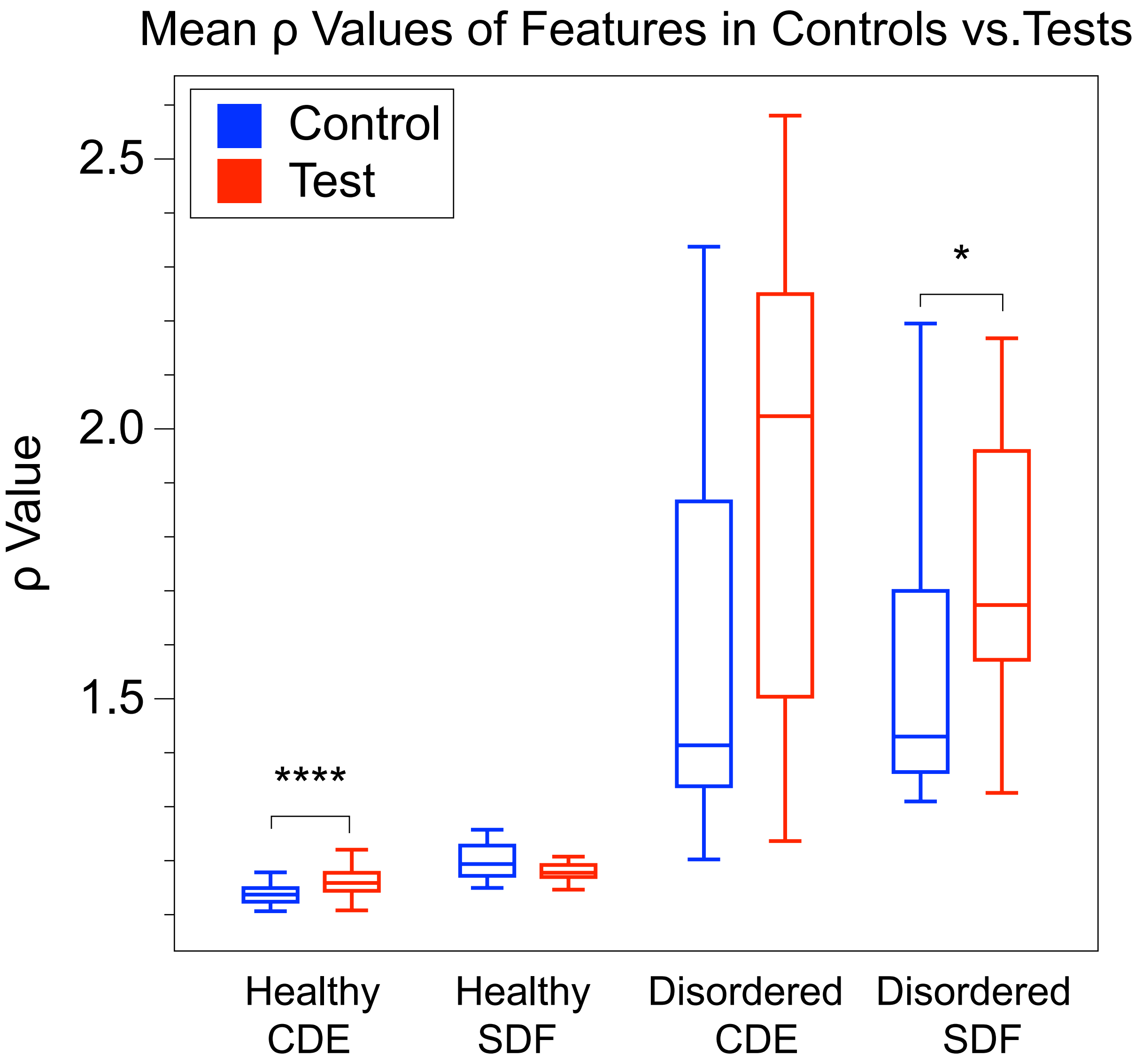

Figure 4.20: A comparison of the mean ρ values between test and control tendons considering all combinations of condition and tendon type. The most significant result shown is that the healthy regions of CDE tendons have greater ρ values in buckled tendons than in the controls.

* $p < 0.05$, ** $p < 0.01$, *** $p < 0.001$, **** $p < 0.001$

Table 4.3: Mean ρ Values and Associated p-values for Approach 2 Treatment Interactions

	Test Mean ρ value	**Control Mean ρ value**	***p*-value**
Healthy CDE	1.16 ± 0.02 [n=40]	1.14 ± 0.02 [n=40]	$p < 0.0001$
Healthy SDF	1.19 ± 0.03 [n=36]	1.21 ± 0.05 [n=40]	$p = 0.1424$
Disordered CDE	1.89 ± 0.46 [n=21]	1.61 ± 0.40 [n=17]	$p = 0.0583$
Disordered SDF	1.75 ± 0.24 [n=33]	1.58 ± 0.31 [n=24]	$p = 0.0102$

Aside from the quantitative analysis, a qualitative analysis yielded some expected and unexpected results, specifically regarding the observed kinkbands. First, when considering the three-dimensional effect of kinkbanding, the parameters κ, ρ and δ were compared to the intensity image. Assessing the four images together led to two results. The first of these results was pertaining to the kinkband on the left of each image in Figure 4.21. The intensity and δ images showed a very sharp change in fibril direction along the kink. The resulting κ and ρ images demonstrate, for this very sharp directional change, either side of the kinkband remains more or less in the same plane and having relatively similar structural order. This kinkband only exhibited structural changes directly along the axis of the kink, seen as an absence of fit pixels or pixels with an irregularly high ρ value. The second result can be observed through the kinkband on the right of each of the four images in Figure 4.21. For the δ and intensity images, the fibrils still appear kinked, but the kink does not look as sharp as that of the kinkband to the left. Additionally, the ρ and κ parameter fit images for the rightmost kinkband, display a clear difference in pixel colour on either side of the kinkband. The ρ image shows a relatively uniform level of structural order among pixels on the right of the rightmost kinkband. The κ parameter shows a gradient of values. The discrepancy between out of plane angle on the left and the right of the kinkband, measured through both ρ and κ, increases towards the right edge of the image, where the distance from the angled tissue to the image plane increases.

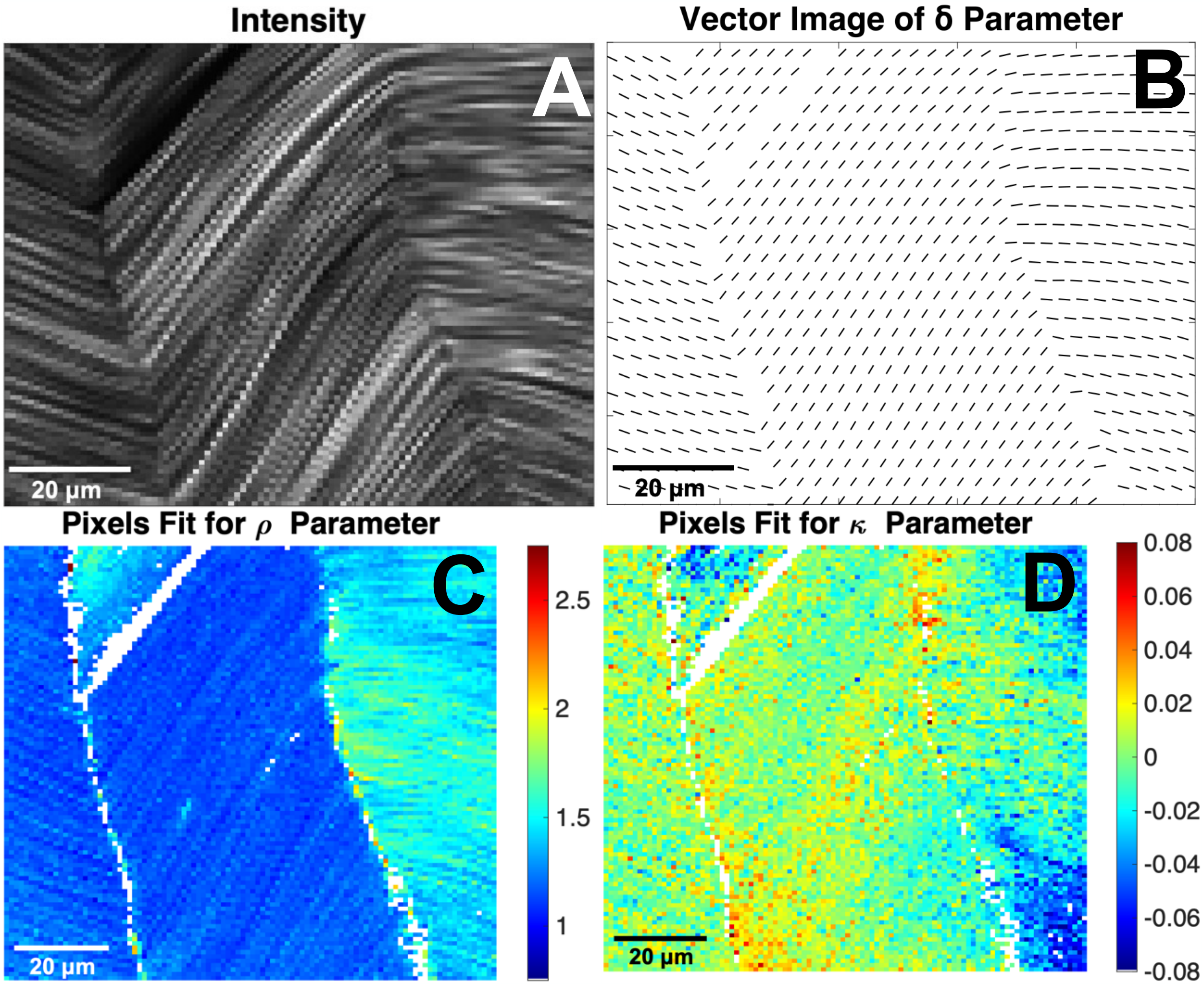

Figure 4.21: This figure shows an SHG-PIPO scan of a CDE test tendon containing two kinkbands. The scan is visualized in four different ways: (A) the intensity image, (B) the δ fit parameter vector image, indicating the direction of tissue as a resultant vector, (C) the ρ fit parameter, and (D) the κ fit parameter.

The second result of the qualitative analysis pertained to the unfit pixels observed along the center of most kinkbands. To determine the cause of a pixel's inability to fit, when located along a kinkband, the two requirements for a pixel to be displayed were revisited. The first requirement was that the pixel must have a minimum intensity of 50 counts. Upon investigation, the intensity of nearly all pixels met the minimum threshold, although it was slightly less than that of well fit pixels not located along a kinkband. The second requirement was for pixels to have a goodness of fit value, $R^2 \geq 0.8$. It was found that all unfit pixels failed to meet this requirement. To further investigate the unfit pixels the signal produced at all combinations of analyzer and polarizer angle was plotted. For well-fit pixels, each pixel's plot appeared to have a dog bone shape (Figure 4.22 A). This result was not observed in the unfit pixels. Instead, the pixels appeared elongated (Figure 4.22 B and C). Further, pixels having an R^2 value near 0.8 (Figure 4.22 B) tended to be less elongated than those far from fitting (Figure 4.22 C).

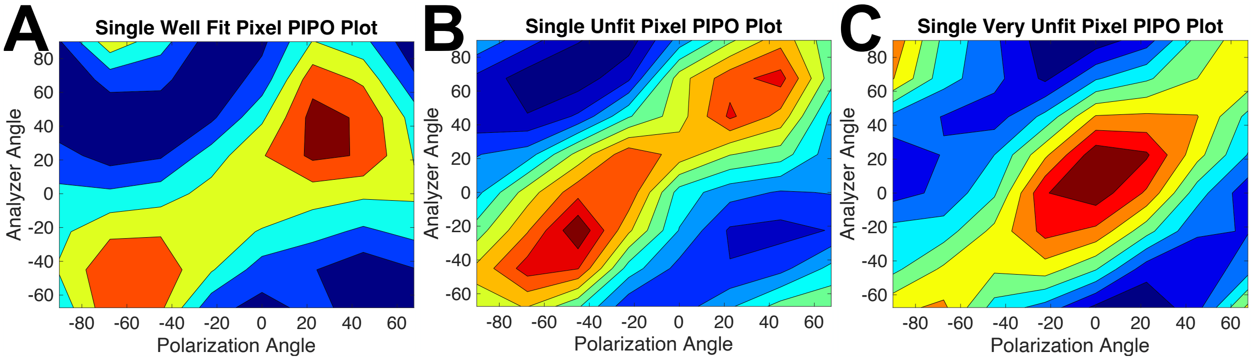

Figure 4.22: The following panel of pixel plots are taken from pixels present in Figure 4.21. The plots show the resulting SHG signal at each combination of analyzer (y-axis) and polarizer (x-axis) angle. (A) The very well fit pixel, located in between the two kinkbands, had an intensity of 268 and was fit with $R^2 = 0.95$. (B) The pixel barely failing to meet the fit requirements, located along the leftmost kinkband, had an intensity of 218 and goodness of fit value $R^2 = 0.71$. (C) The very poorly fit pixel, also located along the leftmost kinkband, had an intensity of 173 and goodness of fit, $R^2 = 0.53$.

4.5 Discussion

The structural hierarchy of tendon is very complex and interrelated, making it much easier to understand and discuss the results of each imaging modality when considering them cohesively. Each microscopy technique served a purpose. Fluorescence microscopy gave insight on a purely molecular level. SHG microscopy assessed collagenous structure on both a molecular and nano scale, though there was an inability to differentiate between the two. PLM evaluated tendon structure on a micro scale, while providing a bridge to relate features between the three imaging techniques. Rather than discussing the results as sequentially introduced, the hypotheses were grouped into two major categories: (i) those relating to the entire cross-sectional structure, and (ii) those specifically pertaining to kinkbands.

4.5.1 Structure of Entire Cross-Sectional Area

Considering the entire tendon cross-section, several results were discovered. Starting at the molecular level, fluorescence microscopy showed that cyclic buckling of tendons caused a significant increase in molecular denaturation. Though denaturation may be achieved with greater ease when stretching past the yield point[104], this observation is the first instance of achieving denaturation exclusively through cyclic buckling. While it was clear the entire test tissue did not become denatured, shown by the mean tissue denaturation of 8.1%, the micrographs gave insight to the dispersion of denaturation. Rather than a uniform dispersion, denatured collagen appeared to be concentrated in local areas distributed throughout the region of maximum tendon buckling, which is where sections were taken from.

To further investigate the fluorescence results, two SHG microscopy results were consulted. In approach 1, the mean ρ value of locations appearing healthy through PLM were significantly lower than those appearing abnormal. Further, for approach 1a, looking at the top

10% of ρ values in the healthy regions of test (1.34 ± 0.12) and control (1.31 ± 0.09) tendons, a significant difference was not shown, supporting the notion that damage due to cyclic buckling was localized. If damage due to cyclic buckling was not localized but rather dispersed across the tendon, a difference would be expected in healthy appearing regions between test and control at a SHG location, which was a cumulation of multiple PIPO scans. The SHG microscopy approach 2 results, considering interaction terms, provided additional support to the idea that cyclic buckling causes localized, but not global damage. In approach 2, a significant difference was found between the ρ values of test (1.75 ± 0.24) and control (1.58 ± 0.31) for SDF tendons and a marginally significant difference was found between the ρ values of test (1.89 ± 0.46) and control (1.61 ± 0.40) for CDE tendons. While healthy regions did not appear different between test and control tendons, as seen in approach 1, damaged regions did, as seen in approach 2. This suggests that denaturation is not the only localized tendon damage resulting from cyclic buckling, but collagenous disorder is also localized.

Importantly, this result of localized damage was observed in both positional and energy-storing tendons, showing damage resulting from cyclic buckling can occur regardless of tendon type. With fluorescence microscopy there was not a significant difference observed between cyclically buckled CDE and SDF tendons. Considering approach 2 of SHG microscopy analysis, there was a significant difference observed in the interaction of condition and tendon type for the cyclically buckled tendons, with disordered regions of CDE tendons having greater ρ values than disordered regions of SDF tendons. The fact that the results differed between the two microscopies was very interesting and unexpected, for a couple reasons.

Firstly, positional, and energy-storing tendons possess differing structures and loading responses. Energy-storing tendons have superior fatigue resistance[42,144]. If treatment did not prove to be a significant factor in fluorescence microscopy, a difference would not be expected between tendon types. However, it would be expected that as damage, such as molecular unfolding, is incurred, it propagates more rapidly in CDE tendons.

Second, the SHG microscopy data comparing tendon types at disordered regions in the buckled group, although not statistically significant, showed a trend that the mean ρ value of CDE tendons (1.89 ± 0.46) was greater than that of SDF tendons (1.75 ± 0.24). This result was also observed in the control group but to a much lesser extent (CDE: 1.61 ± 0.40, SDF: 1.58 ± 0.31). Since healthy regions of SDF tendons had greater ρ values than healthy regions of CDE tendons, the much larger ρ values in disordered regions of CDE compared to SDF tendons, only in buckled but not control tendons, indicates the structural order of CDE tendons is more severely affected than that of SDF tendons, following buckling. While possibly true, this does not indicate that CDE tendons contain more regions of disorder than SDF tendons following buckling, but it does indicate that when buckling causes disorder, it occurs in CDE tendons to a greater extent. However, knowing there is not a significant difference in denaturation between tendon types indicates these changes are likely on the fibril level.

Another expected and very important result regarding structural differences between tendon types, was that the ρ values of healthy regions in CDE tendons were lower than healthy regions of SDF tendons. Prior to this thesis, a difference in ρ values between tendon types was not reported, making these works the first to report this result. The result found in this thesis was that a very significant difference was observed between CDE and SDF tendons, specifically looking at healthy regions of the control tendons, as these values were most indicative of typical structural order. A CDE tendon ρ value of 1.14 ± 0.02 and SDF tendon ρ value of 1.21 ± 0.05 was observed. To further support this difference, the ρ value of healthy regions in test CDE tendons (1.16 ± 0.02) and SDF tendons (1.19 ± 0.03) showed a similar result, with slightly different values. The large sample size [n=36-40 for each group] and region size (150-200-pixels) utilized in finding this result lend support to the validity of these results, while additional data would aide in confirming the numerical values displayed. Future work may also help uncover whether these results are specific to the CDE and SDF tendons, or if they are another, of the many structural differences observed between positional and energy-storing tendons.

4.5.2 Structure Relating to Kinkbands

Many of the hypotheses related to the structural effects of cyclic buckling were inspired by a paper by Herod et al.[95], relating to the formation of kinkbands. Throughout this thesis, kinkbands were identified on a microscale, but investigated at various hierarchical levels, starting with the collagen molecule itself.

When identifying kinkbands through PLM images on a microscale, using the kinkband inclusion criteria (Chapter 4.3.2), two important results were found. The first result was that a significantly greater kinkband density was observed in cyclically buckled tendons, compared to the controls. The second result was that tendon type did not have a significant impact on the presence of kinkbanding. The first result advocates for the 'CUE' model proposed by Herod et al.[95], as it suggests that fibril buckling does in fact progress into kinkband formation. The second result also supports this model, as an insignificant difference in kinkband presence between tendon types alludes to the idea that kinkbanding is not specific to positional tendons, and the 'CUE' model may also be applicable to energy-storing tendons, something that before this thesis had not previously been investigated.

Additionally, some PLM images displayed a tissue pattern previously observed by Schmidt et al.[164] in the patellar tendons of paediatric cadavers (mean age 9.2 years old). The patellar tendon undergoes in vivo buckling[110] and is a tendon commonly susceptible to tendinopathy in humans[77,110,111], making this result very relevant. To properly compare the PLM images of the pediatric and ovine tendons, it would be necessary to test the pediatric tendon PLM images against the kinkband inclusion criteria of Chapter 4.3.2. Without access to the raw data from this study, a visual comparison of these results may suffice. Similarities were observed between the PLM image of the patellar tendon and regions of the buckled ovine tendon, potentially in the early stages of kinkbanding, but not classifying as a confirmed kinkband using the kinkband inclusion criteria of this thesis. In Figure 4.23 (A), portions of the ovine tendon bent or kinked to various degrees are observed through PLM. The patellar tendon (Figure 4.23 (C)) displays a crimp pattern where the tissue bend appears slightly sharper than the crimp of CDE and SDF tendons, as seen within the blue rectangle of Figure 4.23 (A)[19,138,143]. The patellar tendon crimp pattern resembles a sequence of repeated scalene triangles, rather than that of isosceles triangles, used to describe the crimp of CDE and SDF tendons[19,138,143], indicating the crimp of the patellar tendon is not a symmetric wave like that of CDE and SDF tendons. A pattern similar to that of the patellar tendon of Figure 4.23 (C) is observed in the ovine CDE test tendon of Figure 4.23 (B), though the pattern is not as systematic, as this pattern is not the intrinsic crimp of CDE tendons. In Figure 4.23 (A), regions to the left of the feature labelled (B) show what appears to be the progressively sharper bending of tissue (Figure 4.23 (D)), and a kinkband confirmed using the kinkband inclusion criteria (Figure 4.23 (E)). This entertains the notion that the observed tissue structure, on the fibrous level of patellar tendons, may be a result of the in vivo buckling experienced through mundane activities. If cyclic buckling conducted in this thesis can alter the tendon structure to mimic the patellar tendon, it is possible that the patellar tendon's natural state is at an early stage of kinkband formation, resulting from the physiological quantity of buckling experienced. If the amount of in vivo buckling experienced by the patellar tendon became excessive, it is possible that this could lead to the formation of kinkbanding, following the same progression.

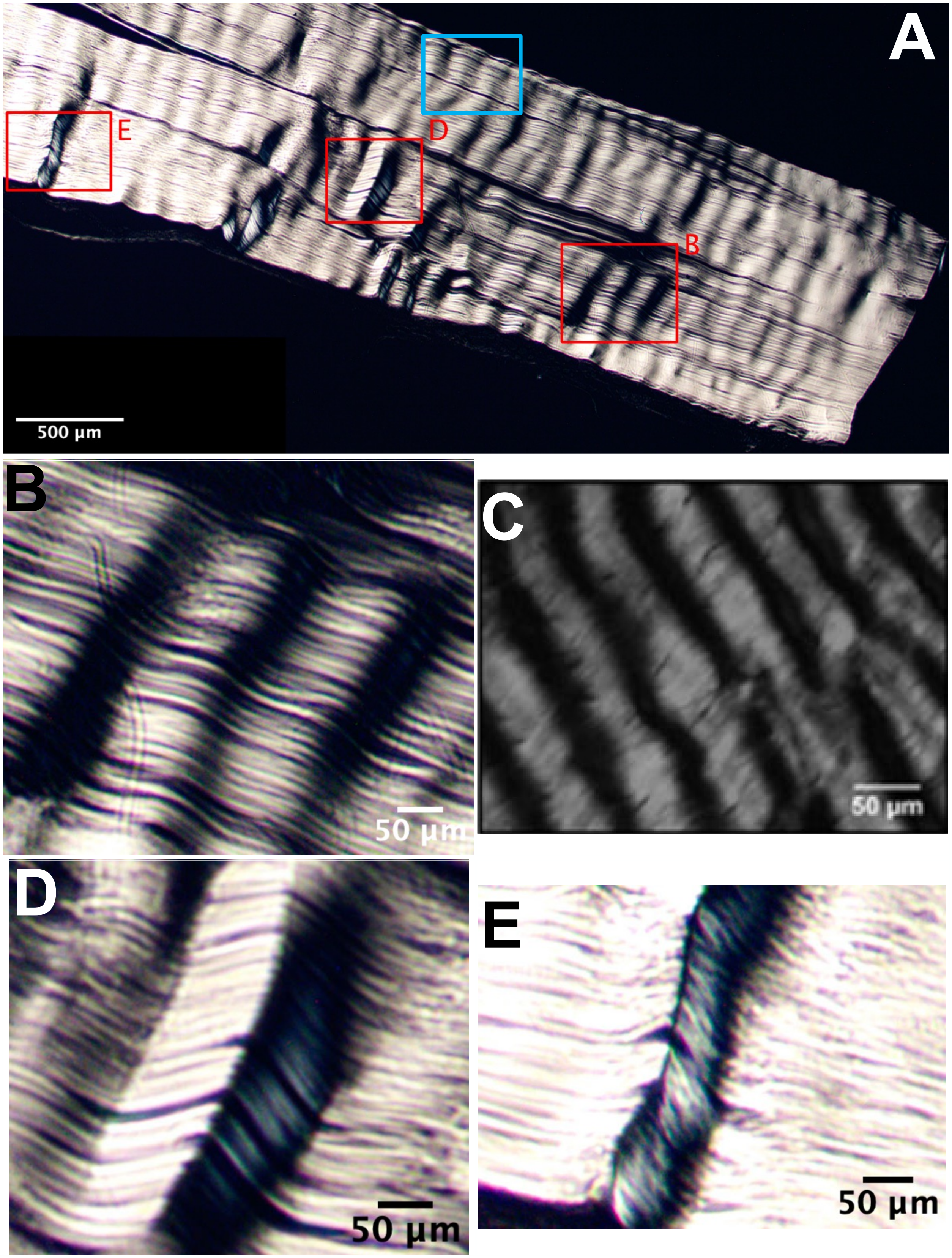
A
E
D
B
500 µm
B
50 µm
C
50 µm
D
50 µm
E
50 µm

Figure 4.23: (A) PLM image of a CDE test tendon containing varying degrees of damage, with the tissue in the blue box demonstrating one example of typical CDE tendon crimp. (B) Magnified image of the red box labelled (B) in panel (A), showing tissue resemblant of patellar tendon tissue. (C) PLM image of cadaveric patellar tendon tissue (adapted with permissions from Sage Publications to remove part of a figure from a study by Schmidt et al.[164], see Appendix II for further detail). (D) Magnified image of the red box labelled (D) in panel (A), illustrating a sharper bent tissue feature than that of panel (B) but not a kinkband according to the criteria used in the current study. (E) Magnified image of the red box labelled (E) in panel (A), containing a confirmed kinkband on the left and a sharply bent tissue feature on the right, similar to the feature in panel (D).

After identifying all kinkbands using the PLM images of the sections imaged through fluorescence microscopy, a qualitative analysis found no relation between kinkbanding and molecular denaturation. When viewing kinkbands on PLM images, there was always a change in colour (almost always black) along the kinkband's axis of propagation. It was expected that this absence of colour along the kink would be a result of either tissue oriented in a direction where it would not produce a detectable signal, or a denaturation of the molecules along the kink, preventing their ability to produce signal. If the black band along the kink axis was a result of denatured molecules, this would correlate to a strong signal in the same locations on the fluorescence microscopy images. Seeing as this was not observed, the inclination is that molecular denaturation is not an intrinsic component of kinkbanding.

Considering the results of the first two imaging techniques, it became much easier to interpret the many SHG microscopy results. It was hypothesized that kinkbands imaged through SHG microscopy would have either very high ρ values, or an absence of fit due to denatured molecules along a kinkband. For kinkbands with unfit pixels due to denaturation, the minimum 50 intensity count criteria when fitting pixels would not be met and these denatured kinkbands would occur with the same frequency as in the fluorescence microscopy images. When sifting through the unfit pixels of kinkbands, it was rare to encounter one that was unfit due to a lack of intensity, which supported the inability to find denatured kinkbands through the fluorescence microscopy images. The sufficient intensity observed in pixels along a kinkband raised even more questions, since almost no pixels were fit along any of the kinkbands.

Comparing the PLM images and the SHG microscopy ρ maps (Figure 4.24 and 4.25), there was a clear relationship supporting the kinkband inclusion criteria utilized in this thesis. Features appearing on the PLM images as potential kinkbands, which barely failed to meet criteria, having a change in colour occurring over a distance slightly greater than 1 μm, contained minimal or no unfit pixels in the corresponding locations of the ρ maps. As the distance required for a change in colour decreased, while still failing to meet criteria, the number of unfit pixels along the kink increased. In the fit pixels located along the kink axis of the near kinkband features, large ρ values were present, subsiding with increasing distance from the axis of kinking (Figure 4.26). The R^2 values accompanying pixels were typically lower nearing the suspected kink, indicating a worse fit. In addition to large ρ values, in many instances, differing κ values on either side of a feature confirmed as a kinkband, or narrowly failing to meet the kinkband criteria were observed. In cases where this result was present, pixels on each side of the kink had a uniform ρ value, differing between the two sides, as opposed to only pixels along the kink showing disorder. This suggests that the uniform larger ρ values on one side of a kinkband are a product of the tissue laying out of plane at a uniform angle.

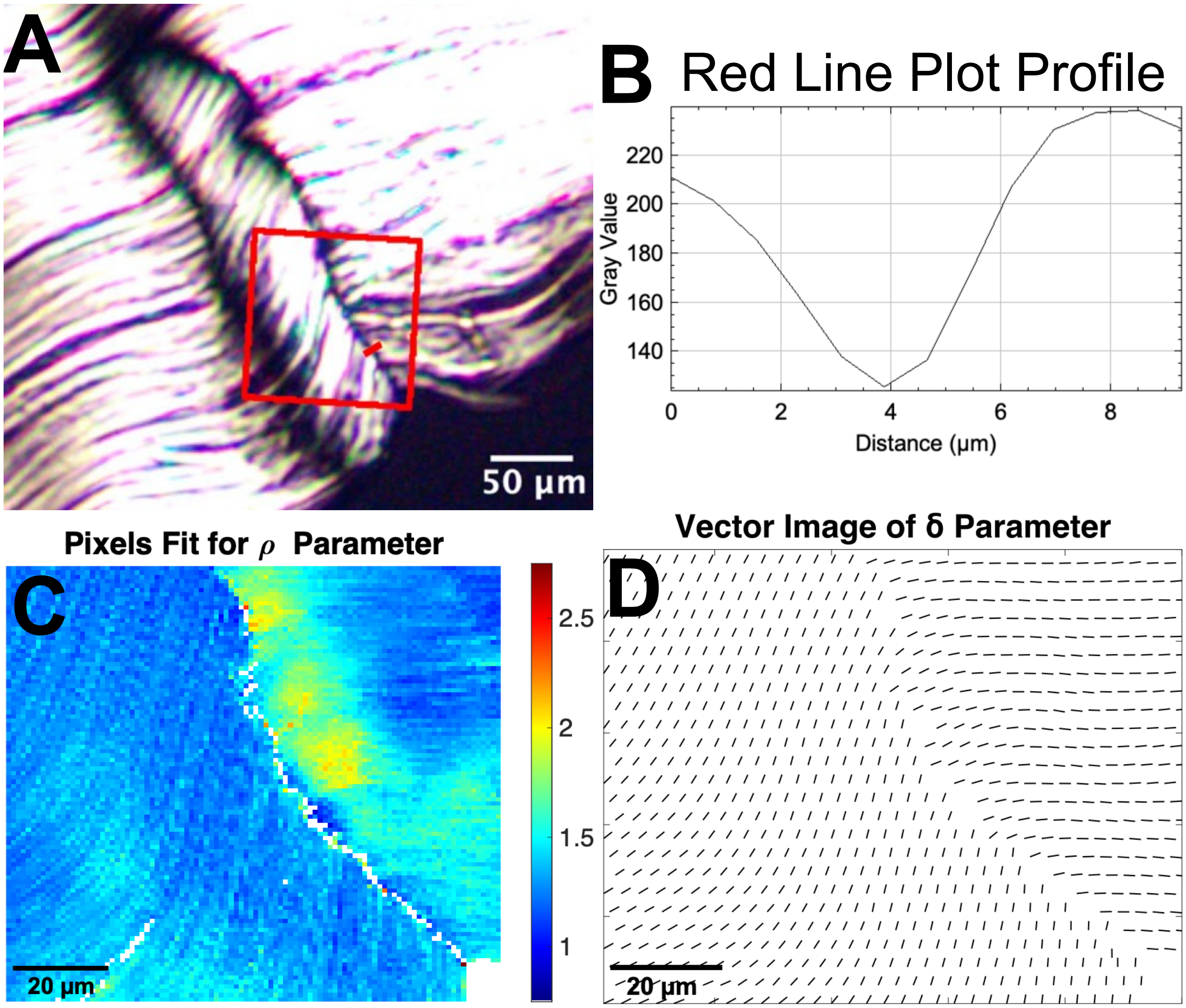

Figure 4.24: Panels (A-D) represent a confirmed kinkband in a CDE test tendon. (A) A PLM image of the kinkband, with the red box indicating the scan window for SHG microscopy. (B) The plot profile of the red line inside of the red box in panel (A). The plot profile shows that the kinkband inclusion criteria are both met with a width of 0.63 µm, at the location of the red line. (C) A single PIPO scan with all pixels fit for the parameter ρ, showing a clear lack of fit pixels along the kink axis. (D) The vector image of the δ parameter, where tissue on either side of the kinkband has a sharp change in angle.

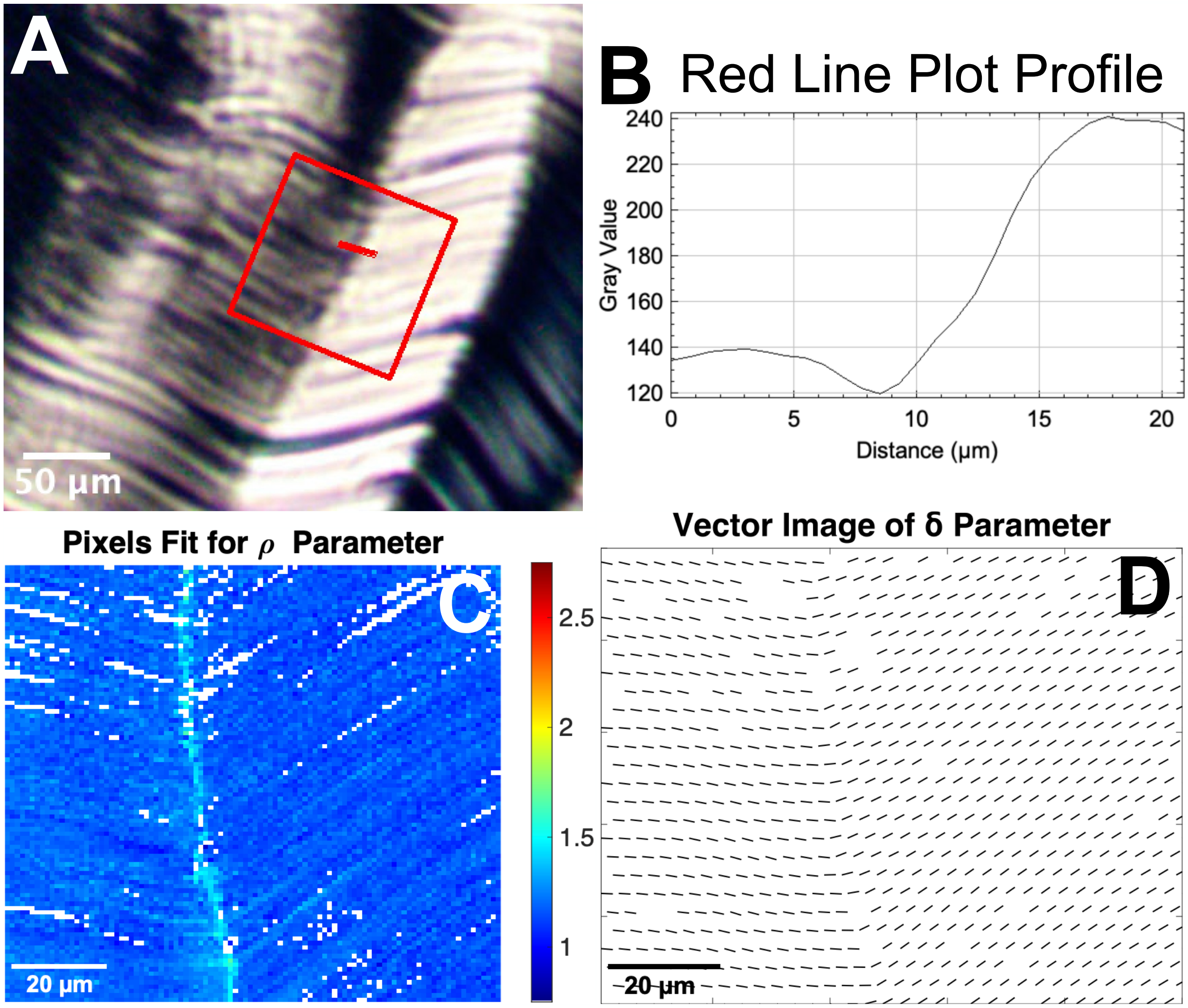

Figure 4.25: Panels (A-D) represent a feature failing to meet the kinkband criteria in a CDE test tendon. (A) A PLM image of the feature, with the red box indicating the scan window for SHG microscopy. (B) The plot profile of the red line in the red box of panel (A), showing that the gray scale change of 10 occurs at a width of 1.15 µm, nearly qualifying as a kinkband. (C) The ρ image, where a change in value along the kink axis is apparent, accompanied by the odd unfit pixel, though a clear difference still exists from Figure 4.24 (C). (D) The vector image of the δ parameter shows a change in direction along the kink axis, though it is not as sharp and distinct as that of the analogous confirmed kinkband image in Figure 4.24 (D).

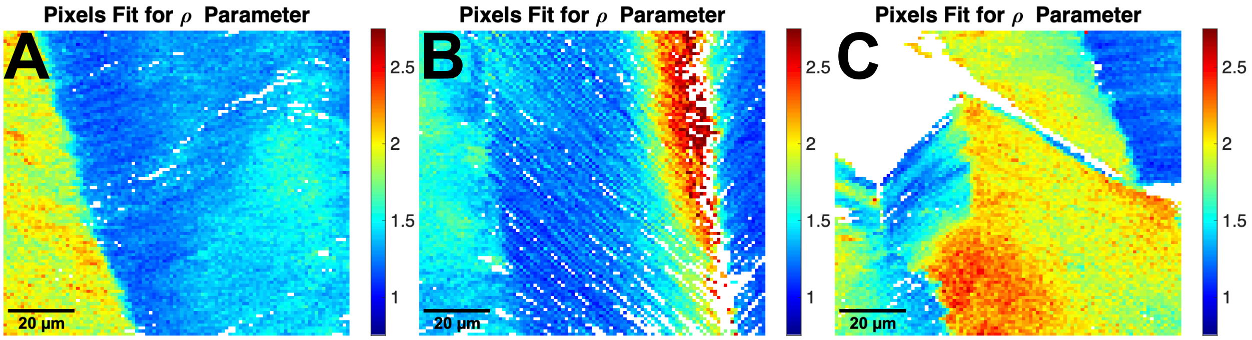

Figure 4.26: PIPO scans of features nearly qualifying as a kinkband from 3 different CDE test tendons, fit for the parameter ρ. (A) The feature failed to meet criteria, having a width of 1.4 µm, but demonstrating how the ρ value distribution is presented when either side of the kink are at different angles. Not only does the ρ value of tissue on either side of the kinkband differ but the ρ values on either side differ from that along the kinkband itself. (B) This feature looks like other confirmed kinkbands, but it failed to meet criteria with a width 1.09 µm. Quite a few pixels are unfit along the kinkband, and the damage is becoming very localized near the kink axis. Additionally, the ρ values of pixels moving away from the kinkband gradually approach those observed in healthy regions (1.16) and appear similar on either side of the kinkband once far enough away. The pixels on the right of the kinkband return to a healthy ρ value over a shorter distance than those on the left. (C) This image shows several kink-like features, ranging in widths from 1.03–1.5 µm, and again showing the presentation of tissue on either side of a kink laying at different out of plane angles. Locations closer to meeting the kinkband inclusion criteria on the PLM image display a result similar to panel (B), where some pixels are unfit and a shorter distance from the kink is required for a return to typical healthy ρ values.

Investigating the ρ values of pixels in features at various levels of kinking seemed random when only considering the ρ maps. However, when considering various levels of kinking using the different SHG microscopy fit parameters, together with the PLM maps, a relationship was suspected. Though a quantitative analysis was not performed, there appeared to be a correlation where the sharpness of a kink was proportional to, (i) the distance over which a color change occurred using the kinkband inclusion criteria (PLM), (ii) the distance from a kink to the point where pixels returned to healthy ρ values (SHG), (iii) the angle between tissue on either side of a kink using the vector image of the δ parameter (SHG), and (iv) the pixels along a kink when looking at the ρ fit PIPO scan (SHG).

Features appearing as potential kinkbands that failed to meet the inclusion criteria due to a change in color occurring over a large distance were indicative of structural damage that occurred over a distance proportional to the distance required for a colour change. This led to a greater distance from the kink required for pixels to return to a healthy ρ value (Figure 4.27 B). The large distance over which structural damage occurred meant the vector image of the δ parameter did not have a large difference in angle between tissue on either side of the kink (Figure 4.27 E). The damage was dispersed over the area of the color change and was consequently less concentrated due to the relatively large distance of the color change.

As the distance required for a color change decreased damage became more localized along the kink. The distance from the kink for ρ values to return to healthy decreased. The vector image of the δ parameter displayed a greater difference in tissue angle on either side of the kink. Pixels along the kink displayed larger ρ values, with pixels eventually failing to fit.

For confirmed kinkbands, the distance from the kink required for pixels to approach healthy ρ values continued to decrease, proportional to the distance required for a color change using the kinkband inclusion criteria (Figure 4.27 A and C). In some cases (Figure 4.27 A) the pixels immediately adjacent to the kinkband displayed healthy ρ values, suggesting that the damage may be so localized that it is all contained within the unfit pixel(s). Sharper kinkbands displayed increasing differences between the tissue angle on either side of the kink, shown by the vector image of the δ parameter (Figure 4.27 D and F). The string of unfit pixels was typically 1-2 μm wide, like that of the kinkband inclusion criteria (≤ 1 μm from the center).

This progression suggests that as fibrils continue to buckle, the kink gets sharper, and the tissue disorder becomes more localized along the kinkband. As an insufficient number of kinkbands were found in the control tendons, all kinkbands viewed through SHG microscopy underwent cyclic buckling, supporting the case that progressive buckling causes sharper fibril kinking. Future works may use the vector image of the δ parameter to investigate if a specific angle is an associated property of kinkbands, as crimp has a characteristic angle[40].

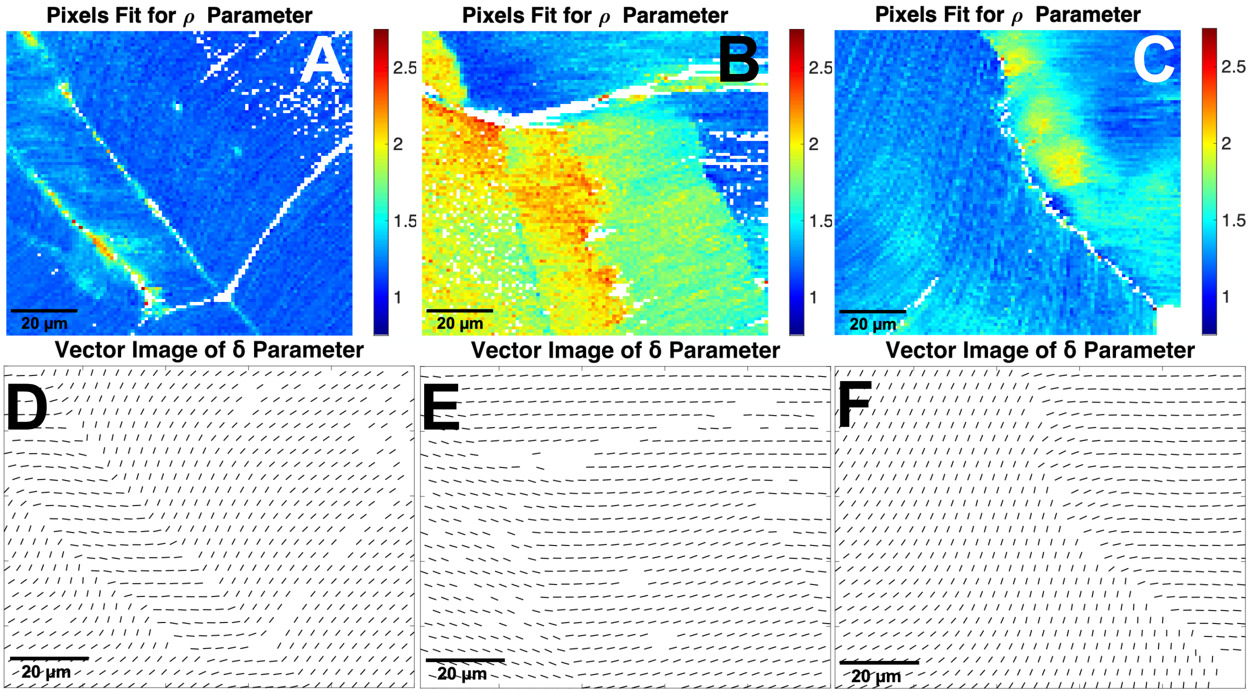

Figure 4.27: Panels (A-C) show PIPO scans fit for the parameter ρ. (A) This PIPO scan contains two kinkbands from an SDF test tendon, where the kinkband on the left and right met the kinkband inclusion criteria having widths of left: 0.3-0.75 µm and right: 0.35-0.65 µm, respectively. In the right kinkband pixels return to healthy ρ values almost immediately exiting the kinkband. (B) A non-kinkband feature that met the first requirement of the kinkband inclusion criteria at a width of 1.45 µm. Large ρ values appear dispersed across the PIPO scan and require a large distance to return to healthy. (C) A single kinkband from a CDE test tendon, where the kinkband inclusion criteria was met at a width of 0.63 µm. Pixels return to healthy ρ values almost immediately on the left of the kinkband but require a slightly greater distance when translating right. Panels (D-F) show the vector images of the δ parameter corresponding to panels (A-C) respectively. (D) Very

sharp change in tissue direction along the kinkbands is observed by the vectors. (E) Although there is a clear change in ρ value along the right of the image in panel (B), the vector image does not show a very sharp change in tissue, as this feature is not a kinkband. (F) The kinkband again shows a sharp change in vector direction along the kink.

These results all help to understand the structure of a kinkband, but a question still looms. If the molecules along a kinkband are not denatured, why do the SHG microscopy pixels along each kinkband not fit with C_6 symmetry? Could it be that prior to kinks becoming sharp enough to be considered a kinkband, the kink width is large enough that it is dispersed over multiple pixels? For larger kink widths present prior to kinkbanding, any fibril crossing would be from two different fibrils crossing, which has previously been shown to result in successfully fit pixels with large ρ values[20], possibly greater than 3. Perhaps, when a kink becomes so sharp that it is contained within one pixel, an individual fibril crosses over itself, as shown through scanning electron microscopy[95]. The result of this fibril kink would be the orientation of tissue in multiple directions and planes, as kinking is three-dimensional. Is it possible that a single pixel along a kinkband can contain collagenous tissue in too many unique orientations for it to be assumed a cylindrical rod with circular symmetry? As this was the assumption made when deriving the equation used for fitting each pixel. It was observed that nearly every unfit pixel resulted from an R^2 value below the 0.8 requirement set. To further investigate this finding and determine why kinkbanded pixels were unable to fit to this symmetry, the plots of several pixels, spaced out along each kinkband were assessed (Figure 4.28).

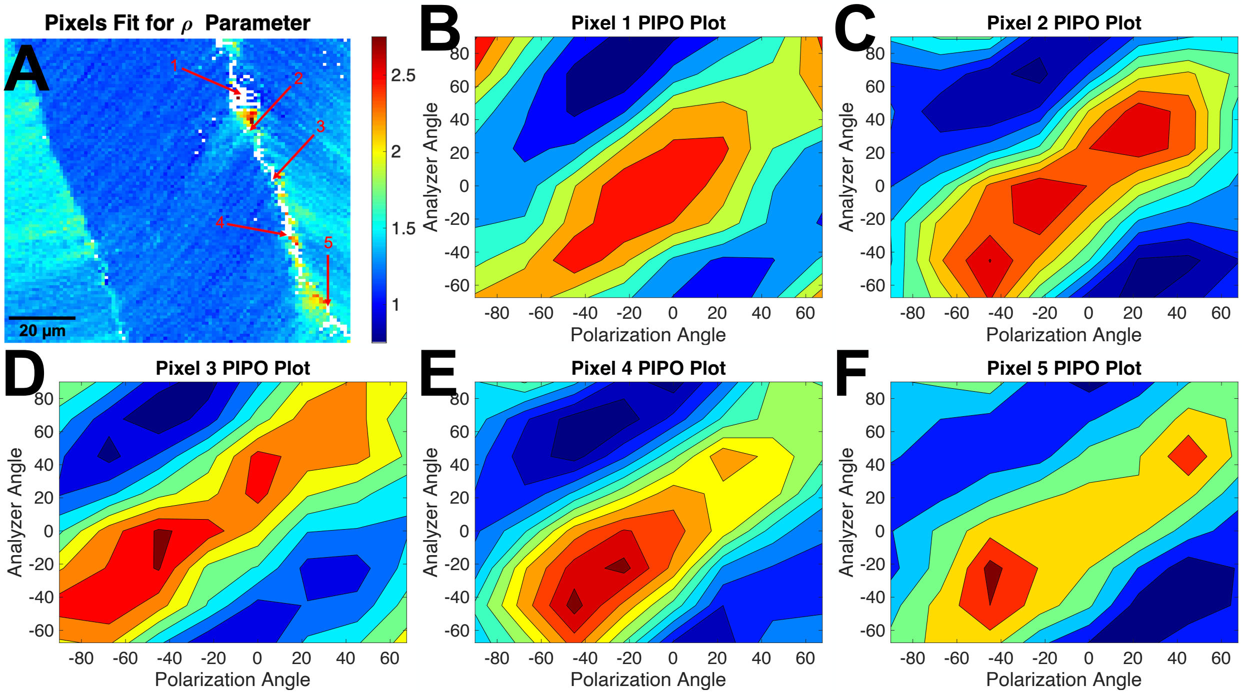

Figure 4.28: This figure shows pixels having various goodness of fits located along a kinkband confirmed using the criteria of this thesis. The differing goodness of fit values help to illustrate how a pixel becomes more elongated as the goodness of fit value decreases. (A) An SHG-PIPO scan fit for the parameter ρ, containing one kinkband, located on the right of the scan. Each of the following pixel plots are labelled and located along the kinkband. (B) Pixel intensity of 142 counts and attempted fit with R^2 = 0.59. (C) Pixel intensity of 201 counts and successful fit with R^2 = 0.89. (D) Pixel intensity of 163 counts and attempted fit with R^2 = 0.63. (E) Pixel intensity of 229 counts and attempted fit with R^2 = 0.76. (F) Pixel intensity of 127 counts and attempted fit with R^2 = 0.69.

When looking at the unfit pixels, it became evident that the typical dog bone shaped plot indicative of a well fit pixel was not present. Rather, the pixel plots were elongated, with those far from the goodness of fit threshold being more elongated than those on the cusp of fitting. For a pixel where all fibrils are oriented in the same direction, the fibrils provide signal strength in a uniform direction. When fibrils cross, the signal adds in the center where they cross but cancels as components point in opposite directions[20]. In previous instances of fibril crossing, there was no report of an inability to fit pixels, or an elongated nature of the pixel's plot, suggesting something other than fibril crossing may be occurring within these pixels. Oddly, this result of elongated pixels was previously observed in cancerous thyroid tissue, though the root cause of this unique structure was unknown. While it is unclear why pixels along a kinkband poorly fit, the proposed hypothesis is that unfit pixels result from excessive unique orientations of collagenous tissue within one pixel, causing the assumptions of treating fibrils in a pixel as a cylindrical rod with circular symmetry to be poor. What is clear, is that unfit pixels do not adhere to C_6 symmetry. Perhaps these tissue locations would be better understood through some other non-linear scattering microscopy. Exploring what is happening within kinked locations of fibrils may help to improve an understanding of how this precursor to tendinopathy can be treated and better prevented.

4.5.3 Kinkband Formation Model (KFM)'

At the time, the 'CUE' model utilized the available knowledge to suggest an idea for how tendinopathy was initiated and formed. With the newfound knowledge presented in this thesis, the prior model can be expounded, specifically pertaining to the structural changes occurring between the cyclic buckling of tendons and the kinking of individual fibrils. Here, the kinkband formation model 'KFM' will be outlined, using features at various stages of kinkband formation as examples.

Stage 0: Buckling Commences

The KFM begins with the buckling of individual fibrils, prior to any damage.

Stage 1: Dispersed Fibril/Fibre Bending

At this stage many fibrils begin bending, eventually leading to fibres bending. This results in a decrease in angle between tissue on either side of the bending axis (BA), though the fibres are not yet kinked. The bending radius of curvature is similar to that of a more aggressive/sharp crimp. The tissue at and around the axis of the bending begins to lose structural order, dispersed over an area having a width on the magnitude of 10s of µm, as seen by the black bands between bending axes in Figure 4.29.

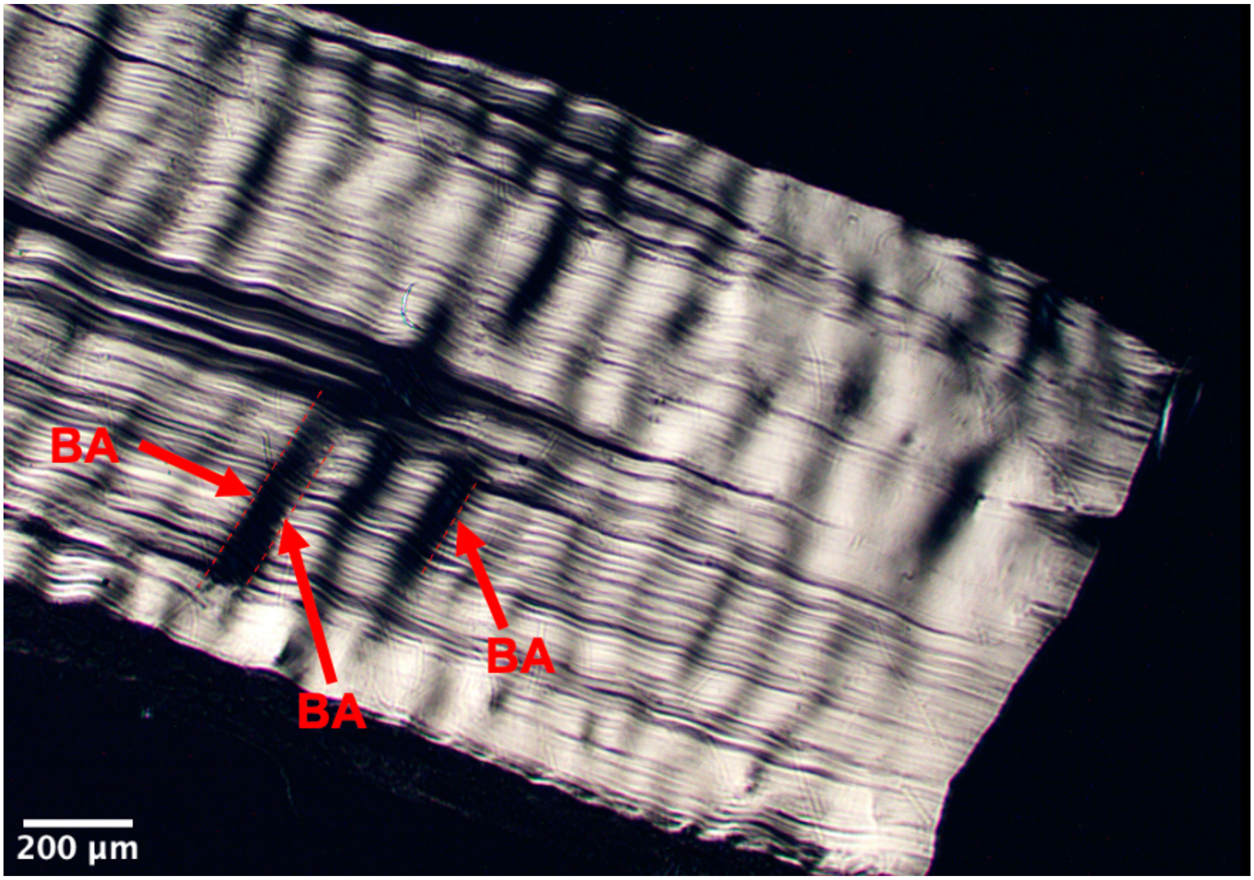

Figure 4.29: KFM Stage 1 damage: The top portion of the CDE test tendon tissue displays a normal crimp patten, while on the bottom portion of tissue there are 3 labelled bending axes (BA), denoted by the red dotted lines. The tissue in stage 1 clearly presents differently from normal crimp, though the changes in tissue direction maintain large radii of curvatures.

Stage 2: Concentrated Fibril/Fibre Bending

Fibrils and fibres continue to bend, causing a decrease in angle between tissue on either side of the bending axis. The tissue structure becomes very disordered along the bending axis, with the surrounding tissue tilting from its original position. This change in tissue angle continues to propagate to neighbouring fibrils on either end of the bending region, lengthening the bending axis. As the bend radius of curvature decreases, the structural disorder becomes for localized along the BA.

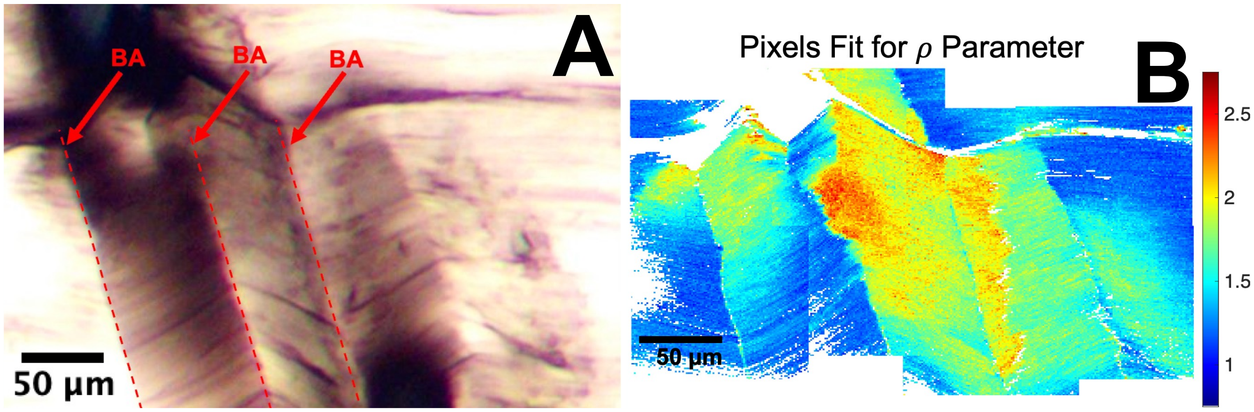

Figure 4.30: KFM Stage 2 damage: (A) PLM image of a CDE test tendon in stage 2 of the KFM, containing 3 bending axes (BA), depicted by the dashed red lines. (B) The corresponding stitched SHG microscopy map fit for the parameter ρ. Along each BA, there are ρ values visibly differing from surrounding pixels. These values gradually change as distance from the BA increases. While the disorder is still very dispersed, it is important to note how ‘dispersion of disorder’ is displayed. This is not the large area of high ρ values, resulting from tissue resting out of plane, but rather the distance required for ρ values to reach a steady state, as they move away from the BA.

Stage 3: Initiation of Kinking

Fibres continue to bend, and individual fibrils begin to kink along the bending axis, adopting the title of kinking axis (KA). A smaller radius of curvature (sharper change in tissue direction) is associated with kinked tissue compared to bent tissue, meaning changes in tissue direction occur over a shorter distance. Since the change in tissue direction is sharper in stage 3 than in stage 2, the structural changes do not span as great of a distance and instead become increasingly concentrated along the KA. As concentration increases along the KA, tissue experiencing minor structural changes in stage 2, far from the BA, display a return to typical structural order and structural changes are relieved, indicating that stage 2 damage is still recoverable, while kinking of fibrils may not be. It should be noted that through SHG microscopy, if all tissue on one side of the kinking axis is of uniform ρ value, regardless of whether it is higher than typical, this just indicates fibrils are positioned out of plane and the feature may still be in stage 3, so long as the ρ value along the kinking axis differs. At this point the feature would nearly pass the kinkband inclusion criteria, though the kinking has yet to reach the point of fibre kinking. As buckling continues, this fibril kinking will continue to propagate to neighbouring fibrils.

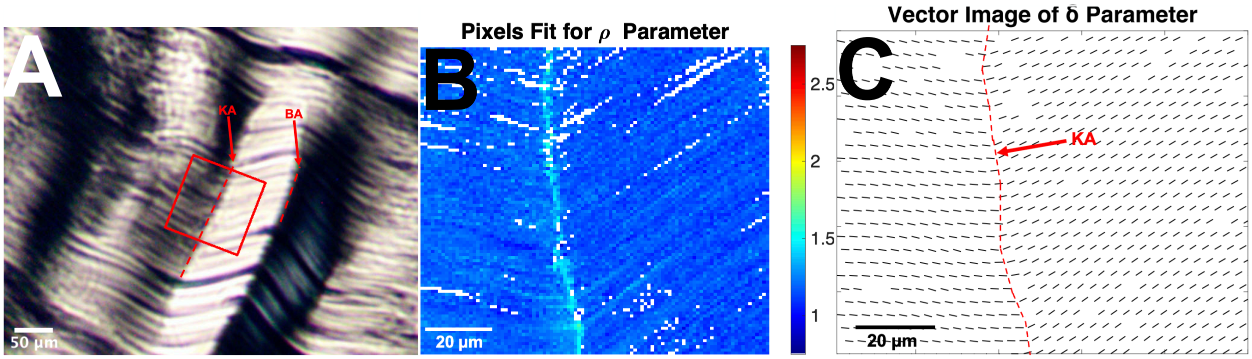

Figure 4.31: KFM Stage 3 damage, (A) PLM image of an SDF test tendon, with the bending axis (BA) and kinking axis (KA) of two features depicted by the dotted red lines. While it appears differently, as the KA is not black, as seen in most kinkbands, this feature nearly meets the kinkband inclusion criteria, contributing to its stage 3 status. (B) A PIPO scan of the region within the red box in panel (A), fit for the parameter ρ. Pixels along the kinking axis are clearly of larger ρ value than pixels in the surrounding areas, with few pixels dispersed along the kink failing to fit. (C) The same PIPO scan in panel (B), fit for the vector image of the δ parameter, showing a clear change in tissue orientation on either side of the KA.

Stage 4: Kinkband Present

At this stage, the kinkband is fully formed. While the kinkband may continue to propagate to neighbouring fibrils and fibres along the KA, all fibres within the kinkband are kinked. As buckling continues and fibres become kinked, the structural order of the tissue becomes increasingly concentrated along the KA and the change in tissue direction between either side of the kink increases. The increasing concentration of damage within the KA results in tissue on either side of the KA returning to normal, concealing all damage within the kink itself. This indicates that all structural changes discussed in the KFM are recoverable, at least to some extent, aside from kinking. Even if a kinked fibril or fibre were unkinked, it has experienced a form of plastic damage that is not recoverable. This stage of fibre kinking and a fully formed kinkband is suspected to be the most extreme degree of damage which will be achieved without a tensile loading component.

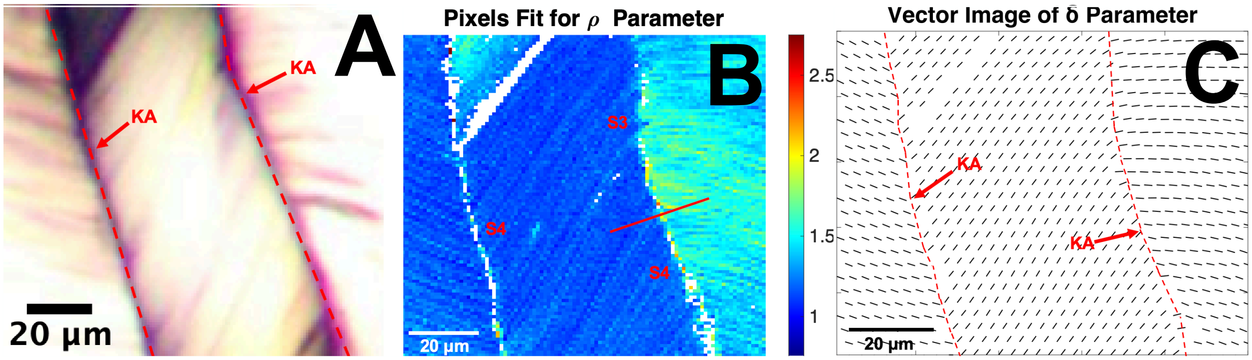

Figure 4.32: KFM Stage 4 damage, (A) PLM image of a CDE test tendon with two kinkbands present, travelling along the kinking axis (KA). (B) The SHG microscopy PIPO scan of the location in panel (A), fit for the parameter ρ. Two kinkbands at stage 4 (S4) of the KFM are present. The kinkband on the right, propagating upwards, transitions from S4 to S3 as it crosses the solid red line, shown by the increasing ability of pixels to fit. Looking at the kinkband on the left, the return of ρ values to structural order is apparent in pixels immediately adjacent to the unfit pixels along the KA. This demonstrates the concentrated structural disorder along the KA that relieves structural disorder in tissue moving away from the kink. (C) The PIPO scan of panel (B) fit for the vector image of the δ parameter. The labelled KA show a very sharp change in fibril direction for the left kinkband and bottom half of the right kinkband, with the change in fibril orientation becoming less drastic for the feature remaining in S3.

4.6 Conclusions

Hypothesis (i): Following cyclic buckling, fluorescence microscopy will demonstrate an increased presence of denatured collagen in test tendons relative to their match-paired controls.

Hypothesis (i) Result: This hypothesis was confirmed, using the results of the fluorescence microscopy analysis approach 2, which indicated a significantly greater percent of denatured collagenous tissue in cyclically buckled tendons (8.1%) compared to controls (1.0%).

Hypothesis (ii): Following cyclic buckling, fluorescence microscopy will demonstrate that a greater product of denatured collagen between test and match-paired control exists in CDE tendons, compared to SDF tendons.

Hypothesis (ii) Result: The second hypothesis was rejected, as the difference in the amount of denatured collagenous tissue between match-pairs was not significantly affected by tendon type.

Hypothesis (iii): In all tendons used in this study, kinkbands observed through polarized light microscopy will often display a heightened fluorescence signal along the center of the kinkband.

Hypothesis (iii) Result: There was no observed correlation between kinkbanding measured through PLM and denatured tissue along the kinking axis, assessed through fluorescence microscopy, rejecting the third hypothesis.

Hypothesis (iv): The kinkband presence observed in tendons subject to cyclic buckling will be greater than that observed in the controls.

Hypothesis (iv) Result: Cyclically buckled tendons contained a greater density of kinkbands than control tendons, measured with PLM images, confirming this hypothesis.

Hypothesis (v): Among the cyclically buckled tendons, the CDE tendons will have a greater kinkband presence than the SDF tendons.

Hypothesis (v) Result: This hypothesis was rejected, as tendon type did not significantly affect kinkband density within the buckled tendons (buckled tendon kinkband density, CDE: 0.044 ± 0.046 and SDF: 0.045 ± 0.081 [mm/mm^2]).

Hypothesis (vi): Locations of a tissue section appearing healthy through PLM imaging will have the same ρ values, regardless of whether they were cyclically buckled or not.

Hypothesis (vi) Result: A significant difference was not observed between the cyclically buckled and control tendon ρ values, at locations categorized as healthy, confirming this hypothesis.

Hypothesis (vii): Locations containing a kinkband, or some other abnormality, will have greater ρ values than healthy appearing locations.

Hypothesis (vii) Result: This hypothesis was confirmed, shown by the larger ρ values present in locations categorized as abnormal, compared to those categorized as healthy.

Hypothesis (viii): If hypothesis vii is true, the kinkbanded or other abnormal regions will have greater ρ values when present in tendons belonging to the test group, compared to the control.

Hypothesis (viii) Result: Since hypothesis (vii) was confirmed, hypothesis (viii) was investigated. Though the ρ values of cyclically buckled abnormal regions were greater than those of healthy regions, the interaction between treatment and condition was not significant, so this hypothesis was rejected.

Hypothesis (ix): The ρ values of healthy regions, specifically in the control samples, will be greater in SDF than CDE tendons.

Hypothesis (ix) Result: This very important hypothesis was confirmed, showing the first reported result of ρ values differing between the CDE and SDF tendons (observed in healthy regions). In healthy regions of the control samples, who's values are more indicative of the intrinsic ρ values of these tendons, CDE and SDF tendons had ρ values of 1.14 ± 0.02 and 1.21 ± 0.05, respectively. The values were supported by healthy regions in the cyclically buckled samples having ρ values of 1.16 ± 0.02 and 1.19 ± 0.03 for CDE and SDF tendons respectively.

Hypothesis (x): Kinkbands observed through PLM will either have very high ρ values along the kink, or an absence of signal. The absence of signal will result from the denaturation of molecules and these denatured kinkbands should occur with the same frequency as in the fluorescence images.

Hypothesis (x) Result: This hypothesis was confirmed, as kinkbands did have either large ρ values or an absence of fit pixels along the kink, though the rationale for the absence of fit was incorrect, as denaturation was not the cause of the pixel's inability to fit.

Hypothesis (xi): The ρ values associated with kinkbands in SDF tendons will not increase as much as the ρ values associated with those of CDE tendons, relative to normal.

Hypothesis (xi) Result: The ρ values of pixels in kinkband regions was found to be larger in SDF tendons (1.57 ± 0.07) compared to CDE tendons (1.36 ± 0.11), rejecting this hypothesis.

Hypothesis (xii): The structural order of tissue immediately adjacent to kinkbands will be slightly more disordered than normal but tissue further from the kinkband will have typical structural order[30,95].

Hypothesis (xii) Result: This hypothesis was confirmed, as tissue closest to the KA of a kinkband was typically disordered, with distance from the KA allowing structural order to be regained.

Hypothesis (xiii): The tissue along and on either side of a kinkband will often lay at different angles.

Hypothesis (xiii) Result: This hypothesis was confirmed, as the vector images fit for the δ parameter showed a sharp change in tissue direction on either side of the KA, though the out of plane angle did not appear to differ between either side of the KA in most confirmed kinkbands.

A structural analysis of CDE and SDF tendons following cyclic buckling, using fluorescence microscopy, PLM, and SHG microscopy have demonstrated that cyclic buckling causes structural changes. Within these changes, tendon type generally does not appear to affect the structural response. At the molecular level, fluorescence microscopy showed that cyclic buckling causes an increase in percent of denatured tissue, with no apparent pattern of where denaturation occurs. Using some novel criteria for defining a kinkband, PLM images demonstrated that cyclic buckling caused an increase in overall kinkband presence. Through SHG microscopy, a smaller ρ value was observed in positional relative to energy-storing tendons. SHG microscopy also led to the determination that cyclic buckling caused an increasing structural disorder, and an increasing structural disorder along the kinking axis of kinkbands. Finally, the kinkband formation model 'KFM' was formulated to explain the structural presentation of tissue at various stages of kinking.

Chapter 5: Functional Analysis – Mechanical Testing

5.1 Background

Tensile testing is a commonly utilized form of mechanical testing, which provides important mechanical properties of a material while being simple to use, low-cost to perform each test, and accessible at most institutions. Tensile tests are an effective method of measuring changes to a material's mechanical properties, following other mechanical testing. Tensile testing can also be used with imaging techniques to draw conclusion surrounding the structure-function relationship of a sample.

As discussed in Chapter 1.1.2, tensile testing has helped further an understanding of tendon mechanics by determining parameters such as the UTS and elastic modulus of various tendons, across several animal models, and relating those results to the mechanical properties of human tendons. In this chapter, mechanical testing was used to better understand changes to tendon properties as a result of cyclic buckling, as well as to provide further literature surrounding the mechanical properties of ovine tendons.

5.2 Hypotheses and Rationale

Hypothesis (xiv): CDE tendons will have a larger ultimate tensile strength and modulus of elasticity (E) than SDF tendons.

Rationale: This is in accordance with the ovine and other large animal literature[17,52,54–56].

Hypothesis (xv): Cyclic buckling of tendons will result in decreased values for UTS and E, relative to the controls.

Rationale: As it was hypothesized that cyclic buckling would cause structural changes, the resulting damage, if of sufficient volume, should compromise mechanical properties.

Hypothesis (xvi): Cyclic buckling will have a more severe effect on the UTS and E in the positional CDE tendon, than the energy-storing SDF tendon.

Rationale: This relates to the inherent characteristics of each tendon. Physiologically, energy-storing tendons undergo greater volumes of cyclic loading, and as a result are more fatigue resistant than positional tendons[42,43,52].

5.3 Methodology

Experimental

Following the cyclic buckling procedures outlined in Chapter 3.4, test and match-pair control tendons (n = 5 pairs per tendon type) were wrapped in PBS-soaked gauze and transported to the SMU engineering laboratory for tensile testing. A camera was placed on a tripod, and the entire setup and tensile testing procedure was video recorded. First, a marker was used to place one dot on either end of the 20 mm of the tendon located at the center, as a reference for what would be the inter-grip sample length. One end of the tendon was clamped into the upper grips of an MTS C43-series electromechanical test system with custom 3-D printed grip inserts (Figure 5.1 and A I.1). After clamping the end of the tendon into the upper grip, the load on the computer running the program was zeroed. At this stage the unclamped portion of tendon remained in the PBS-soaked gauze, to maintain hydration. The upper grips were lowered to the point where an inter-grip length of 20 mm was estimated, using the marked dots. The gauze remained wrapped around the inter-grip portion of tendon, while the other end of the tendon was tightened into the lower grips. The tendon was pulled to a nominal tensile load of 0.7 N, indicating all slack was removed from the sample. The crosshead distance was then zeroed. In the same plane but adjacent to the tendon, a ruler was held in the camera frame of view, providing a scale for frame-by-frame measurements and determination of inter-grip length in the recorded video (actual inter-grip length was measured as 18.2 ± 2.2 mm). Finally, the gauze was removed, and a marker was used to place two dots on the tendon, within the inter-grip segment, to monitor for any grip slippage. Data were collected at a rate of 10 Hz for force, displacement, and duration, throughout testing. Finally, testing commenced, beginning with preconditioning. Samples underwent 10 preconditioning cycles, to a strain of 5% (of the estimated 20 mm sample inter-grip length), at a strain rate of 10%/s. Following the 10th cycle, the tendon was pulled to rupture at a strain rate of 10%/s. This entire process was then repeated using the other paired tendon.

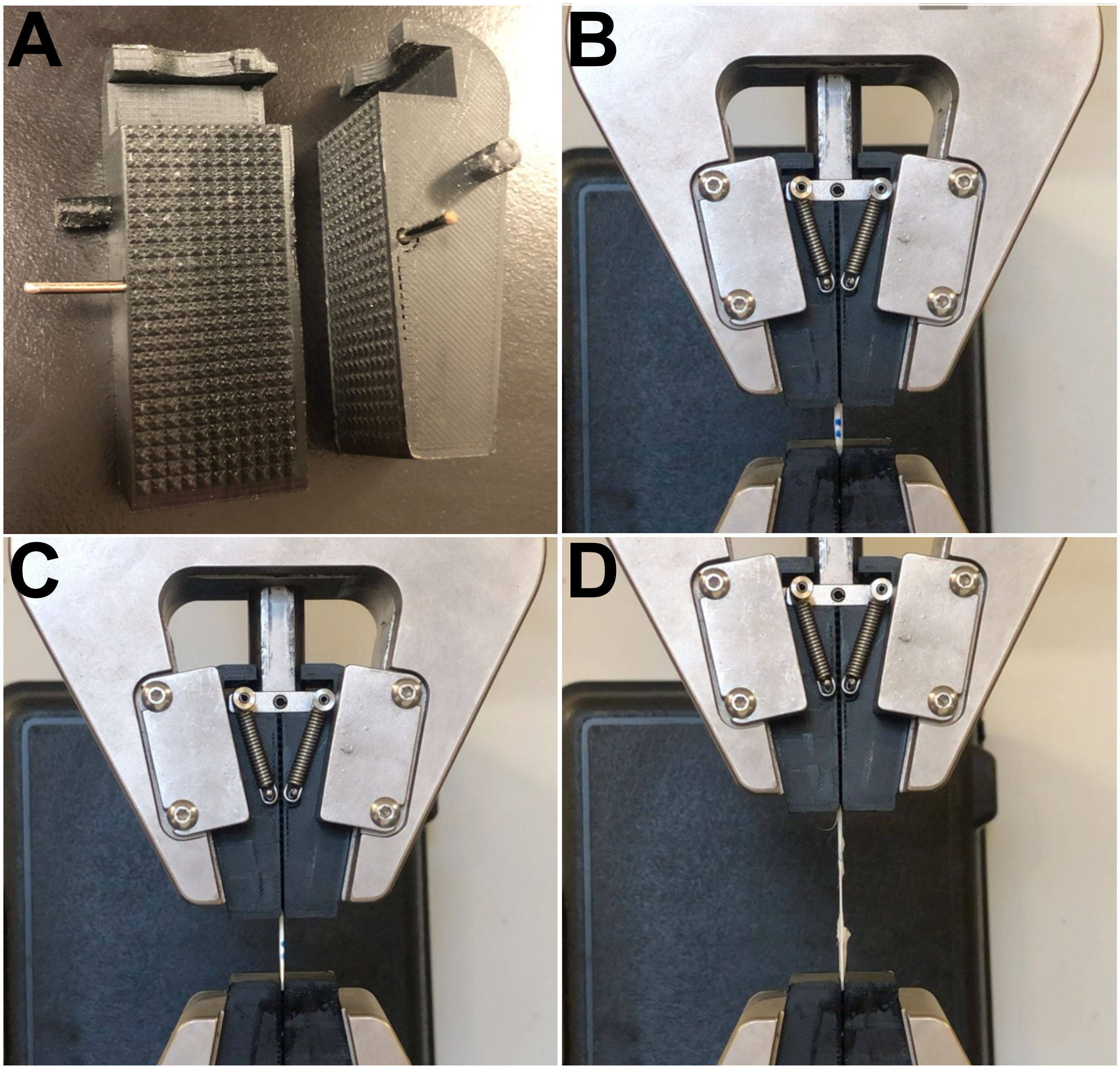

Figure 5.1: (A) Photograph of the custom designed tensile testing grips. Grips were 3-D printed using ECO-ABS filament. To maximize the clamping force exerted on a sample, grips utilized a design of pyramidal teeth, having a peak to valley mate between grips, to ensure a snug fit around the clamped tendon. Panels (B-D) show individual frames extracted from a video of the tensile testing process of a SDF control tendon. (B) Tendon is subject to a tensile force of 0.7 N, but preconditioning has not commenced. (C) Preconditioning has finished and tensile pull to rupture has begun but rupture has not yet occurred. (D) Tendon post rupture. Though the tendon was not fully severed it is no longer able to bear load.

Data Analysis

Once all testing was concluded, the UTS and modulus of elasticity for each tendon were determined by using the tensile testing data and the cross-sectional area found through the methods of Chapter 3.4. The data were analyzed as follows. Each tendon was approximated to have a longitudinally uniform, elliptical cross-sectional area, measured as πab, where a and b are the major and minor diameters, respectively. The 'force' column of each tensile data set was divided by the tendon cross-sectional area, to create a 'stress' column. To calculate strain, the column for 'crosshead distance' was divided by the initial sample inter-grip length. The value used for inter-grip length was measured with ImageJ, using a video frame when the tendon was in tension, prior to preconditioning. Finally, a stress vs. strain curve for each tensile test was plotted (Figure 5.2).

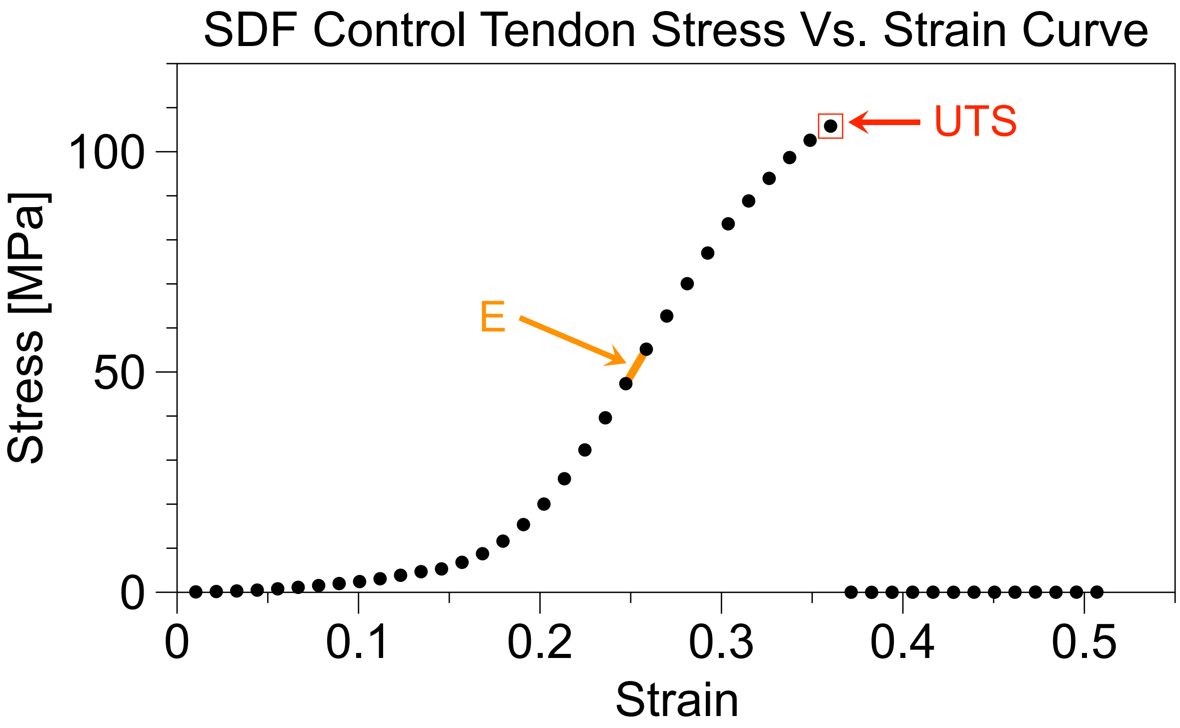

Figure 5.2: This figure shows the stress-strain curve of a SDF control tendon. The modulus, E, was calculated as the segment of the stress-strain curve with maximum slope. The red boxed point labelled UTS, at a value of 105.8 MPa is the ultimate tensile strength. The immediate drop in stress from the UTS to zero is indicative of a complete instantaneous tendon rupture.

The UTS of each tendon was determined as the maximum tensile stress recorded, prior to failure, as labelled in Figure 5.2. Two methods were used to determine E, and the results from each were compared. In the first method, the derivative of the linear equation between subsequent points, in the portion of the stress-strain curve prior to rupture, was used to determine which segment of the linear region of the stress-strain curve had the largest slope, which was taken as E (Figure 5.3). For the second method, the points indicating the start and end of the stress-strain curve's linear region were qualitatively determined and the slope of the line connecting these points was taken as E. Using both methods, the results were comparable, so the first method was used for the presentation of results, as it was the most repeatable.

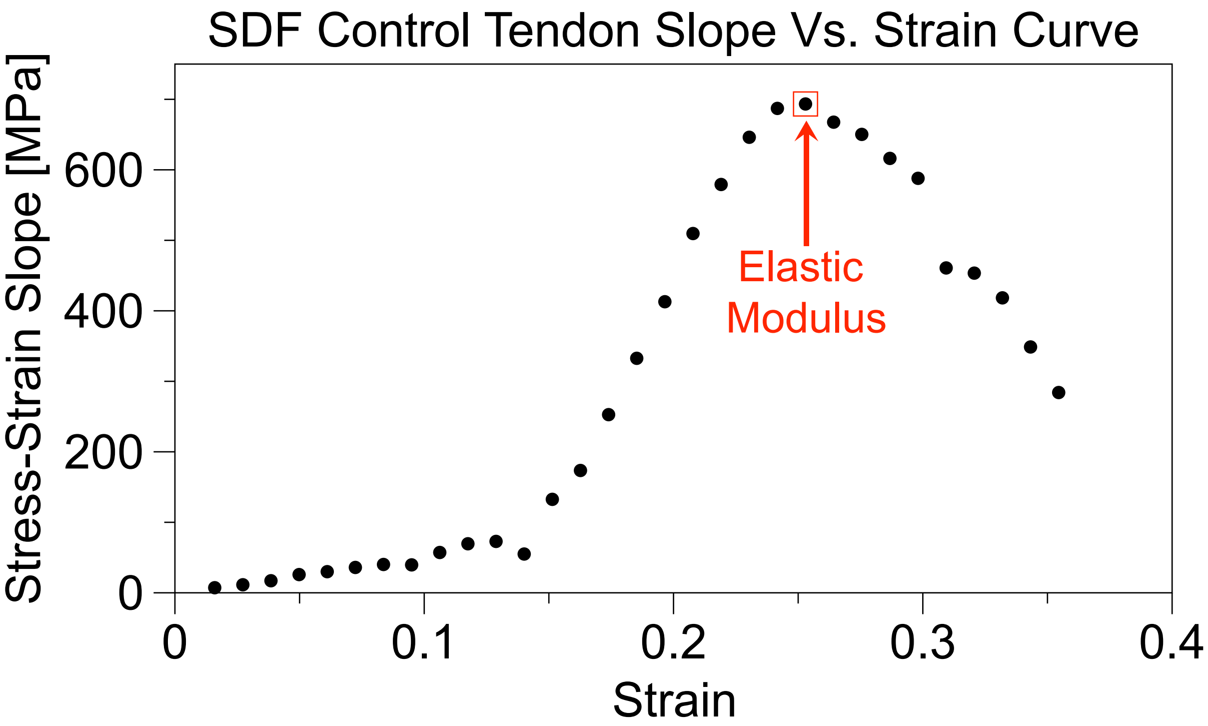

Figure 5.3: A plot of the slope of the line between each two points of the stress-strain curve vs. strain, for the segment of the curve prior to rupture in a SDF test tendon. The maximum value of this curve shows the maximum slope between two points in the linear region of the stress-strain curve.

Statistical Analysis

Statistical analysis was conducted using JMP (Version 17.1.0, SAS Institute, USA). The UTS data were analyzed by splitting the data by treatment and conducting a one-way repeated measures ANOVA, with treatment as the repeated measure and tendon type as the independent factor. After finding treatment to be the only significant factor, tendon types were pooled together and a matched-pair two-tailed t-test was performed. For the modulus of elasticity data, the same statistical approach was repeated. The data was split by treatment and a one-way repeated measures ANOVA was conducted, with treatment as the repeated measure and tendon type as the independent factor. Tendon type was found to be the only significant factor, so test and control samples were combined, and a pooled two-tailed t-test was run on the modulus by tendon type.

5.4 Results

Tested samples showed no evidence of slippage within the grips, and failure occurred within the mid-substance of the inter-grip region and not directly at the grips. Failure was often accompanied by one crisp, audible crack or multiple cracks of lesser volume. A significant difference was found between the UTS of the test and control groups using a one-way repeated measures ANOVA ($p = 0.0292$), as seen in Figure 5.4, but no difference was found between CDE and SDF tendons ($p = 0.1330$). Further, the interaction of treatment and tendon type was not significant ($p = 0.3281$), as seen in Figure 5.5. A one-way ANOVA of the modulus data had a different result, finding only tendon type to be significant ($p = 0.0072$) but not treatment ($p = 0.2492$) or their interaction ($p = 0.2407$), shown in Figure 5.6. When test and control data were pooled, CDE tendons had a significantly higher modulus of elasticity than SDF tendons ($p = 0.0030$), coinciding with the literature[56], as shown in Figure 5.7.

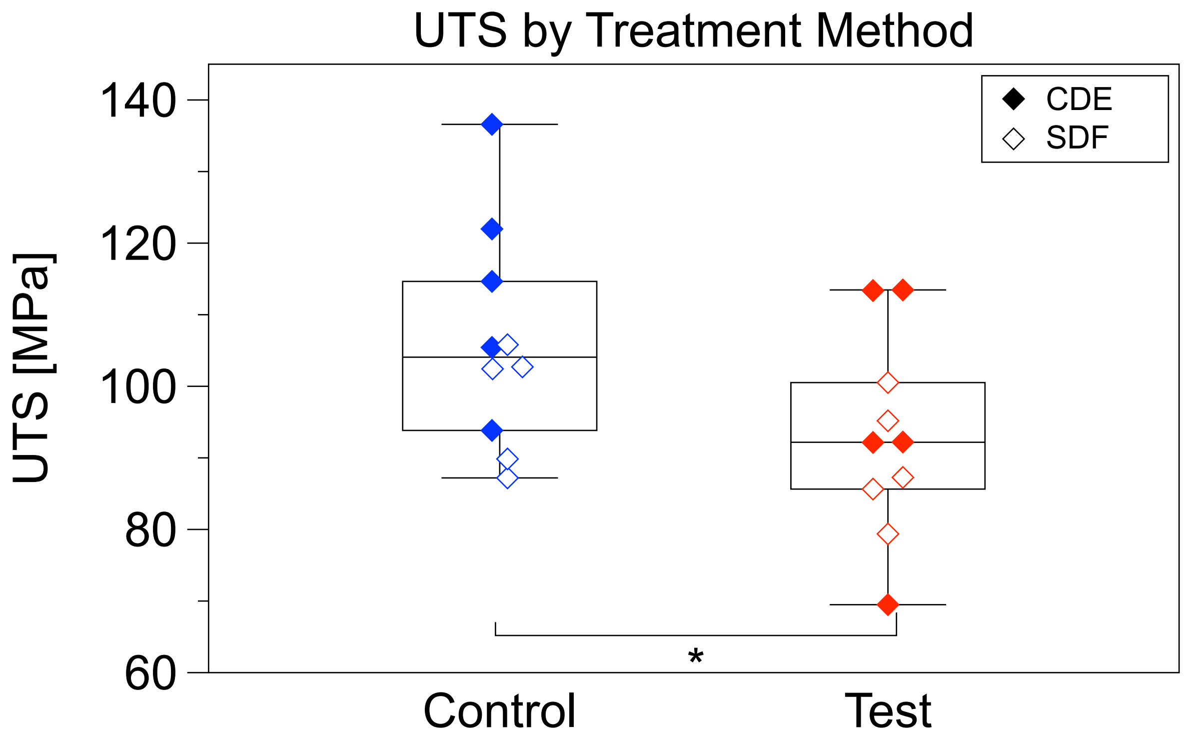

Figure 5.4: Plot showing the UTS of Control (106.0 ± 15.1 [MPa]) vs. test (92.9 ± 13.8 [MPa]) tendons. Test tendons had significantly decreased UTS compared to controls (p = 0.0270).

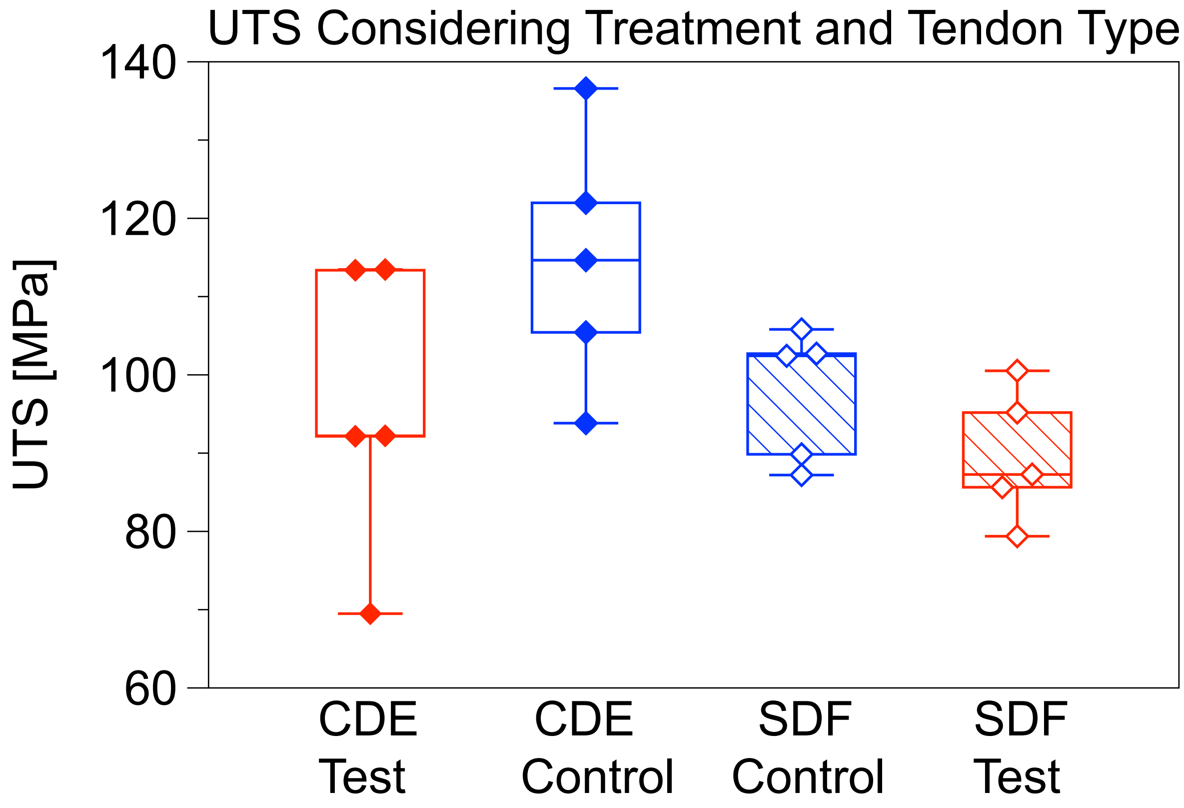

Figure 5.5: Plot showing the UTS of the four sample groups. The factor of treatment (test vs. control) was significant (*p* = 0.0292), while tendon type was not (*p* = 0.1330).

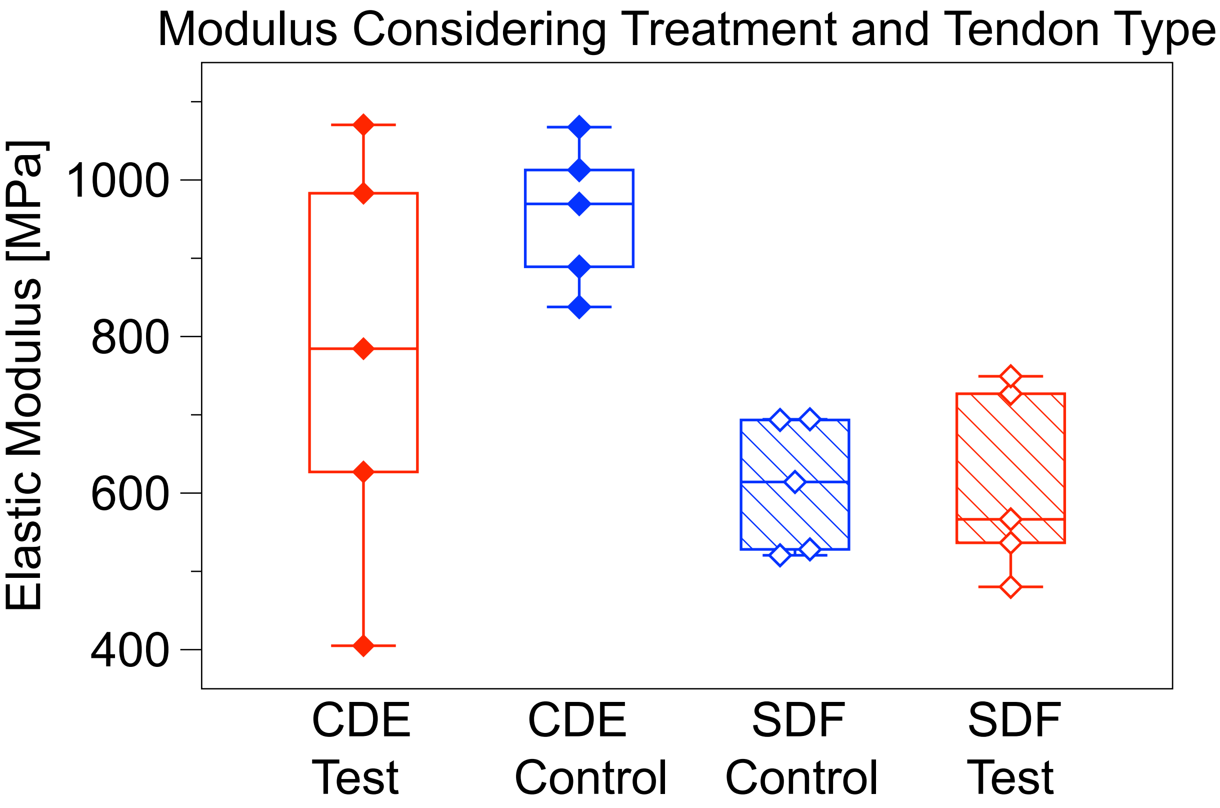

Figure 5.6: Plot showing the elastic modulus of the four sample groups. The factor of tendon type was significant (*p* = 0.0072), while the factor of treatment (test vs. control) was not (*p* = 0.2492).

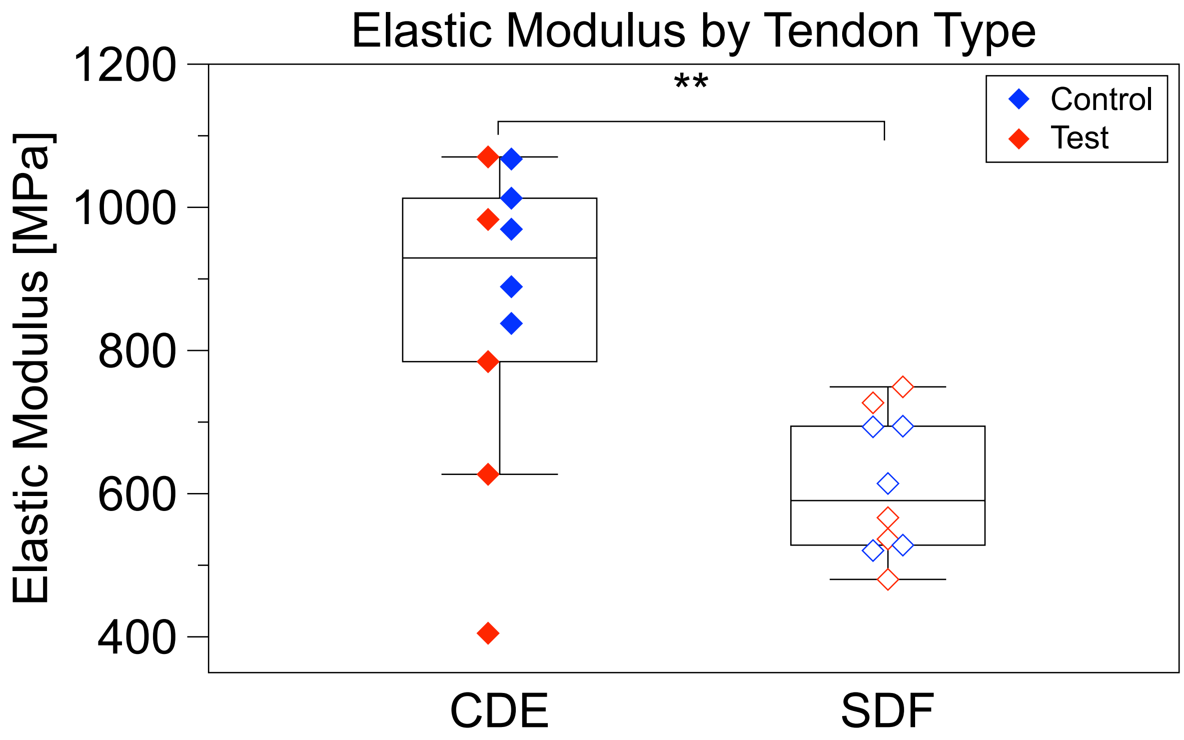

Figure 5.7: Plot showing the elastic modulus of CDE (864.7 ± 212.4 [MPa]) vs. SDF (611.0 ± 97.7 [MPa]) tendons. CDE tendons show a significantly higher elastic modulus ($p = 0.0030$).

5.5 Discussion

Consistent with hypothesis (xv), the UTS of control tendons was greater than that of cyclically buckled tendons. The process leading to tensile failure began with the initiation of damage, followed by damage propagation, until a macroscale failure occurred. As structural damage was observed through cyclic buckling in Chapter 4, evidence is present that test tendons contain locations where damage was already initiated, indicating the tensile failure process had commenced prior to the application of a tensile force. As such, there were likely sites of reduced tensile load-bearing ability, and hence stress-concentration and early failure.

The unexpected result, pertaining to UTS, is that significance was not found between the CDE and SDF tendon, nor between the interaction of the two factors (treatment and tendon type). The study of mechanical properties, such as UTS, on large animal models in the literature is well established, always indicating a superior strength of CDE tendons, relative to SDF tendons, or the same result in analogous tendons[17,52,54–56]. An insignificant result between the tendon types without considering treatment makes some sense, as it is not a comparison of the two tendons under the same conditions. However, to support the literature, a difference between tendon types among control samples would be required. Despite the ANOVA result preventing further statistical analyses, it was observed that the control CDE tendon UTS (114.5 ± 16.2 [MPa]) was larger than that of the control SDF tendon (97.6 ± 8.4 [MPa]). It is important to note that the small sample size of each group (n=5) resulted in the presence of large standard deviations in the data, especially in the CDE tendons. To determine if a larger sample size would lead to a significant result, the statistical analysis for UTS by tendon type was run again, assuming one additional sample was present in each group (n=6) where the UTS for the additional sample was that of the mean. It was determined that in this scenario with a sample size of n=6, a significant difference would be present between tendon types ($p = 0.0370$).

The other comparisons within the interaction term that were of interest were the differences between the CDE test and control, and the SDF test and control tendons. Again, there is an indication that the differences in these two measurements are not significant, albeit, the means of the CDE tendon test (96.1 ± 18.3 [MPa]) and control (114.5 ± 16.2 [MPa]), as well as the SDF tendon test (89.6 ± 8.3 [MPa]) and control (97.6 ± 8.4 [MPa]), show a larger UTS in each control compared to the match-paired test, suggesting that the significant difference between test and control is impacted by both tendon types. This is a very good result for the ‘CUE’ model, as it shows that the UTS of energy-storing tendons are just as affected as positional tendons, following cyclic buckling. This result is also consistent with the fluorescence microscopy, PLM and some of the SHG microscopy findings, presented in Chapter 4, that both tendon types are equally affected by cyclic buckling.

There are also a combination of expected and unexpected results pertaining to the elastic modulus. Interestingly, a significant result was not found considering cyclic buckling, though significance was found between tendon type, which was opposite of the UTS results. The CDE tendons (864.7 ± 212.4 [MPa]) had a significantly larger modulus than the SDF tendons (611.0 ± 97.7 [MPa]). The CDE tendon test (774.0 ± 269.0 [MPa]) and control (955.3 ± 92.6 [MPa]) values both being larger than the SDF tendon test (611.9 ± 119.6 [MPa]) and control (610.1 ± 84.8 [MPa]) moduli indicates that both the test and control contribute to this result.

To better understand why cyclic buckling affected UTS but not elastic modulus, the results of Chapter 4 may be revisited. Through structural analysis, it was determined that testing damage was presented as small, highly concentrated regions, dispersed throughout the tissue. Under sub-failure loading, the microscopic defect sites could be expected to carry less load, and consequently the surrounding tissue would be under higher stresses, resulting in the tissue under high stresses experiencing greater strain. This would not appear as a change in modulus of the bulk material, as the larger strains would only be present at the very longitudinally limited sites where the damage was present. Further, this extra extension would be negligible, relative to the length of the entire segment of tendon clamped in the tensile grips (clamped tendon samples were an average of 18.2 mm long and localized damaged was typically on the magnitude of 1 μm). However, the locations of concentrated damage provided sites where failure would occur at a lower load, and the stress concentration would mean that failure also propagates to adjacent material at a lower load. This would effectively result in localized damage having a great impact on the UTS than the elastic modulus.

While the results for elastic modulus and UTS in this thesis are larger than the previous works considering ovine tendons (approximate modulus: SDF tendon (120 MPa), medial extensor tendon (270 MPa), UTS: SDF tendon (31 MPa), medical extensor tendon (48 MPa))[56], this was the only study found that reported these specific mechanical properties, leaving uncertainty in their reliability. The mechanical properties obtained in this thesis are also much closer to the other large animal models[17,52,54,55], than the previous ovine study was to other large animals, suggesting that these results are likely more indicative of the true mechanical properties of ovine forelimb positional and energy-storing tendons. Most importantly, the trend of positional tendons having a larger modulus and UTS than energy-storing tendons was found, agreeing with all literature, which in combination with the numerical values observed, suggests that these results are reliable.

5.6 Conclusions

Hypothesis (xiv): CDE tendons will have a larger ultimate tensile strength and modulus of elasticity (E) than SDF tendons.

Hypothesis (xiv) Result: This hypothesis was partially confirmed. It was confirmed that the elastic modulus of CDE was greater than SDF tendons, though it was not confirmed that the UTS of CDE was greater than SDF tendons. However, this hypothesis should not be rejected, as it was determined that by increasing the sample size by 1, a significantly larger UTS would be observed in CDE tendons.

Hypothesis (xv): Cyclic buckling of tendons will result in decreased values for UTS and E, relative to the controls.

Hypothesis (xv) Result: The first part of this hypothesis was confirmed that cyclic buckling did cause a decrease in tendon UTS. The second part was rejected, as cyclic buckling did not cause a decrease in elastic modulus, under the conditions of this thesis, though that is not to say that cyclic buckling is incapable of causing changes to elastic modulus.

Hypothesis (xvi): Cyclic buckling will have a more severe effect on the UTS and E in the positional CDE tendon, than the energy-storing SDF tendon.

Hypothesis (xvi) Result: This hypothesis was rejected, as testing did not have an effect on modulus and testing was observed to have an equal effect on the UTS of both positional and energy-storing tendons.

A tensile pull to rupture following cyclic buckling showed that independent of tendon type, cyclically buckled tendons have a significantly lower UTS than an ex vivo control. Further, independent of treatment, CDE tendons displayed a greater modulus of elasticity than SDF tendons. The resulting mechanical property values obtained are comparable to the literature of other large animal models and are much closer than the only other known study mentioning ovine mechanical properties. However, the sample size (n=20 total tendons, 5 per treatment-tendon type combination) was relatively small and increasing it would reduce standard deviations and increase significance of some results that failed to reach significance.

Chapter 6: Summary and Conclusions

6.1 Structure – Function Relationship

The relationship between structure and function in tendons is difficult to understand due to its complexity. However, an understanding is necessary to optimize the treatment of tendinopathies.

In this thesis, cyclically buckling tendons caused changes at several hierarchical levels, observed through fluorescence microscopy, SHG microscopy and PLM. Fluorescence microscopy, conducted after staining tissue sections with a CHP solution, illustrated the increase in denatured tissue present in cyclically buckled tissue. The denatured tissue was not localized along kinkbands and was not significantly affected by tendon type.

PLM images added to the fluorescence microscopy results, showing that kinkband density was found to increase because of cyclic buckling, with equal ease in both positional and energy-storing tendons.

Utilizing SHG microscopy, structural differences were shown between tendon types through the observation of a smaller ρ value in positional (1.14 ± 0.02), relative to energy-storing (1.21 ± 0.05) tendons, a result that before this thesis had never been reported. SHG microscopy also displayed an increase in structural disorder in both cyclically buckled tendon types, as well as along the axis of kinking in kinkbands.

The combination of these three imaging techniques demonstrated that cyclic buckling of tendons causes structural changes from the nanoscale to the microscale, regardless of tendon type. To best explain these changes and the resulting kinkbands formed through cyclic buckling, a descriptive model was created. The kinkband formation model 'KFM' was presented, describing the structural changes leading to the formation of a kinkband due to cyclic buckling, as a supplemental model to the 'CUE' model, proposed by Herod et al.[95].

Structure has a direct effect on function, so the resulting effects of cyclic buckling on the mechanical properties of tendon were explored. It was determined that cyclic buckling caused a significant decrease in the UTS of tendon but did not significantly affect the tendon modulus of elasticity. The tensile testing results also strengthened the literary values for modulus, showing the modulus of positional tendons to be greater than energy-storing tendons. An important result was also that the observed mechanical properties of ovine tendons were comparable to those of other large animal models, as opposed to the smaller values previously making up the literature.

6.2 Research Objective Conclusions

In Chapter 2.2 four objectives were proposed to guide this thesis.

Objective (i): To investigate the effect of cyclic buckling on the molecular and nanoscale structure of ovine tendons.

Objective (i) Result: Three imaging techniques were utilized to undergo a detailed investigation on the molecular and nanoscale structural changes caused by cyclic buckling. These imaging techniques helped to understand how structural changes may present themselves and led to the creation of a model proposing how these changes may occur.

Objective (ii): To assess the relative structural impact of cyclic buckling between the positional CDE and energy-storing SDF tendon.

Objective (ii) Result: Differences between tendon types were assessed using one positional and one energy-storing tendon, though no significant differences were observed.

Objective (iii): To investigate the effect of cyclic buckling on the mechanical properties of ovine tendon.

Objective (iii) Result: Following buckling, a tensile pull to rupture test determined changes, when present, in mechanical properties of ovine tendons.

Objective (iv): To assess the relative mechanical response to cyclic buckling between the positional CDE and energy-storing SDF tendon.

Objective (iv) Result: Tensile testing was utilized to show that cyclic buckling of tendons did not affect one tendon type more than the other.

6.3 Limitations

6.3.1 Sample Acquisition and Storage

No members of the Veres laboratory were present during the time of slaughter, leaving some uncertainty in the time between slaughter and the time when the samples were collected. However, all samples were collected from the same abattoir, where slaughter occurred between 7:00 am and 11:00 am, and samples were collected and brought back to SMU no later than 1:00 pm (depending on the time they were ready that day). Some studies have expressed concerns regarding the relationship between time of slaughter and the circadian rhythm of tendon. In these studies, they typically concatenate the morning hours into one group[165,166], meaning this would likely not pose an issue to the present work, as all animals were slaughtered in the morning.

Though an estimate of age was provided, the exact age of each animal was not always known, nor were the prior living conditions of the animal, such as exercise level. Information regarding activity level was not expected, as it is rarely provided in the literature. Albeit for a study where tendons are mechanically tested, additional information would be useful, since tendons of older animals and tendons experiencing more lifetime loading would be more susceptible to damage prior to dissection. This was controlled for by using a matched pair from the contralateral forelimb of each animal.

The storage of tendons was another limitation. The time required to transport tendons from the abattoir to Saint Mary's University, dissect, and then freeze them typically took approximately

75-115 minutes, though they were kept in a cooler during this period. Tendons would ideally be tested fresh, to give the most accurate representation of their mechanics, though this was not possible. Research on the storage of tendons has shown that three main factors contribute to the preservation of tendon structure and function, those being temperature, duration, and freeze-thaw cycles. Storage of tendons at -80 °C have produced the largest values of UTS and elastic modulus, with mechanical property values decreasing as storage temperature decreases. It is suspected that storage at warmer temperatures can increase damage from ice crystals, changing the structure, and consequently, tendon properties[167,168], though it remains unclear the ideal storage temperature. Different studies have shown differing results surrounding the effect of storage duration. A study by Ng et al.[169] found that when storing tendons at -40 °C, the UTS and modulus increased over the first 170 days and then decreased following, with the values at 1 year still exceeding those at 0 days. A study by Quirk et al.[170] investigated freezing at -80 °C for 9 months versus fresh tendons and found that the UTS significantly decreased, while modulus did not. Finally, most research has concluded that the structure and mechanical properties of tendon remain like fresh tendons when two or less freeze/thaw cycles are performed, with changes occurring after the second freeze/thaw cycle[170–172]. The combination of storage variables clearly affects the testing outcome, so this is undoubtedly a limitation of these works, however, the – 86 °C storage for 3-5 months, with one freeze/thaw cycle used in this thesis, is consistent with the recommendations of the literature.

6.3.2 Mechanical Testing

The first limitation of the mechanical testing comes from the clamping forces exerted on samples in both the cyclic buckling and tensile testing apparatuses. All clamps were 3-D printed, so the measurement of their clamping forces would have been useful knowledge. However, no observation of tendon slippage was apparent, indicating the producible clamping force was sufficient.

When clamping tendons within the grips, it was difficult to ensure the inter-grip length was identical between tests. Despite the best efforts to ensure consistency, some variation in inter-grip length was present (18.2 ± 2.2 mm). This likely had little effect on the tensile testing and would only reduce the precision of results. For the cyclic buckling there was more of an impact, as this changed the bending radius of curvature. Additionally, samples had different thicknesses based on animal size and tendon type, which also affected the bending radius of curvature. It is unclear what effect, if any, the radius of curvature has on the accumulation of damage as tendons buckle, though this is something that would be worthwhile to study in future work.

6.3.3 Imaging

Imaged tendon sections were 5 μm thick and moved multiple times with tweezers. It is possible that the tweezers may have caused damage to the tendons in certain locations, though this did not seem to be the case, as test and control samples were handled identically.

The process of staining tendons with the CHP solution was performed as consistently as possible but the small nature of the well-plate and solution volume, where the thin and relatively fragile sections were submerged in, posed difficulties. Two pairs of tendons were removed due to suspected staining procedural complications. Complications were most likely to arise from an incomplete rinsing of excess CHP from tissue or the folding of tissue edges trapping CHP in the edges. To best respond to this issue, any fluorescence clearly present as an artifact, air bubble with trapped CHP or highly intense edges of a tissue section, were removed from the acquired image. In severe cases, such as the two pairs of tendons removed from the study, the whole tendon was discarded.

SHG PIPO scans are commonly taken of single fibrils, as the entire fibril can be imaged. The sections in this study were too large to fully capture through SHG, despite taking several scans of each section. This posed a limitation and required the selection of isolated locations to be carefully chosen to best capture the intended feature.

The methods used for drawing relationships between features of each imaging technique were effective but more concrete conclusions could be drawn if the same location of the same sample were imaged with all imaging techniques. The R-CHP excitation spectrum was heavily affected by the 515 nm wavelength laser used in the SHG microscope, meaning that throughout the approximately 15 minutes required to obtain one 64-image PIPO stack, the fluorophores would undergo excessive heating. An attempt to scan CHP-stained sections using SHG microscopy was made but this ultimately led to the burning of tissue.

A second idea to image fluorescence-stained sections through SHG was also tested. Following fluorescence microscopy, samples were photobleached. The photobleaching process was conducted using the same fluorescence microscope used for imaging. The 20x objective lens was put in place and the entire section was imaged with an exposure time of 500 ms, then subsequently imaged with an exposure time of 2000 ms. This process of 500 ms followed by 2000 ms was repeated seven times. Numerous scans with a lower exposure time, rather than one high exposure scan was preferable, to avoid burning of the tissue. The photobleached section was then imaged via SHG microscopy, within two weeks of photobleaching. This photobleaching method was effective, as seen in Figure 6.1, where the first and last scan in the SHG PIPO stack appear nearly indistinguishable, suggesting negligible evidence of burning. After fitting the acquired PIPO image, it was observed that locations of intense denaturation on the fluorescence image were presented as well fit pixels, with high intensity. A pixel containing many denatured molecules, should not produce an intense signal. This entertained the possibility that the CHP monomeric α-chains attaching to the α-chains of denatured collagen molecules was able to produce a SHG signal. The uncertainty of the resulting images forced the abandonment of this method and the proceeding of the techniques presented in Chapter 4 of this thesis.

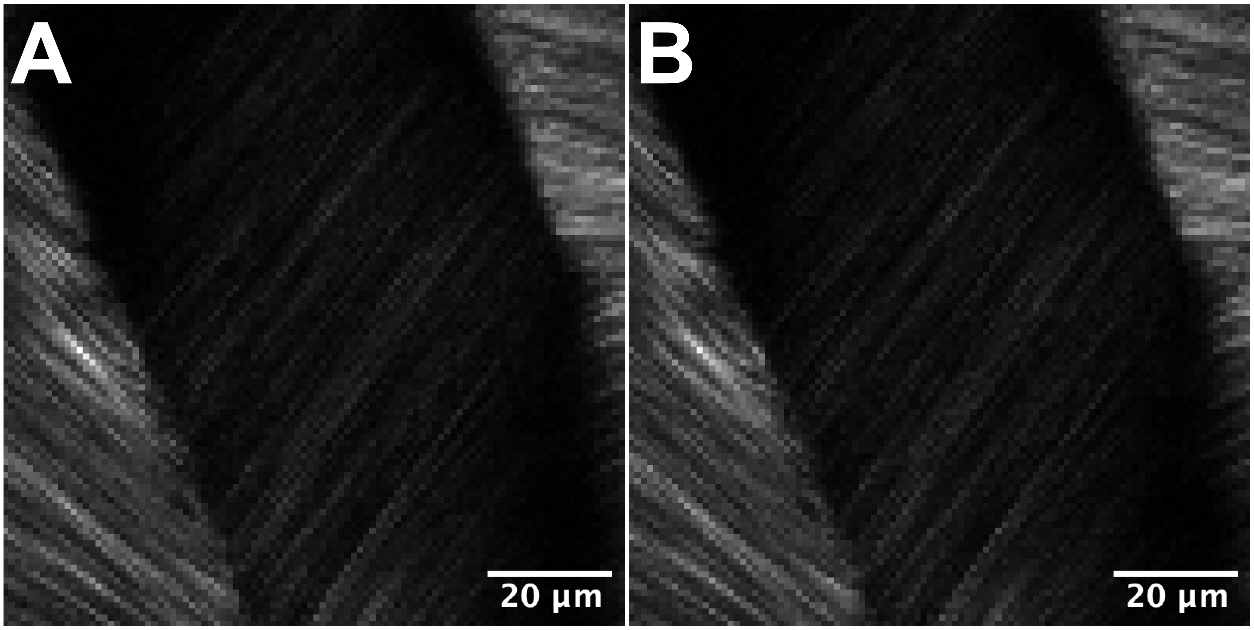

Figure 6.1: The intensity images of a CHP stained and photobleached CDE test tendon. (A) The first and (B) the last image of a 65 image PIPO stack. The two images are nearly indistinguishable, indicating negligible tissue burning occurred.

6.4 Significance

Tendinopathy is a nagging injury affecting workers, athletes, and others. Not only does tendinopathy limit the ability of those affected to return to work or sport, but current treatment, usually in the form of physiotherapy, can be very expensive, with no clear end in sight. Additionally, this chronic pathology may limit one's ability to participate in physical activities in a social setting, as a result of pain and reduced function. This places a significant physical burden on individuals, which could be subsided by improving our understanding of tendinopathy.

This thesis looked to investigate a potential mechanism responsible for the initiation of tendinopathy. Rather than testing treatment methods, the results of the current work has helped to better understand how tendinopathies may form. Understanding the root of this pathology will help to tailor new and existing treatment methods that will consider the buckling of tendons. Additionally, it will help provide clinicians with the knowledge to help victims rehabilitate, altering the movements that led to chronic tendinopathy, to relearn them in a way that will better resist future complications.

6.5 Future Work

A few potential directions for future work were inspired throughout the process of conducting the research in this thesis. Firstly, the kinkband inclusion criteria developed for confirming kinkbands should be validated through SEM. Previously, Herod et al.[95] identified kinkbands using SEM, so a comparison of kinkbands between the PLM identification in this thesis and its predecessor would strengthen findings. Two potential methods for completing this task would be to bisect a tendon, using one half for SEM and taking the first section from the open bisected face of the other half and imaging it under PLM. A second potential and more conclusive method would be to take sections of a tendon for PLM and after imaging the tissue under PLM, prepare the section for SEM, to investigate the same feature under both microscopies.

Based on the observation of kinkbanding through SHG microscopy and the absence of fit pixels along kinkbands, an investigation of the reason behind the inability to fit may help further explain how kinkbands form. This could be done by imaging kinkbands using another non-linear microscopy, such as Rayleigh scattering.

To determine the locations of a buckled tendon where kinkbands are most susceptible to form a similar project could be carried out. Cross-sections of a buckled tendon at the bottom of the buckle, using the tendon orientation of Figure 3.6, experience greater localized stresses than cross-sections at the top. However, bisecting the tendon in the frontal plane about its longitudinal axis, half of the tendon should have a similar structure. If the tendon were bisected following cyclic buckling, sections could be imaged at various heights of a tendon using different microscopies to investigate how varying locations of a tendon may be more susceptible to kinkbanding.

A logical next step, having determined the ability of cyclic buckling to form kinkbands, would be to look at how the addition of a tensile component changes the tendon structure. Various parameters may be considered here, such as the rate of loading, the amount of strain, and degree of buckling incorporated in each cycle. A specific feature that should be considered when adding a tensile component to each cycle is the denaturation of molecules along a kinkband. Denaturation was not observed along kinkbands in this thesis, however, the stretching of tendon as kinkbands form may display a different presentation of the kinkband.

Bibliography

1. Klaus-Dieter, Habel RE. 2003. Bovine Anatomy, First. Germany: Die Deutsche Bibliothek.

2. Vipula Ms, Atula Ms. 2018. Human Anatomy and Physiology: For Undergraduate Students of Pharmacy, Nursing, Physiotherapy and Other Paramedical Sciences. In: First, editor. . Bengaluru : Laxmi Publications Pvt Ltd. 2018. p 229–230.

3. Munford MJ, Ng KCG, Jeffers JRT. 2020. Mapping the Multi-Directional Mechanical Properties of Bone in the Proximal Tibia. Adv. Funct. Mater. 30(46).

4. HURLEY MV, REES J, NEWHAM DJ. 1998. Quadriceps function, proprioceptive acuity and functional performance in healthy young, middle-aged and elderly subjects. Age Ageing 27(1):55–62.

5. Zitnay JL, Weiss JA. 2018. Load transfer, damage, and failure in ligaments and tendons. J Orthop Res 36(12):3093–3104.

6. Ker RF. 2007. Mechanics of tendon, from an engineering perspective. Int J Fatigue 29(6):1001–1009.

7. Collier TA, Nash A, Birch HL, Leeuw NH de. 2018. Effect on the mechanical properties of type I collagen of intra-molecular lysine-arginine derived advanced glycation end-product cross-linking. J Biomech 67:55–61.

8. Thorpe CT, Peffers MJ, Simpson D, et al. 2016. Anatomical heterogeneity of tendon: Fascicular and interfascicular tendon compartments have distinct proteomic composition. Sci Rep-uk 6(1):20455.

9. Handsfield GG, Slane LC, Screen HRC. 2016. Nomenclature of the tendon hierarchy: An overview of inconsistent terminology and a proposed size-based naming scheme with terminology for multi-muscle tendons. J Biomech 49(13):3122–3124.

10. Kastelic J, Galeski A, Baer E. 1978. The Multicomposite Structure of Tendon. Connect. Tissue Res. 6(1):11–23.

11. SCREEN HRC. 2009. Hierarchical Approaches to Understanding Tendon Mechanics. J Biomechanical Sci Eng 4(4):481–499.

12. Veres SP, Lee JM. 2012. Designed to Fail: A Novel Mode of Collagen Fibril Disruption and Its Relevance to Tissue Toughness. Biophys J 102(12):2876–2884.

13. Screen HRC, Bader DL, Lee DA, Shelton JC. 2004. Local Strain Measurement within Tendon. Strain 40(4):157–163.

14. BATSON EL, PARAMOUR RJ, SMITH TJ, et al. 2003. Are the material properties and matrix composition of equine flexor and extensor tendons determined by their functions? Equine Vet J 35(3):314–318.

15. Alexander RM. 1991. Energy-saving mechanisms in walking and running. J Exp Biol 160(1):55–69.

16. Biewener AA. 1998. Muscle-tendon stresses and elastic energy storage during locomotion in the horse. Comp Biochem Physiology Part B Biochem Mol Biology 120(1):73–87.

17. Thorpe CT, Udeze CP, Birch HL, et al. 2012. Specialization of tendon mechanical properties results from interfascicular differences. J Roy Soc Interface 9(76):3108–3117.

18. Quigley AS, Bancelin S, Deska-Gauthier D, et al. 2018. In tendons, differing physiological requirements lead to functionally distinct nanostructures. Sci Rep-uk 8(1):4409.

19. Fang F, Lake SP. 2017. Experimental evaluation of multiscale tendon mechanics. J Orthopaed Res 35(7):1353–1365.

20. Harvey M, Cisek R, Tokarz D, Kreplak L. 2023. Effect of out of plane orientation on polarization second harmonic generation of single collagen fibrils. Biomed. Opt. Express 14(12):6271.

21. Shoulders MD, Raines RT. 2009. Collagen Structure and Stability. Annu Rev Biochem 78(1):929–958.

22. Buehler MJ. 2006. Nature designs tough collagen: Explaining the nanostructure of collagen fibrils. Proc. Natl. Acad. Sci. 103(33):12285–12290.

23. Gelse K, Pöschl E, Aigner T. 2003. Collagens—structure, function, and biosynthesis. Adv Drug Deliver Rev 55(12):1531–1546.

24. Hodge AJ, Schmitt FO. 1960. THE CHARGE PROFILE OF THE TROPOCOLLAGEN MACROMOLECULE AND THE PACKING ARRANGEMENT IN NATIVE-TYPE COLLAGEN FIBRILS*. Proc National Acad Sci 46(2):186–197.

25. Exposito J-Y, Valcourt U, Cluzel C, Lethias C. 2010. The Fibrillar Collagen Family. Int J Mol Sci 11(2):407–426.

26. Eyre DR, Wu J-J. 2005. Collagen, Primer in Structure, Processing and Assembly. Top Curr Chem :207–229.

27. Svensson RB, Herchenhan A, Starborg T, et al. 2017. Evidence of structurally continuous collagen fibrils in tendons. Acta Biomater 50:293–301.

28. Peterson BE, Szczesny SE. 2020. Dependence of tendon multiscale mechanics on sample gauge length is consistent with discontinuous collagen fibrils. Acta Biomater 117:302–309.

29. Lee AM. 2023. Benchmarking Native Collagen: Evaluation of Structural Differences between Tendon Types and across Animal Models.

30. Herod TW, Chambers NC, Veres SP. 2016. Collagen fibrils in functionally distinct tendons have differing structural responses to tendon rupture and fatigue loading. Acta Biomater 42:296–307.

31. Birch HL. 2007. Tendon matrix composition and turnover in relation to functional requirements. Int. J. Exp. Pathol. 88(4):241–248.

32. Rumian AP, Wallace AL, Birch HL. 2007. Tendons and ligaments are anatomically distinct but overlap in molecular and morphological features—a comparative study in an ovine model. J Orthopaed Res 25(4):458–464.

33. Makhzoomi AKA, Kirk TB, Allison GT. 2021. An AFM study of the nanostructural response of New Zealand white rabbit Achilles tendons to cyclic loading. Microscopy Research & Technique Available from: https://analyticalsciencejournals-onlinelibrary-wiley-com.library.smu.ca/doi/epdf/10.1002/jemt.23944.

34. Dittmore A, Silver J, Sarkar SK, et al. 2016. Internal strain drives spontaneous periodic buckling in collagen and regulates remodeling. Proc. Natl. Acad. Sci. 113(30):8436–8441.

35. Orgel JPRO, Irving TC, Miller A, Wess TJ. 2006. Microfibrillar structure of type I collagen in situ. Proc National Acad Sci 103(24):9001–9005.

36. Kalson NS, Lu Y, Taylor SH, et al. 2015. A structure-based extracellular matrix expansion mechanism of fibrous tissue growth. Elife 4:e05958.

37. Grant TM, Thompson MS, Urban J, Yu J. 2013. Elastic fibres are broadly distributed in tendon and highly localized around tenocytes. J. Anat. 222(6):573–579.

38. Dael WC, Baer E. 1974. Fibre-buckling in composite systems: a model for the ultrastructure of uncalcified collagen tissues. Composites 9(3):369–382.

39. Wilmink J, Wilson AM, Goodship AE. 1992. Functional significance of the morphology and micromechanics of collagen fibres in relation to partial rupture of the superficial digital flexor tendon in racehorses. Res. Vet. Sci. 53(3):354–359.

40. Shearer T, Thorpe CT, Screen HRC. 2017. The relative compliance of energy-storing tendons may be due to the helical fibril arrangement of their fascicles. J Roy Soc Interface 14(133):20170261.

41. Järvinen TAH, Järvinen TLN, Kannus P, et al. 2004. Collagen fibres of the spontaneously ruptured human tendons display decreased thickness and crimp angle. J. Orthop. Res. 22(6):1303–1309.

42. Thorpe CT, Riley GP, Birch HL, et al. 2016. Fascicles and the interfascicular matrix show adaptation for fatigue resistance in energy storing tendons. Acta Biomater 42:308–315.

43. Thorpe CT, Godinho MSC, Riley GP, et al. 2015. The interfascicular matrix enables fascicle sliding and recovery in tendon, and behaves more elastically in energy storing tendons. J Mech Behav Biomed 52:85–94.

44. Godinho MSC, Thorpe CT, Greenwald SE, Screen HRC. 2017. Elastin is Localised to the Interfascicular Matrix of Energy Storing Tendons and Becomes Increasingly Disorganised With Ageing. Sci Rep-uk 7(1):9713.

45. Thorpe CT, Karunaseelan KJ, Hin JNC, et al. 2016. Distribution of proteins within different compartments of tendon varies according to tendon type. J Anat 229(3):450–458.

46. Thorpe CT, Birch HL, Clegg PD, Screen HRC. 2013. The role of the non-collagenous matrix in tendon function. Int. J. Exp. Pathol. 94(4):248–259.

47. Thorpe CT, Streeter I, Pinchbeck GL, et al. 2010. Aspartic Acid Racemization and Collagen Degradation Markers Reveal an Accumulation of Damage in Tendon Collagen That Is Enhanced with Aging*. J. Biol. Chem. 285(21):15674–15681.

48. Veld PJ in't, Stevens MJ. 2008. Simulation of the Mechanical Strength of a Single Collagen Molecule. Biophys. J. 95(1):33–39.

49. Sasaki N, Odajima S. 1996. Stress-strain curve and young's modulus of a collagen molecule as determined by the X-ray diffraction technique. J. Biomech. 29(5):655–658.

50. Liu Y, Ballarini R, Eppell SJ. 2016. Tension tests on mammalian collagen fibrils. Interface Focus 6(1):20150080.

51. Svensson RB, Mulder H, Kovanen V, Magnusson SP. 2013. Fracture Mechanics of Collagen Fibrils: Influence of Natural Cross-Links. Biophys. J. 104(11):2476–2484.

52. UK I of B School of Engineering and Materials Science, Queen Mary, University of London, Mile End Road, London, E1 4NS, Thorpe C, Udeze C, et al. 2013. Capacity for sliding between tendon fascicles decreases with ageing in injury prone equine tendons: a possible mechanism for age-related tendinopathy? European Cells Mater 25:48–60.

53. Wren TAL, Lindsey DP, Beaupré GS, Carter DR. 2003. Effects of Creep and Cyclic Loading on the Mechanical Properties and Failure of Human Achilles Tendons. Ann Biomed Eng 31(6):710–717.

54. Verkade ME, Back W, Birch HL. 2020. Equine digital tendons show breed-specific differences in their mechanical properties that may relate to athletic ability and predisposition to injury. Equine Vet J 52(2):320–325.

55. Chambers NC, Herod TW, Veres SP. 2018. Ultrastructure of tendon rupture depends on strain rate and tendon type. J Orthop Res 36(11):2842–2850.

56. Choi RK, Smith MM, Smith S, et al. 2019. Functionally distinct tendons have different biomechanical, biochemical and histological responses to in vitro unloading. J Biomech 95:109321.

57. Shojaee A. 2023. Equine tendon mechanical behaviour: Prospects for repair and regeneration applications. Vet. Med. Sci. 9(5):2053–2069.

58. Wren TAL, Yerby SA, Beaupré GS, Carter DR. 2001. Mechanical properties of the human achilles tendon. Clin. Biomech. 16(3):245–251.

59. Louis-Ugbo J, Leeson B, Hutton WC. 2004. Tensile properties of fresh human calcaneal (achilles) tendons. Clin. Anat. 17(1):30–35.

60. Kongsgaard M, Qvortrup K, Larsen J, et al. 2010. Fibril Morphology and Tendon Mechanical Properties in Patellar Tendinopathy. Am. J. Sports Med. 38(4):749–756.

61. Duenwald SE, Vanderby R, Lakes RS. 2009. Viscoelastic Relaxation and Recovery of Tendon. Ann. Biomed. Eng. 37(6):1131–1140.

62. Machiraju C, Phan A-V, Pearsall AW, Madanagopal S. 2006. Viscoelastic studies of human subscapularis tendon: Relaxation test and a Wiechert model. Comput. Methods Programs Biomed. 83(1):29–33.

63. Silver FH, Ebrahimi A, Snowhill PB. 2002. Viscoelastic Properties of Self-Assembled Type I Collagen Fibers: Molecular Basis of Elastic and Viscous Behaviors. Connect. Tissue Res. 43(4):569–580.

64. Shen ZL, Kahn H, Ballarini R, Eppell SJ. 2011. Viscoelastic Properties of Isolated Collagen Fibrils. Biophys. J. 100(12):3008–3015.

65. Donahue TLH, Gregersen C, Hull ML, Howell SM. 2001. Comparison of Viscoelastic, Structural, and Material Properties of Double-Looped Anterior Cruciate Ligament Grafts Made From Bovine Digital Extensor and Human Hamstring Tendons. J. Biomech. Eng. 123(2):162–169.

66. Ciarletta P, Micera S, Accoto D, Dario P. 2006. A novel microstructural approach in tendon viscoelastic modelling at the fibrillar level. J. Biomech. 39(11):2034–2042.

67. Wang JH-C, Iosifidis MI, Fu FH. 2006. Biomechanical Basis for Tendinopathy. Clin Orthop Relat R 443(NA;):320–332.

68. Misof K, Rapp G, Fratzl P. 1997. A new molecular model for collagen elasticity based on synchrotron X-ray scattering evidence. Biophys. J. 72(3):1376–1381.

69. Silver FH, Freeman JW, Seehra GP. 2003. Collagen self-assembly and the development of tendon mechanical properties. J Biomech 36(10):1529–1553.

70. Orgel JPRO, Miller A, Irving TC, et al. 2001. The In Situ Supermolecular Structure of Type I Collagen. Structure 9(11):1061–1069.

71. Eyre DR, Paz MA, Gallop PM. 1984. Cross-Linking in Collagen and Elastin. Annual Reviews Inc. p 717–748.

72. Avery NC, Bailey AJ. 2008. Collagen: Structure and Mechanics, Chapter 4: Restraining Cross-Links Responsible for the Mechanical Properties of Collagen Fibers: Natural and Artificial. p 81–110.

73. Gautieri A, Redaelli A, Buehler MJ, Vesentini S. 2014. Age- and diabetes-related nonenzymatic crosslinks in collagen fibrils: Candidate amino acids involved in Advanced Glycation End-products. Matrix Biol. 34:89–95.

74. THORPE CT, STARK RJF, GOODSHIP AE, BIRCH HL. 2010. Mechanical properties of the equine superficial digital flexor tendon relate to specific collagen cross-link levels. Equine Vet J 42(s38):538–543.

75. Riley G. 2004. The pathogenesis of tendinopathy. A molecular perspective. Rheumatology 43(2):131–142.

76. Lui PP-Y, Chan L-S, Lee Y-W, et al. 2010. Sustained expression of proteoglycans and collagen type III/type I ratio in a calcified tendinopathy model. Rheumatology 49(2):231–239.

77. Khan KM, Cook JL, Bonar F, et al. 1999. Histopathology of Common Tendinopathies. Sports Med. 27(6):393–408.

78. Screen HRC, Seto J, Krauss S, et al. 2011. Extrafibrillar diffusion and intrafibrillar swelling at the nanoscale are associated with stress relaxation in the soft collagenous matrix tissue of tendons. Soft Matter 7(23):11243–11251.

79. Birch HL, Thorpe CT, Rumian AP. 2019. Specialisation of extracellular matrix for function in tendons and ligaments. Muscle Ligaments Tendons J. 03(01):12.

80. Rigozzi S, Müller R, Snedeker JG. 2010. Collagen fibril morphology and mechanical properties of the Achilles tendon in two inbred mouse strains. J. Anat. 216(6):724–731.

81. Screen HRC, Berk DE, Kadler KE, et al. 2015. Tendon Functional Extracellular Matrix. J Orthopaed Res 33(6):793–799.

82. Trębacz H, Barzycka A. 2023. Mechanical Properties and Functions of Elastin: An Overview. Biomolecules 13(3):574.

83. Lipman K, Wang C, Ting K, et al. 2018. Tendinopathy: injury, repair, and current exploration. Drug Des Dev Ther 12:591–603.

84. Maffulli N, Khan KM, Puddu G. 1998. Overuse tendon conditions: Time to change a confusing terminology. Arthrosc.: J. Arthrosc. Relat. Surg. 14(8):840–843.

85. Puddu G, Ippolito E, Postacchini F. 1976. A classification of achilles tendon disease. Am. J. Sports Med. 4(4):145–150.

86. Docheva D, Müller SA, Majewski M, Evans CH. 2015. Biologics for tendon repair. Adv. Drug Deliv. Rev. 84:222–239.

87. Fu S-C, Rolf C, Cheuk Y-C, et al. 2010. Deciphering the pathogenesis of tendinopathy: a three-stages process. Sports Medicine Arthrosc Rehabilitation Ther Technology Smartt 2(1):30–30.

88. Shepherd JH, Screen HRC. 2013. Fatigue loading of tendon. Int J Exp Pathol 94(4):260–270.

89. Dean BJF, Dakin SG, Millar NL, Carr AJ. 2017. Review: Emerging concepts in the pathogenesis of tendinopathy. Surg 15(6):349–354.

90. Warden SJ. 2007. Animal models for the study of tendinopathy. Brit J Sport Med 41(4):232.

91. Wezenbeek E, Willems T, Mahieu N, et al. 2018. The Role of the Vascular and Structural Response to Activity in the Development of Achilles Tendinopathy: A Prospective Study. Am J Sports Medicine 46(4):947–954.

92. 2016. Metabolic Influences on Risk for Tendon Disorders. Adv Exp Med Biol .

93. Arnoczky SP, Lavagnino M, Egerbacher M. 2007. The mechanobiological aetiopathogenesis of tendinopathy: is it the over-stimulation or the under-stimulation of tendon cells? Int J Exp Pathol 88(4):217–226.

94. Egerbacher M, Arnoczky SP, Caballero O, et al. 2008. Loss of Homeostatic Tension Induces Apoptosis in Tendon Cells: An In Vitro Study. Clin Orthop Relat R 466(7):1562.

95. Herod TW, Veres SP. 2018. Development of overuse tendinopathy: A new descriptive model for the initiation of tendon damage during cyclic loading. J Orthop Res 36(1):467–476.

96. Cook JL, Purdam CR. 2009. Is tendon pathology a continuum? A pathology model to explain the clinical presentation of load-induced tendinopathy. Brit J Sport Med 43(6):409.

97. Clinic C. 2022. Tendinopathy: Symptoms, Causes & Treatment. [cited 2023 Apr 6] Available from: https://my.clevelandclinic.org/health/diseases/22289-tendinopathy.

98. Zamboulis DE, Thorpe CT, Birch HL, et al. 2018. Pre- and post-natal development of the tendon inter-fascicular matrix and fascicles in the equine superficial digital flexor tendon and common digital extensor tendon. Osteoarthr Cartilage 26:S403–S404.

99. Makhzoomi AKA, Kirk TB, Allison GT. 2021. A multiscale study of morphological changes in tendons following repeated cyclic loading. J Biomech 128:110790.

100. Thorpe CT, Riley GP, Birch HL, et al. 2013. Fascicles from energy-storing tendons show an age-specific response to cyclic fatigue loading. Journal of the Royal Society Interface Available from: https://royalsocietypublishing.org/doi/pdf/10.1098/rsif.2013.1058.

101. Veres SP, Harrison JM, Lee JM. 2013. Repeated subrupture overload causes progression of nanoscaled discrete plasticity damage in tendon collagen fibrils. J Orthopaed Res 31(5):731–737.

102. Shepherd JH, Legerlotz K, Demirci T, et al. 2014. Functionally distinct tendon fascicles exhibit different creep and stress relaxation behaviour. Proc Institution Mech Eng Part H J Eng Medicine 228(1):49–59.

103. Pearson SJ, Burgess K, Onambele GNL. 2007. Creep and the in vivo assessment of human patellar tendon mechanical properties. Clin. Biomech. 22(6):712–717.

104. Lin AH, Allan AN, Zitnay JL, et al. 2020. Collagen denaturation is initiated upon tissue yield in both positional and energy-storing tendons. Acta Biomater 118:153–160.

105. Zitnay JL, Jung GS, Lin AH, et al. 2020. Accumulation of collagen molecular unfolding is the mechanism of cyclic fatigue damage and failure in collagenous tissues. Sci Adv 6(35):eaba2795.

106. Pedaprolu K, Szczesny SE. 2023. Mouse Achilles tendons exhibit collagen disorganization but minimal collagen denaturation during cyclic loading to failure. J. Biomech. 151:111545.

107. Wadee MA, Hunt GW, Peletier MA. 2004. Kink band instability in layered structures. J Mech Phys Solids 52(5):1071–1091.

108. Moran PM, Liu XH, Shih CF. 1995. Kink band formation and band broadening in fiber composites under compressive loading. Acta Metall Mater 43(8):2943–2958.

109. DeFrate LE, Nha KW, Papannagari R, et al. 2007. The biomechanical function of the patellar tendon during in-vivo weight-bearing flexion. J. Biomech. 40(8):1716–1722.

110. Slane LC, Bogaerts S, Mihejeva I, Scheys L. 2016. Evidence of patellar tendon buckling during passive knee extension. Knee 23(5):801–806.

111. Obst SJ, Heales LJ, Schrader BL, et al. 2018. Are the Mechanical or Material Properties of the Achilles and Patellar Tendons Altered in Tendinopathy? A Systematic Review with Meta-analysis. Sports Med 48(9):2179–2198.

112. Pearson SJ, Mohammed ASA, Hussain SR. 2017. Patellar tendon in vivo regional strain with varying knee angle. J. Biomech. 61:45–50.

113. Ristaniemi A, Regmi D, Mondal D, et al. 2021. Structure, composition and fibril-reinforced poroviscoelastic properties of bovine knee ligaments and patellar tendon. J. R. Soc. Interface 18(174):20200737.

114. Donczo B, Guttman A. 2018. Biomedical analysis of formalin-fixed, paraffin-embedded tissue samples: The Holy Grail for molecular diagnostics. J. Pharm. Biomed. Anal. 155:125–134.

115. Oheim M, Michael DJ, Geisbauer M, et al. 2006. Principles of two-photon excitation fluorescence microscopy and other nonlinear imaging approaches. Adv. Drug Deliv. Rev. 58(7):788–808.

116. Zavala-García LE, Carriles R, López MG, Sánchez-Segura L. 2022. Microscopic Techniques for the Non-Expert, 2: Principles of Light and Fluorescence Microscopy. In: Kamaraj S-K, Thirumurugan A, Dhanabalan SS, Hevia SA, editors. . Springer. p 25–52.

117. Rachid R. 2022. Principles of Light Microscopy: From Basic to Advanced, 3: Epifluorescence Microscopy. In: Nechyporuk-Zloy V, editor. . p 57–76.

118. White NS, Errington RJ. 2005. Fluorescence techniques for drug delivery research: theory and practice. Adv. Drug Deliv. Rev. 57(1):17–42.

119. Li Y, Yu SM. 2013. Targeting and mimicking collagens via triple helical peptide assembly. Curr. Opin. Chem. Biol. 17(6):968–975.

120. Li Y, Foss CA, Summerfield DD, et al. 2012. Targeting collagen strands by photo-triggered triple-helix hybridization. Proc. Natl. Acad. Sci. 109(37):14767–14772.

121. Li Y, Ho D, Meng H, et al. 2013. Direct Detection of Collagenous Proteins by Fluorescently Labeled Collagen Mimetic Peptides. Bioconjugate Chem 24(1):9–16.

122. Bennink LL, Smith DJ, Foss CA, et al. 2017. High Serum Stability of Collagen Hybridizing Peptides and Their Fluorophore Conjugates. Mol. Pharm. 14(6):1906–1915.

123. Henriksen K, Karsdal MA. 2019. Biochemistry of Collagens, Laminins and Elastin.:1–12.

124. Lin AH, Zitnay JL, Li Y, et al. 2019. Microplate assay for denatured collagen using collagen hybridizing peptides. J. Orthop. Res. 37(2):431–438.

125. Bank RA, Krikken M, Beekman B, et al. 1997. A simplified measurement of degraded collagen in tissues: Application in healthy, fibrillated and osteoarthritic cartilage. Matrix Biol. 16(5):233–243.

126. Lin AH, Slater CA, Martinez C-J, et al. 2023. Collagen fibrils from both positional and energy-storing tendons exhibit increased amounts of denatured collagen when stretched beyond the yield point. Acta Biomater 155:461–470.

127. Iqbal SMA, Deska-Gauthier D, Kreplak L. 2019. Assessing collagen fibrils molecular damage after a single stretch–release cycle. Soft Matter 15(30):6237–6246.

128. Zitnay JL, Li Y, Qin Z, et al. 2017. Molecular level detection and localization of mechanical damage in collagen enabled by collagen hybridizing peptides. Nat Commun 8(1):14913.

129. Turčanová M, Hrtoň M, Dvořák P, et al. 2021. Full-Range Optical Imaging of Planar Collagen Fiber Orientation Using Polarized Light Microscopy. BioMed Res. Int. 2021:6879765.

130. Wu X, Pankow M, Huang H-YS, Peters K. 2017. High-speed polarized light microscopy for in situ, dynamic measurement of birefringence properties. Meas. Sci. Technol. 29(1):015203.

131. Cristoforetti A, Masè M, Ravelli F. 2023. Model-Based Approach for the Semi-Automatic Analysis of Collagen Birefringence in Polarized Light Microscopy. Appl. Sci. 13(5):2916.

132. Yang B, Jan N, Brazile B, et al. 2018. Polarized light microscopy for 3-dimensional mapping of collagen fiber architecture in ocular tissues. J. Biophotonics 11(8):e201700356.

133. Bancelin S, Nazac A, Ibrahim BH, et al. 2014. Determination of collagen fiber orientation in histological slides using Mueller microscopy and validation by second harmonic generation imaging. Opt. Express 22(19):22561.

134. Yang B, Lesicko J, Sharma M, et al. 2015. Polarized light spatial frequency domain imaging for non-destructive quantification of soft tissue fibrous structures. Biomed. Opt. Express 6(4):1520–1533.

135. Croft WJ. 2006. Under the Microscope Chapter V: The Polarizing Microscope. In: Weiss RJ, editor. . World Scientific Publishing Co. Pte. Ltd. p 31–40.

136. Syrbu NN, Tiron AV, Parvan VI, et al. 2015. Interference of birefractive waves in CdGa2S4 crystals. Phys. B: Condens. Matter 463:88–92.

137. McCall MW, Hodgkinson IJ, Wu Q. 2014. Birefringent Thin Films and Polarizing Elements Part 3: Applications of Birefringent Media. In: , Second. Imperial College Press. p 195–215.

138. Vidal B de C. 2003. Image analysis of tendon helical superstructure using interference and polarized light microscopy. Micron 34(8):423–432.

139. Rowe AJ, Finlay HM, Canham PB. 2003. Collagen Biomechanics in Cerebral Arteries and Bifurcations Assessed by Polarizing Microscopy. J. Vasc. Res. 40(4):406–415.

140. JUNQUEIRA LCU, COSSERMELLI W, BRENTANI R. 1978. Differential Staining of Collagens Type I, II and III by Sirius Red and Polarization Microscopy. Arch. Histol. Jpn. 41(3):267–274.

141. Franchi M, Fini M, Quaranta M, et al. 2007. Crimp morphology in relaxed and stretched rat Achilles tendon. J. Anat. 210(1):1–7.

142. Franchi M, Raspanti M, Dell'Orbo C, et al. 2008. Different Crimp Patterns in Collagen Fibrils Relate to the Subfibrillar Arrangement. Connect. Tissue Res. 49(2):85–91.

143. Spiesz EM, Thorpe CT, Thurner PJ, Screen HRC. 2018. Structure and collagen crimp patterns of functionally distinct equine tendons, revealed by quantitative polarised light microscopy (qPLM). Acta Biomater 70:281–292.

144. Ker RF, Wang XT, Pike AVL. 2000. Fatigue Quality of Mammalian Tendons. J. Exp. Biol. 203(8):1317–1327.

145. Campagnola PJ, Dong C -Y. 2011. Second harmonic generation microscopy: principles and applications to disease diagnosis. Laser Photonics Rev. 5(1):13–26.

146. Ling Y, Li C, Feng K, et al. 2017. Second harmonic generation (SHG) imaging of cancer heterogeneity in ultrasound guided biopsies of prostate in men suspected with prostate cancer. J. Biophotonics 10(6–7):911–918.

147. Tokarz D, Cisek R, Golaraei A, et al. 2015. Ultrastructural features of collagen in thyroid carcinoma tissue observed by polarization second harmonic generation microscopy. Biomed. Opt. Express 6(9):3475–3481.

148. Aghigh A, Bancelin S, Rivard M, et al. 2023. Second harmonic generation microscopy: a powerful tool for bio-imaging. Biophysical Rev :1–28.

149. Kleinman L. 1962. Deformation Potentials in Silicon. I. Uniaxial Strain. Phys. Rev. 128(6):2614–2621.

150. Roth S, Freund I. 1982. Second harmonic generation and orientational order in connective tissue: a mosaic model for fibril orientational ordering in rat-tail tendon. J. Appl. Crystallogr. 15(1):72–78.

151. Freund I, Deutsch M, Sprecher A. 1986. Connective tissue polarity. Optical second-harmonic microscopy, crossed-beam summation, and small-angle scattering in rat-tail tendon. Biophys. J. 50(4):693–712.

152. Roth S, Freund I. 1980. Coherent optical harmonic generation in rat-tail tendon. Opt. Commun. 33(3):292–296.

153. Gusachenko I, Tran V, Houssen YG, et al. 2012. Polarization-Resolved Second-Harmonic Generation in Tendon upon Mechanical Stretching. Biophys. J. 102(9):2220–2229.

154. Yeh M, Su Y, Tzeng M, et al. 2013. Amphiphilic Design of a Discotic Liquid-Crystalline Molecule for Dipole Manipulation: Hierarchical Columnar Assemblies with a 2D Superlattice Structure. Angew. Chem. 125(3):1065–1068.

155. Tokarz D, Cisek R, Joseph A, et al. 2019. Characterization of pathological thyroid tissue using polarization-sensitive second harmonic generation microscopy. Lab. Investig. 100(10):1280–1287.

156. Roth S, Freund I. 1981. Optical second-harmonic scattering in rat-tail tendon. Biopolymers 20(6):1271–1290.

157. Golaraei A, Mirsanaye K, Ro Y, et al. 2019. Collagen chirality and three-dimensional orientation studied with polarimetric second-harmonic generation microscopy. J. Biophotonics 12(1):e201800241.

158. Freund I, Deutsch M. 1986. Macroscopic polarity of connective tissue is due to discrete polar structures. Biopolymers 25(4):601–606.

159. Brittain K, Harvey M, Cisek R, et al. 2022. Second harmonic generation microscopy of otoconia. Biomed. Opt. Express 13(6):3593.

160. Harvey M, Cisek R, Alizadeh M, et al. 2022. Microscopic structural study of collagen aging in isolated fibrils using polarized second harmonic generation. J Biomed Opt 17(8):080506-1-080506–3.

161. Harvey M, Cisek R, Alizadeh M, et al. 2023. High numerical aperture imaging allows chirality measurement in individual collagen fibrils using polarization second harmonic generation microscopy. Nanophotonics-berlin 12(11):2061–2071.

162. Roth S, Freund I. 1980. Erratum: Second harmonic generation in collagen [J. Chem. Phys. 7 , 1637 (1979)]. J. Chem. Phys. 73(7):3521–3521.

163. Roth S, Freund I. 1979. Second harmonic generation in collagen. J. Chem. Phys. 70(4):1637–1643.

164. Schmidt EC, Chin M, Aoyama JT, et al. 2019. Mechanical and Microstructural Properties of Pediatric Anterior Cruciate Ligaments and Autograft Tendons Used for Reconstruction. Orthop. J. Sports Med. 7(1):2325967118821667.

165. Yeung CC, Svensson RB, Yurchenko K, et al. 2023. Disruption of day-to-night changes in circadian gene expression with chronic tendinopathy. J. Physiol. .

166. Dudek M, Meng Q-J. 2014. Running on time: the role of circadian clocks in the musculoskeletal system. Biochem. J. 463(Pt 1):1–8.

167. Goh KL, Chen Y, Chou SM, et al. 2010. Effects of frozen storage temperature on the elasticity of tendons from a small murine model. Animal 4(9):1613–1617.

168. Oswald I, Rickert M, Brüggemann G-P, et al. 2017. The influence of cryopreservation and quick-freezing on the mechanical properties of tendons. J Biomech 64:226–230.

169. Ng BH, Chou SM, Lim BH, Chong A. 2005. The Changes in the Tensile Properties of Tendons after Freeze Storage in Saline Solution. Proc Institution Mech Eng Part H J Eng Medicine 219(6):387–392.

170. Quirk NP, Padilla CLD, Vega REDL, et al. 2018. Effects of freeze-thaw on the biomechanical and structural properties of the rat Achilles tendon. J Biomech 81:52–57.

171. Huang H, Zhang J, Sun K, et al. 2011. Effects of repetitive multiple freeze–thaw cycles on the biomechanical properties of human flexor digitorum superficialis and flexor pollicis longus tendons. Clin Biomech 26(4):419–423.

172. Chen L, Wu Y, Yu J, et al. 2011. Effect of repeated freezing–thawing on the Achilles tendon of rabbits. Knee Surg Sports Traumatology Arthrosc 19(6):1028–1034.

Appendix I – CAD Drawings

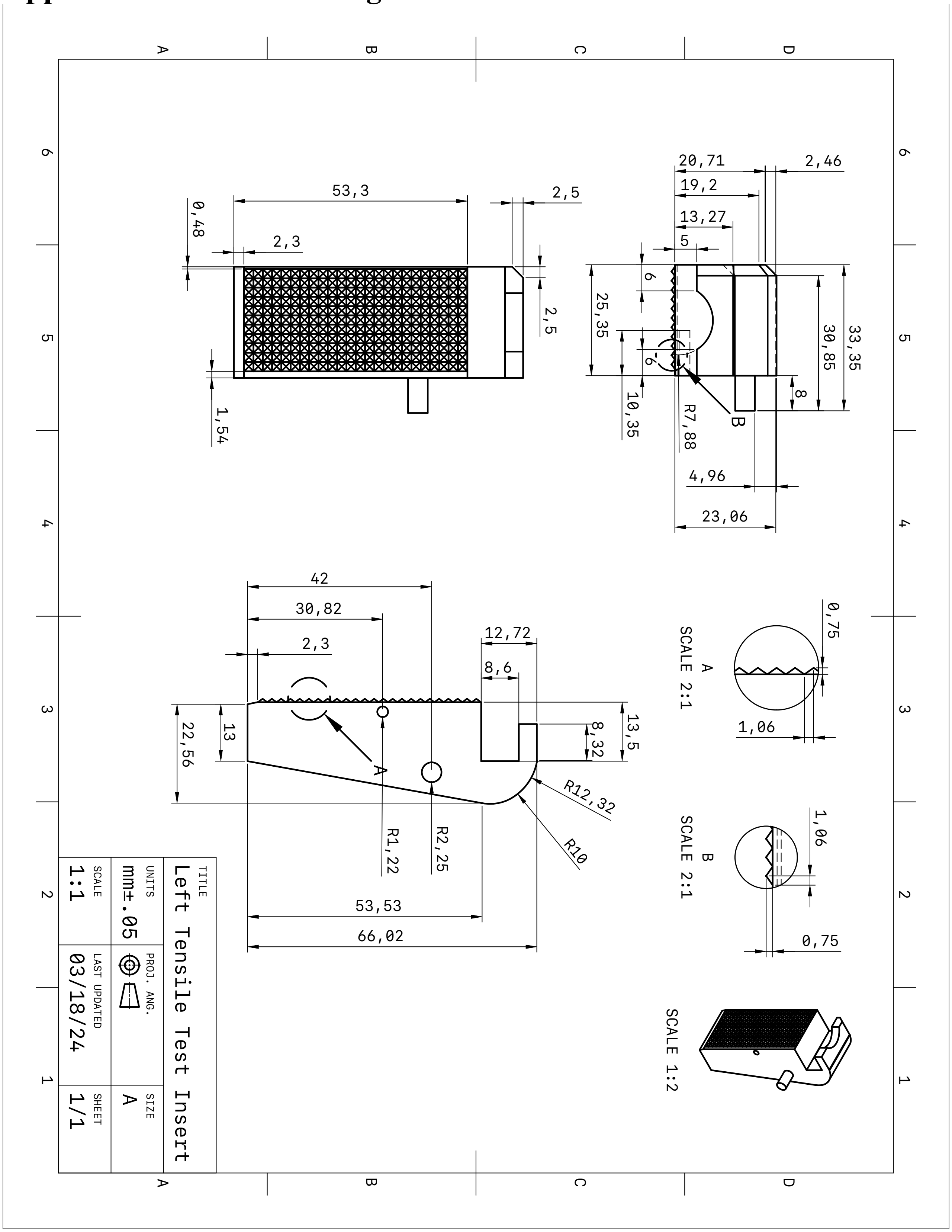

Figure A I.1: Engineering drawing of the left insert used for tensile testing. The drawing is intended for 3-D printing using plastics. The hole of radius 1.22 mm was left for a piece of metal to be inserted. In the tensile testing apparatus, one end of the spring is placed around the piece of metal as the spring tightens the clamps as it is loaded. The hole was placed as the plastic used for the insert was not strong enough to support the spring force, so a stronger material was required.

Appendix II – Licenses for Copyrighted Materials

CCC Marketplace

This is a License Agreement between Austin Yazbek MacDonald/Saint Mary's University ("User") and Copyright Clearance Center, Inc. ("CCC") on behalf of the Rightsholder identified in the order details below. The license consists of the order details, the Marketplace Permissions General Terms and Conditions below, and any Rightsholder Terms and Conditions which are included below.

All payments must be made in full to CCC in accordance with the Marketplace Permissions General Terms and Conditions below.

Order Date	14-Mar-2024	**Type of Use**	Republish in a thesis/dissertation
Order License ID	1461430-1	**Publisher**	BLACKWELL PUBLISHING
ISSN	1475-1305	**Portion**	Chart/graph/table/figure

LICENSED CONTENT

Publication Title	Strain	**Publication Type**	e-Journal
Article Title	Local Strain Measurement within Tendon	**Start Page**	157
		End Page	163
Author/Editor	British Society for Strain Measurement.	**Issue**	4
		Volume	40
Date	01/01/1965	**URL**	http://www.blackwellpublishing.com/journal.asp?ref=0039-2103
Language	English		
Country	United Kingdom of Great Britain and Northern Ireland		
Rightsholder	John Wiley & Sons - Books		

REQUEST DETAILS

Portion Type	Chart/graph/table/figure	**Distribution**	Canada
Number of Charts / Graphs / Tables / Figures Requested	1	**Translation**	Original language of publication
		Copies for the Disabled?	No
Format (select all that apply)	Print, Electronic	**Minor Editing Privileges?**	No
Who Will Republish the Content?	Academic institution	**Incidental Promotional Use?**	No
Duration of Use	Life of current and all future editions	**Currency**	CAD
Lifetime Unit Quantity	Up to 499		
Rights Requested	Main product		

NEW WORK DETAILS

Title	The Effect of Cyclic Buckling on the Structure and Mechanical Properties of Ovine Tendon	**Institution Name**	Saint Mary's University
		Expected Presentation Date	2024-04-10

Instructor Name	Austin Yazbek MacDonald

ADDITIONAL DETAILS

The Requesting Person / Organization to Appear on the License	Austin Yazbek MacDonald/Saint Mary's University

REQUESTED CONTENT DETAILS

Title, Description or Numeric Reference of the Portion(s)	Figure 1	**Title of the Article / Chapter the Portion Is From**	Local Strain Measurement within Tendon
Editor of Portion(s)	Screen, H. R. C.; Bader, D. L.; Lee, D. A.; Shelton, J. C.	**Author of Portion(s)**	Screen, H. R. C.; Bader, D. L.; Lee, D. A.; Shelton, J. C.
Volume / Edition	40	**Publication Date of Portion**	2004-11-12
Page or Page Range of Portion	157-163		

RIGHTSHOLDER TERMS AND CONDITIONS

No right, license or interest to any trademark, trade name, service mark or other branding ("Marks") of WILEY or its licensors is granted hereunder, and you agree that you shall not assert any such right, license or interest with respect thereto. You may not alter, remove or suppress in any manner any copyright, trademark or other notices displayed by the Wiley material. This Agreement will be void if the Type of Use, Format, Circulation, or Requestor Type was misrepresented during the licensing process. In no instance may the total amount of Wiley Materials used in any Main Product, Compilation or Collective work comprise more than 5% (if figures/tables) or 15% (if full articles/chapters) of the (entirety of the) Main Product, Compilation or Collective Work. Some titles may be available under an Open Access license. It is the Licensors' responsibility to identify the type of Open Access license on which the requested material was published, and comply fully with the terms of that license for the type of use specified Further details can be found on Wiley Online Library http://olabout.wiley.com/WileyCDA/Section/id-410895.html.

Marketplace Permissions General Terms and Conditions

The following terms and conditions ("General Terms"), together with any applicable Publisher Terms and Conditions, govern User's use of Works pursuant to the Licenses granted by Copyright Clearance Center, Inc. ("CCC") on behalf of the applicable Rightsholders of such Works through CCC's applicable Marketplace transactional licensing services (each, a "Service").

1) **Definitions.** For purposes of these General Terms, the following definitions apply:

"License" is the licensed use the User obtains via the Marketplace platform in a particular licensing transaction, as set forth in the Order Confirmation.

"Order Confirmation" is the confirmation CCC provides to the User at the conclusion of each Marketplace transaction. "Order Confirmation Terms" are additional terms set forth on specific Order Confirmations not set forth in the General Terms that can include terms applicable to a particular CCC transactional licensing service and/or any Rightsholder-specific terms.

"Rightsholder(s)" are the holders of copyright rights in the Works for which a User obtains licenses via the Marketplace platform, which are displayed on specific Order Confirmations.

"Terms" means the terms and conditions set forth in these General Terms and any additional Order Confirmation Terms collectively.

"User" or "you" is the person or entity making the use granted under the relevant License. Where the person accepting the Terms on behalf of a User is a freelancer or other third party who the User authorized to accept the General Terms on the

User's behalf, such person shall be deemed jointly a User for purposes of such Terms.

"Work(s)" are the copyright protected works described in relevant Order Confirmations.

2) **Description of Service.** CCC's Marketplace enables Users to obtain Licenses to use one or more Works in accordance with all relevant Terms. CCC grants Licenses as an agent on behalf of the copyright rightsholder identified in the relevant Order Confirmation.

3) **Applicability of Terms.** The Terms govern User's use of Works in connection with the relevant License. In the event of any conflict between General Terms and Order Confirmation Terms, the latter shall govern. User acknowledges that Rightsholders have complete discretion whether to grant any permission, and whether to place any limitations on any grant, and that CCC has no right to supersede or to modify any such discretionary act by a Rightsholder.

4) **Representations; Acceptance.** By using the Service, User represents and warrants that User has been duly authorized by the User to accept, and hereby does accept, all Terms.

5) **Scope of License; Limitations and Obligations.** All Works and all rights therein, including copyright rights, remain the sole and exclusive property of the Rightsholder. The License provides only those rights expressly set forth in the terms and conveys no other rights in any Works

6) **General Payment Terms.** User may pay at time of checkout by credit card or choose to be invoiced. If the User chooses to be invoiced, the User shall: (i) remit payments in the manner identified on specific invoices, (ii) unless otherwise specifically stated in an Order Confirmation or separate written agreement, Users shall remit payments upon receipt of the relevant invoice from CCC, either by delivery or notification of availability of the invoice via the Marketplace platform, and (iii) if the User does not pay the invoice within 30 days of receipt, the User may incur a service charge of 1.5% per month or the maximum rate allowed by applicable law, whichever is less. While User may exercise the rights in the License immediately upon receiving the Order Confirmation, the License is automatically revoked and is null and void, as if it had never been issued, if CCC does not receive complete payment on a timely basis.

7) **General Limits on Use.** Unless otherwise provided in the Order Confirmation, any grant of rights to User (i) involves only the rights set forth in the Terms and does not include subsequent or additional uses, (ii) is non-exclusive and non-transferable, and (iii) is subject to any and all limitations and restrictions (such as, but not limited to, limitations on duration of use or circulation) included in the Terms. Upon completion of the licensed use as set forth in the Order Confirmation, User shall either secure a new permission for further use of the Work(s) or immediately cease any new use of the Work(s) and shall render inaccessible (such as by deleting or by removing or severing links or other locators) any further copies of the Work. User may only make alterations to the Work if and as expressly set forth in the Order Confirmation. No Work may be used in any way that is unlawful, including without limitation if such use would violate applicable sanctions laws or regulations, would be defamatory, violate the rights of third parties (including such third parties' rights of copyright, privacy, publicity, or other tangible or intangible property), or is otherwise illegal, sexually explicit, or obscene. In addition, User may not conjoin a Work with any other material that may result in damage to the reputation of the Rightsholder. Any unlawful use will render any licenses hereunder null and void. User agrees to inform CCC if it becomes aware of any infringement of any rights in a Work and to cooperate with any reasonable request of CCC or the Rightsholder in connection therewith.

8) **Third Party Materials.** In the event that the material for which a License is sought includes third party materials (such as photographs, illustrations, graphs, inserts and similar materials) that are identified in such material as having been used by permission (or a similar indicator), User is responsible for identifying, and seeking separate licenses (under this Service, if available, or otherwise) for any of such third party materials; without a separate license, User may not use such third party materials via the License.

9) **Copyright Notice.** Use of proper copyright notice for a Work is required as a condition of any License granted under the Service. Unless otherwise provided in the Order Confirmation, a proper copyright notice will read substantially as follows: "Used with permission of [Rightsholder's name], from [Work's title, author, volume, edition number and year of copyright]; permission conveyed through Copyright Clearance Center, Inc." Such notice must be provided in a reasonably legible font size and must be placed either on a cover page or in another location that any person, upon gaining access to the material which is the subject of a permission, shall see, or in the case of republication Licenses, immediately adjacent to the Work as used (for example, as part of a by-line or footnote) or in the place where substantially all other credits or notices for the new work containing the republished Work are located. Failure to include the required notice results in loss to the Rightsholder and CCC, and the User shall be liable to pay liquidated damages for each such failure equal to

twice the use fee specified in the Order Confirmation, in addition to the use fee itself and any other fees and charges specified.

10) **Indemnity.** User hereby indemnifies and agrees to defend the Rightsholder and CCC, and their respective employees and directors, against all claims, liability, damages, costs, and expenses, including legal fees and expenses, arising out of any use of a Work beyond the scope of the rights granted herein and in the Order Confirmation, or any use of a Work which has been altered in any unauthorized way by User, including claims of defamation or infringement of rights of copyright, publicity, privacy, or other tangible or intangible property.

11) **Limitation of Liability.** UNDER NO CIRCUMSTANCES WILL CCC OR THE RIGHTSHOLDER BE LIABLE FOR ANY DIRECT, INDIRECT, CONSEQUENTIAL, OR INCIDENTAL DAMAGES (INCLUDING WITHOUT LIMITATION DAMAGES FOR LOSS OF BUSINESS PROFITS OR INFORMATION, OR FOR BUSINESS INTERRUPTION) ARISING OUT OF THE USE OR INABILITY TO USE A WORK, EVEN IF ONE OR BOTH OF THEM HAS BEEN ADVISED OF THE POSSIBILITY OF SUCH DAMAGES. In any event, the total liability of the Rightsholder and CCC (including their respective employees and directors) shall not exceed the total amount actually paid by User for the relevant License. User assumes full liability for the actions and omissions of its principals, employees, agents, affiliates, successors, and assigns.

12) **Limited Warranties.** THE WORK(S) AND RIGHT(S) ARE PROVIDED “AS IS.” CCC HAS THE RIGHT TO GRANT TO USER THE RIGHTS GRANTED IN THE ORDER CONFIRMATION DOCUMENT. CCC AND THE RIGHTSHOLDER DISCLAIM ALL OTHER WARRANTIES RELATING TO THE WORK(S) AND RIGHT(S), EITHER EXPRESS OR IMPLIED, INCLUDING WITHOUT LIMITATION IMPLIED WARRANTIES OF MERCHANTABILITY OR FITNESS FOR A PARTICULAR PURPOSE. ADDITIONAL RIGHTS MAY BE REQUIRED TO USE ILLUSTRATIONS, GRAPHS, PHOTOGRAPHS, ABSTRACTS, INSERTS, OR OTHER PORTIONS OF THE WORK (AS OPPOSED TO THE ENTIRE WORK) IN A MANNER CONTEMPLATED BY USER; USER UNDERSTANDS AND AGREES THAT NEITHER CCC NOR THE RIGHTSHOLDER MAY HAVE SUCH ADDITIONAL RIGHTS TO GRANT.

13) **Effect of Breach.** Any failure by User to pay any amount when due, or any use by User of a Work beyond the scope of the License set forth in the Order Confirmation and/or the Terms, shall be a material breach of such License. Any breach not cured within 10 days of written notice thereof shall result in immediate termination of such License without further notice. Any unauthorized (but licensable) use of a Work that is terminated immediately upon notice thereof may be liquidated by payment of the Rightsholder’s ordinary license price therefor; any unauthorized (and unlicensable) use that is not terminated immediately for any reason (including, for example, because materials containing the Work cannot reasonably be recalled) will be subject to all remedies available at law or in equity, but in no event to a payment of less than three times the Rightsholder’s ordinary license price for the most closely analogous licensable use plus Rightsholder’s and/or CCC’s costs and expenses incurred in collecting such payment.

14) **Additional Terms for Specific Products and Services.** If a User is making one of the uses described in this Section 14, the additional terms and conditions apply:

a) ***Print Uses of Academic Course Content and Materials (photocopies for academic coursepacks or classroom handouts).*** For photocopies for academic coursepacks or classroom handouts the following additional terms apply:

i) The copies and anthologies created under this License may be made and assembled by faculty members individually or at their request by on-campus bookstores or copy centers, or by off-campus copy shops and other similar entities.

ii) No License granted shall in any way: (i) include any right by User to create a substantively non-identical copy of the Work or to edit or in any other way modify the Work (except by means of deleting material immediately preceding or following the entire portion of the Work copied) (ii) permit “publishing ventures” where any particular anthology would be systematically marketed at multiple institutions.

iii) Subject to any Publisher Terms (and notwithstanding any apparent contradiction in the Order Confirmation arising from data provided by User), any use authorized under the academic pay-per-use service is limited as follows:

A) any License granted shall apply to only one class (bearing a unique identifier as assigned by the institution, and thereby including all sections or other subparts of the class) at one institution;

B) use is limited to not more than 25% of the text of a book or of the items in a published collection of essays, poems or articles;

C) use is limited to no more than the greater of (a) 25% of the text of an issue of a journal or other periodical or (b) two articles from such an issue;

D) no User may sell or distribute any particular anthology, whether photocopied or electronic, at more than one institution of learning;

E) in the case of a photocopy permission, no materials may be entered into electronic memory by User except in order to produce an identical copy of a Work before or during the academic term (or analogous period) as to which any particular permission is granted. In the event that User shall choose to retain materials that are the subject of a photocopy permission in electronic memory for purposes of producing identical copies more than one day after such retention (but still within the scope of any permission granted), User must notify CCC of such fact in the applicable permission request and such retention shall constitute one copy actually sold for purposes of calculating permission fees due; and

F) any permission granted shall expire at the end of the class. No permission granted shall in any way include any right by User to create a substantively non-identical copy of the Work or to edit or in any other way modify the Work (except by means of deleting material immediately preceding or following the entire portion of the Work copied).

iv) Books and Records; Right to Audit. As to each permission granted under the academic pay-per-use Service, User shall maintain for at least four full calendar years books and records sufficient for CCC to determine the numbers of copies made by User under such permission. CCC and any representatives it may designate shall have the right to audit such books and records at any time during User's ordinary business hours, upon two days' prior notice. If any such audit shall determine that User shall have underpaid for, or underreported, any photocopies sold or by three percent (3%) or more, then User shall bear all the costs of any such audit; otherwise, CCC shall bear the costs of any such audit. Any amount determined by such audit to have been underpaid by User shall immediately be paid to CCC by User, together with interest thereon at the rate of 10% per annum from the date such amount was originally due. The provisions of this paragraph shall survive the termination of this License for any reason.

b) ***Digital Pay-Per-Uses of Academic Course Content and Materials (e-coursepacks, electronic reserves, learning management systems, academic institution intranets).*** For uses in e-coursepacks, posts in electronic reserves, posts in learning management systems, or posts on academic institution intranets, the following additional terms apply:

i) The pay-per-uses subject to this Section 14(b) include:

A) **Posting e-reserves, course management systems, e-coursepacks for text-based content,** which grants authorizations to import requested material in electronic format, and allows electronic access to this material to members of a designated college or university class, under the direction of an instructor designated by the college or university, accessible only under appropriate electronic controls (e.g., password);

B) **Posting e-reserves, course management systems, e-coursepacks for material consisting of photographs or other still images not embedded in text,** which grants not only the authorizations described in Section 14(b)(i)(A) above, but also the following authorization: to include the requested material in course materials for use consistent with Section 14(b)(i)(A) above, including any necessary resizing, reformatting or modification of the resolution of such requested material (provided that such modification does not alter the underlying editorial content or meaning of the requested material, and provided that the resulting modified content is used solely within the scope of, and in a manner consistent with, the particular authorization described in the Order Confirmation and the Terms), but not including any other form of manipulation, alteration or editing of the requested material;

C) **Posting e-reserves, course management systems, e-coursepacks or other academic distribution for audiovisual content,** which grants not only the authorizations described in Section 14(b)(i)(A) above, but also the following authorizations: (i) to include the requested material in course materials for use consistent with Section 14(b)(i)(A) above; (ii) to display and perform the requested material to such members of such class in the physical classroom or remotely by means of streaming media or other video formats; and (iii) to "clip" or reformat the requested material for purposes of time or content management or ease of delivery, provided that such "clipping" or reformatting does not alter the underlying editorial content or meaning of the requested material and that the resulting material is used solely within the scope of, and in a manner consistent with, the particular authorization described in the Order Confirmation and the Terms. Unless expressly set forth in the relevant Order Conformation, the License does not authorize any other form of manipulation, alteration or editing of the requested material.

ii) Unless expressly set forth in the relevant Order Confirmation, no License granted shall in any way: (i) include any right by User to create a substantively non-identical copy of the Work or to edit or in any other way modify the Work (except by means of deleting material immediately preceding or following the entire portion of the Work copied or, in the case of Works subject to Sections 14(b)(1)(B) or (C) above, as described in such Sections) (ii) permit "publishing ventures" where any particular course materials would be systematically marketed at multiple institutions.

iii) Subject to any further limitations determined in the Rightsholder Terms (and notwithstanding any apparent contradiction in the Order Confirmation arising from data provided by User), any use authorized under the electronic course content pay-per-use service is limited as follows:

A) any License granted shall apply to only one class (bearing a unique identifier as assigned by the institution, and thereby including all sections or other subparts of the class) at one institution;

B) use is limited to not more than 25% of the text of a book or of the items in a published collection of essays, poems or articles;

C) use is limited to not more than the greater of (a) 25% of the text of an issue of a journal or other periodical or (b) two articles from such an issue;

D) no User may sell or distribute any particular materials, whether photocopied or electronic, at more than one institution of learning;

E) electronic access to material which is the subject of an electronic-use permission must be limited by means of electronic password, student identification or other control permitting access solely to students and instructors in the class;

F) User must ensure (through use of an electronic cover page or other appropriate means) that any person, upon gaining electronic access to the material, which is the subject of a permission, shall see:

- a proper copyright notice, identifying the Rightsholder in whose name CCC has granted permission,
- a statement to the effect that such copy was made pursuant to permission,
- a statement identifying the class to which the material applies and notifying the reader that the material has been made available electronically solely for use in the class, and
- a statement to the effect that the material may not be further distributed to any person outside the class, whether by copying or by transmission and whether electronically or in paper form, and User must also ensure that such cover page or other means will print out in the event that the person accessing the material chooses to print out the material or any part thereof.

G) any permission granted shall expire at the end of the class and, absent some other form of authorization, User is thereupon required to delete the applicable material from any electronic storage or to block electronic access to the applicable material.

iv) Uses of separate portions of a Work, even if they are to be included in the same course material or the same university or college class, require separate permissions under the electronic course content pay-per-use Service. Unless otherwise provided in the Order Confirmation, any grant of rights to User is limited to use completed no later than the end of the academic term (or analogous period) as to which any particular permission is granted.

v) Books and Records; Right to Audit. As to each permission granted under the electronic course content Service, User shall maintain for at least four full calendar years books and records sufficient for CCC to determine the numbers of copies made by User under such permission. CCC and any representatives it may designate shall have the right to audit such books and records at any time during User's ordinary business hours, upon two days' prior notice. If any such audit shall determine that User shall have underpaid for, or underreported, any electronic copies used by three percent (3%) or more, then User shall bear all the costs of any such audit; otherwise, CCC shall bear the costs of any such audit. Any amount determined by such audit to have been underpaid by User shall immediately be paid to CCC by User, together with interest thereon at the rate of 10% per annum from the date such amount was originally due. The provisions of this paragraph shall survive the termination of this license for any reason.

c) ***Pay-Per-Use Permissions for Certain Reproductions (Academic photocopies for library reserves and interlibrary loan reporting) (Non-academic internal/external business uses and commercial document delivery).*** The License expressly excludes the uses listed in Section (c)(i)-(v) below (which must be subject to separate license from the applicable Rightsholder) for: academic photocopies for library reserves and interlibrary loan reporting; and non-academic internal/external business uses and commercial document delivery.

i) electronic storage of any reproduction (whether in plain-text, PDF, or any other format) other than on a transitory basis;

ii) the input of Works or reproductions thereof into any computerized database;

iii) reproduction of an entire Work (cover-to-cover copying) except where the Work is a single article;

iv) reproduction for resale to anyone other than a specific customer of User;

v) republication in any different form. Please obtain authorizations for these uses through other CCC services or directly from the rightsholder.

Any license granted is further limited as set forth in any restrictions included in the Order Confirmation and/or in these Terms.

d) ***Electronic Reproductions in Online Environments (Non-Academic-email, intranet, internet and extranet).*** For “electronic reproductions”, which generally includes e-mail use (including instant messaging or other electronic transmission to a defined group of recipients) or posting on an intranet, extranet or Intranet site (including any display or performance incidental thereto), the following additional terms apply:

i) Unless otherwise set forth in the Order Confirmation, the License is limited to use completed within 30 days for any use on the Internet, 60 days for any use on an intranet or extranet and one year for any other use, all as measured from the “republication date” as identified in the Order Confirmation, if any, and otherwise from the date of the Order Confirmation.

ii) User may not make or permit any alterations to the Work, unless expressly set forth in the Order Confirmation (after request by User and approval by Rightsholder); provided, however, that a Work consisting of photographs or other still images not embedded in text may, if necessary, be resized, reformatted or have its resolution modified without additional express permission, and a Work consisting of audiovisual content may, if necessary, be “clipped” or reformatted for purposes of time or content management or ease of delivery (provided that any such resizing, reformatting, resolution modification or “clipping” does not alter the underlying editorial content or meaning of the Work used, and that the resulting material is used solely within the scope of, and in a manner consistent with, the particular License described in the Order Confirmation and the Terms.

15) **Miscellaneous.**

a) User acknowledges that CCC may, from time to time, make changes or additions to the Service or to the Terms, and that Rightsholder may make changes or additions to the Rightsholder Terms. Such updated Terms will replace the prior terms and conditions in the order workflow and shall be effective as to any subsequent Licenses but shall not apply to Licenses already granted and paid for under a prior set of terms.

b) Use of User-related information collected through the Service is governed by CCC’s privacy policy, available online at www.copyright.com/about/privacy-policy/.

c) The License is personal to User. Therefore, User may not assign or transfer to any other person (whether a natural person or an organization of any kind) the License or any rights granted thereunder; provided, however, that, where applicable, User may assign such License in its entirety on written notice to CCC in the event of a transfer of all or substantially all of User’s rights in any new material which includes the Work(s) licensed under this Service.

d) No amendment or waiver of any Terms is binding unless set forth in writing and signed by the appropriate parties, including, where applicable, the Rightsholder. The Rightsholder and CCC hereby object to any terms contained in any writing prepared by or on behalf of the User or its principals, employees, agents or affiliates and purporting to govern or otherwise relate to the License described in the Order Confirmation, which terms are in any way inconsistent with any Terms set forth in the Order Confirmation, and/or in CCC's standard operating procedures, whether such writing is prepared prior to, simultaneously with or subsequent to the Order Confirmation, and whether such writing appears on a copy of the Order Confirmation or in a separate instrument.

e) The License described in the Order Confirmation shall be governed by and construed under the law of the State of New York, USA, without regard to the principles thereof of conflicts of law. Any case, controversy, suit, action, or proceeding arising out of, in connection with, or related to such License shall be brought, at CCC's sole discretion, in any federal or state court located in the County of New York, State of New York, USA, or in any federal or state court whose geographical jurisdiction covers the location of the Rightsholder set forth in the Order Confirmation. The parties expressly submit to the personal jurisdiction and venue of each such federal or state court.

Last updated October 2022

Craig Myles 12:17 PM

RP-11392 I would like to use part of figure 5 from the article listed below, in my Master's thesis

To: austin.yazbek.macdonald@smu.ca

Reply above this line.

Craig Myles commented:

Dear Austin Yazbek MacDonald,

Thank you for your ticket. I am pleased to report we can grant your request to reuse part of Figure 5 from “Mechanical and Microstructural Properties of Pediatric Anterior Cruciate Ligaments and Autograft Tendons Used for Reconstruction” without a fee as part of your thesis.

Please accept this email as permission for your request as detailed above. Permission is granted for the life of the thesis on a non-exclusive basis, in the English language, throughout the world in all formats provided full citation is made to the original Sage publication. Permission does not include any third-party material found within the work. Please contact us for any further usage of the material.

Please note that as this article is under a CC BY-NC-Non-Derivative license that you will need to indicate the figure has been adapted with permission, indicate the changes you have made to the figure, indicate the Creative Commons license, and provide a link to the license: https://creativecommons.org/licenses/by-nc-nd/4.0/

If you have any questions, or if we may be of further assistance, please let us know.

Kind regards,

Craig Myles (*he/him/his*)
Rights Administrator

2455 Teller Road
Thousand Oaks, CA 91320
USA
www.sagepublications.com

View request · Turn off this request's notifications

This is shared with Austin Yazbek MacDonald.